Radiative Capture Measurements of Astrophysically Important Reactions Using the DRAGON Separator

Charles Akers

Doctor of Philosophy

University of York

Physics

October 2014

Abstract

The rate of the ^{18}F(p,γ)^{19}Ne reaction affects the final abundance of the γ-ray observable radioisotope ^{18}F, produced in novae. However the rate used is calculated from incomplete information on the contributing resonances. Of the two resonances thought to play a significant role, one has a radiative width estimated from the assumed analogue state in the mirror nucleus, ^{19}F. The second, located at E_{cm}=665 keV, does not have an analogue state assignment at all, as such it's radiative width is extremely uncertain. This thesis presents the first successful direct measurement of the ^{18}F(p,γ)^{19}Ne reaction, conducted at the recoil separator facility DRAGON. The strength of the 665 keV resonance (E$_x$=7.076 MeV) was found to be an order of magnitude weaker than currently assumed in nova models. Reaction rate calculations show that this resonance therefore plays no significant role in the destruction of ^{18}F at any astrophysical energy.

As part of an ongoing endeavour to expand DRAGON's capabilities to include heavy ion reactions, ^{76}Se(α,γ)^{80}Kr was also measured at astrophysical energies. This reaction is relevant to the production of p-nuclei, which are the 35 proton rich nuclei with A>56 that cannot be created via the s- or r-processes. Although their production mechanism(s) remain ambiguous, one favoured scenario involves a series of (γ,n) photo disintegration reactions from r/s seed nuclei. ^{80}Kr represents a branching point in this process, with the uncertainty in its (γ,α) rate having a large influence on abundance calculations of various astrophysical models. Observation of the ^{76}Se(α,γ)^{80}Kr reaction can be used to better characterize the reverse (γ,α) reaction rate. At DRAGON the cross section of the forward reaction was successfully measured at two astrophysical energies. Results agree well with theoretical predictions and represent the first time a recoil separator has been used for such a study.

Contents

List of Figures

List of Tables

Acknowledgements

I would like to thank all the members of the DRAGON group (Chris Ruiz, Jennifer Fallis, Greg Christian and Dave Hutcheon) for their advice and assistance over the last three years, as well as operating the apparatus during experiments. Special thanks must also go to my supervisor Brian Fulton for all his guidance, as well as Alison Laird for her support. Without such help this thesis would not have been possible.

Thanks also to the people who assisted in the successful running of experiments and compilation of this work: Dario Gigliotti, James DeBoer, Peter Machule, Ulrike Hager, Barry Davids and many more.

Declaration of Authorship

I, Charles Akers, declare that this thesis titled, 'Radiative Capture Measurements of Astrophysically Important Reactions Using the DRAGON Separator' and the work presented in it are my own. I confirm that:

- This work was done wholly or mainly while in candidature for a research degree at this University.
- Where any part of this thesis has previously been submitted for a degree or any other qualification at this University or any other institution, this has been clearly stated.
- Where I have consulted the published work of others, this is always clearly attributed.
- Where I have quoted from the work of others, the source is always given. With the exception of such quotations, this thesis is entirely my own work.
- I have acknowledged all main sources of help.
- Where the thesis is based on work done by myself jointly with others, I have made clear exactly what was done by others and what I have contributed myself.

Charles Akers

"The shortest and surest way of arriving at real knowledge is to unlearn the lessons we have been taught, to mount the first principles, and take nobody's word about them."

Henry IV of England

Chapter 1

Introduction

Stars shine due to the energy released via nuclear fusion in their cores[1], a process that generates heat resulting in the production of the majority of isotopes heavier than helium. During their lifetime, and after dying, some stars release their inner synthesized material providing the means of new stellar systems to form, including our own solar system. As a result the iron in your blood and the oxygen in your lungs were all produced in the interior of ancient stars, via a variety of processes, long ago. Given that the Earth's age is approximately 4 Gy [1] and the galaxy it resides in is approximately 14 Gy old [2], we can estimate that it took around 10 Gy for all of these elements to be synthesized. The isotopic enrichment of our universe is referred to as nucleosynthesis and forms the basis of nuclear astrophysics, the discipline that merges both nuclear physics and astrophysics. It combines experimental and theoretical aspects of science; the theoretical models require experimental data to constrain input parameters. A better understanding of nucleosynthesis can help us explain the composition of both individual stars and the solar system as a whole. It can also help us explain the enormous quantities of energy outpouring from systems such as Novae, Supernovae and X-ray bursters.

This thesis focuses on two experiments, measurements of the ^{18}F(p,γ)^{19}Ne and ^{76}Se(α,γ)^{80}Kr reactions, conducted at the TRIUMF laboratory in Vancouver that were carried out to investigate the rate of specific reactions in the astrophysical regime. The former reaction plays a key role in determining the abundance of ^{18}F in novae (see section 3.1.1). This isotope is thought to be primarily responsible for the gamma-ray emission that can be observed from Nova by instruments on board orbiting satellites. Gamma ray measurements enable us to test astrophysical models of these systems, but these in turn rely on a knowledge of the nuclear reactions rates (see section 1.2). The latter reaction forms one channel in the branching of a reaction path in the γ-process (see section 4.1.1). This is the mechanism proposed to account for the solar abundance of the proton rich nuclides heavier than ^{56}Fe, a process which requires more experimental data to be properly characterized.

This Chapter gives a history and brief overview of the field of nuclear astrophysics, then details how reaction rates in stellar environments can be determined experimentally here on Earth. Chapter 2 then describes the experimental apparatus used for the two studies

[1] with the exception of white dwarfs, that have energy stored from previous burning phases, and dark stars which have a inert, cool coating preventing any heat from escaping and hence don't shine

conducted at TRIUMF and the statistical framework needed to interpret the data. The two separate experiments are then expounded in chapters 3 and 4; chapter 5 then details what was ultimately gained from the studies.

1.1 Nucleosynthesis under Astrophysical Conditions

1.1.1 Nuclear Fusion

The process of two nuclei combining to form a compound nucleus is referred to as nuclear fusion and it forms the bases for nucleosynthesis in stars. In the field of nuclear physics, reactions are frequently represented in the form A(a,b)B, where A is the target nucleus (at rest in the laboratory frame) and a is the projectile[2]. B is the heavy compound nucleus formed and b is the lighter product which, in the case of radiative capture, is a γ ray. Figure 1.1 gives a simple illustration of the situation. Such capture reactions, be they (p,γ) or (α,γ), form a significant portion of all astrophysically relevant nuclear processes and hence are the focus of this thesis.

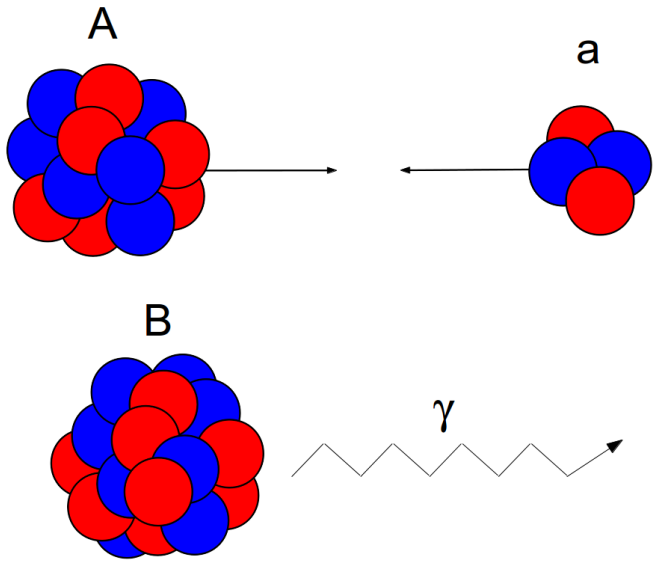

FIGURE 1.1: Illustration of the reaction A(a,γ)B. Such radiative capture reactions are typical in various astrophysical scenarios.

In order for two nuclei to fuse however, they must first overcome the electrostatic repulsion that arises from the positive charge on their constituent protons, termed the *Coulomb barrier* (see figure 1.2). Most stellar scenarios occur at temperatures that correspond to energies below this, and so such reactions occur via the quantum tunnelling effect whereby a particles wavefunction can penetrate a potential barrier greater than its kinetic energy [3]. Once inside the barrier, the target nuclei's potential becomes attractive due to the attractive nature of the short range strong nuclear force, and the compound nuclei may be formed. Fusion reactions

[2] Although reactions in inverse kinematics, where the target is lighter than the beam nucleus, are often presented with the target and projectile symbols reversed. Such is the case for the two experiments expounded in this thesis.

are not always energetically favourable however; when the products have a greater binding energy (see next section) than the reactants a net input of energy is required, and so such processes cannot fuel heat generation in stars.

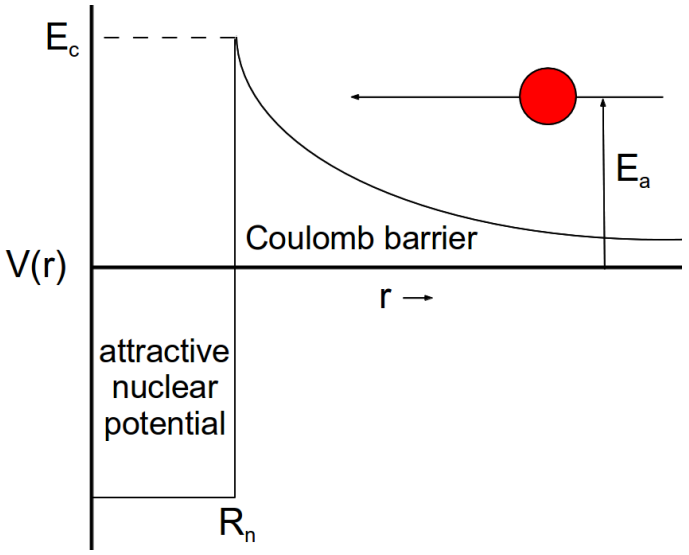

FIGURE 1.2: Graphical representation of the Coulomb barrier (E_c) due to the electrostatic repulsion of nuclei. Although the projectile's kinetic energy (E_a) is less than E_c it may still penetrate inside the target's effective nuclear radius (R_n), due to the quantum tunnelling effect.

1.1.2 Binding Energy

The total mass of a nucleus is not necessarily the same as the sum if it's unbound constituent nucleons. This mass difference can be equated to an energy (using $E = mc^2$) in which case it is referred to as the binding energy, defined quantitatively as [4]:

$$B = \left(Zm_p + Nm_n - m(^A X)\right) c^2 \tag{1.1}$$

Here Z is the nucleus's atomic number, N is it's number of neutrosn and $m(^A X)$ is it's total mass. m_p and m_n are the proton and neutron masses respectively. Figure 1.3 displays the binding energy per nucleon (B/A) as a function of nucleon number (A) for a selection of stable and long lived nuclei. The most prominent features of this graph are that the majority of nuclei have a binding energy per nucleon in the range 7→9 MeV and that a peak forms around A≈60. This suggests that energy can be released when fusing lighter nuclei to heavier ones; such is the case in a variety of stellar scenarios.

Another quantity often used in nuclear physics is the *particle separation energy*. This is the energy required to remove a single proton or neutron from a specific nucleus, defined as [4]:

$$S_p = B(^A_Z X_N) - B(^{A-1}_{Z-1} X_N) \tag{1.2}$$

For protons, and:

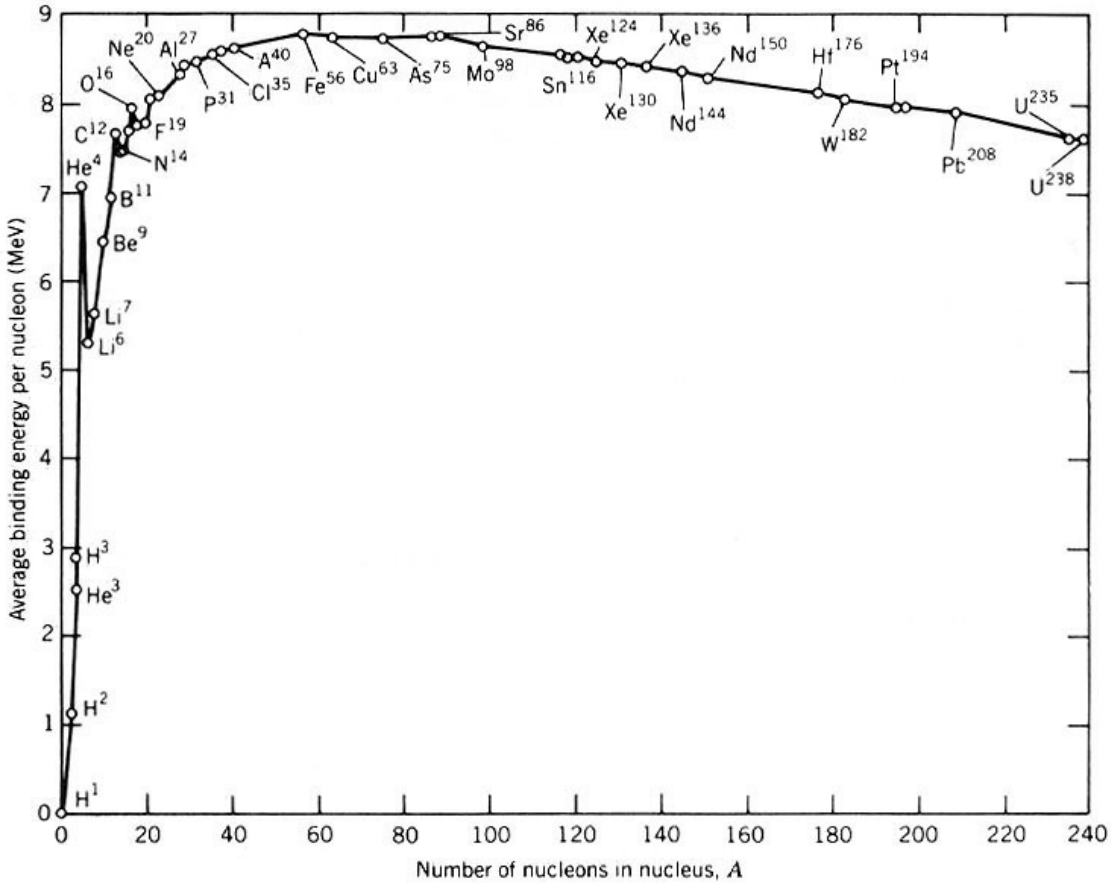

FIGURE 1.3: Binding energy per nucleon for a selection of stable and long lived nuclei. Adapted from [5].

$$S_n = B({}^{A}_{Z}X_N) - B({}^{A-1}_{Z}X_{N-1}) \tag{1.3}$$

For neutrons.

1.1.3 Shell Model

The shell model approximates the structure of the nucleus to be a series of single particle levels divided up into separate *shells*, which in turn consist of various *sub-shells*. This model assumes that the force felt by an individual nucleon can be approximated by a mean potential resulting from the nucleus as a whole [4]. Due to the Pauli exclusion principle, nucleons cannot occupy the same quantum state and so the single particle levels fill up sequentially, with protons and neutrons filling shells separately due to their differing isospin[3]. Filled shells generally correspond to nuclei that are more energetically stable than their neighbours, resulting in large particle separation energies and binding energies per nucleon [6]. The number of nucleons required to fill such a shell are referred to as *magic numbers* (2, 8, 20, 28, 50, 82 and 126).

[3] A quantum number that distinguishes protons from neutrons

1.1.4 History

Francis William Aston was the first person to discover that helium has less than four times the mass of hydrogen [7] as a consequence of its nuclear binding energy, resulting in the release of radiation and neutrinos when four protons combine to form an α particle. Later, Arthur Eddington proposed that this mass difference could be a possible source of heat generation for the sun, via hydrogen fusion, however at this time nobody could account for the fact that observed stellar temperatures were well below that required to overcome the Coulomb barrier between nuclei [6]. The problem was later solved by Gamow, who first explained the phenomenon of quantum tunnelling in alpha decay [3], Atkinson and Houterman [8] then realized that this same process could explain the presence of fusion in stars. Bethe and Critchfield [9] consequently calculated that hydrogen fusion can give a heat output similar to that observed in the sun. The discovery of energy generation in more massive stars, via the CNO cycle (see section 1.1.10) shortly followed, by both Weisacker [10] and Bethe [11].

Later experiments established that no stable isotopes of mass 5 or 8 exist in nature so it remained unknown how heavier elements were produced, until Saltpeter [12] suggested that a triple alpha reaction could bypass these masses via ^{8}Be (see section 1.1.9). Fred Hoyle pointed out however that such a reaction would have too small a cross section unless a state with spin zero and positive parity existed in ^{12}C, at around 7.7 MeV, now referred to as the Hoyle state. Subsequent experiments confirmed both the presence [13] and properties [14] of such a state, paving the way for the framework of heavy element nucleosynthesis [15].

1.1.5 Evidence

The most direct and irrefutable evidence for nucleosynthesis in stars comes primarily from four sources, the first being the discovery of technetium in red giant stars [16]; all of this element's isotopes are radioactive with a half life much shorter than the age of the universe meaning that it must have been produced relatively recently on a cosmological time scale. The second piece of evidence comes from the detection in satellite observations of gamma rays emitted from ^{26}Al [17], as its half life is even shorter than technetium and so the same conclusion can be drawn. Neutrinos, which are fundamental particles formed during various nuclear reactions, provide the third source; they interact with matter very weakly and so are able to bypass the outer layers of stars relatively unhindered, eventually making it to the Earths surface where they can be detected in small numbers. Such measurements have been done, confirming the generation of neutrinos via nuclear reactions in both the sun [18] and type II supernova 1987A [19]. Lastly, gamma-ray emission from the decay of ^{56}Co, again with a half life much shorter than the age of the universe, has been observed directly from SN 1987A [20].

1.1.6 Solar System Abundances

Isotopic abundances in the solar system during its conception is the common benchmark for evaluating stellar models. The two main sources for these abundances are the solar

photosphere and primitive meteorites, containing material that has undergone minimal fractionation, with both showing good agreement (<10%) for most elements. These methods tell us that most of the solar system's primeval mass was, and still is, in the form of hydrogen and helium with all of the former and most of the latter formed during the big bang. Hence these are the elements that form the basis for all nucleosynthesis in stars. Figure 1.4 shows the elemental abundance curve for the solar system, it can be seen that local maxima occur around H and He, C and O and Fe. Such phenomena suggest that far from being synthesized randomly with equal probability, nuclei are instead formed via a series of specific mechanisms; it is the role of nuclear astrophysics to expound such processes.

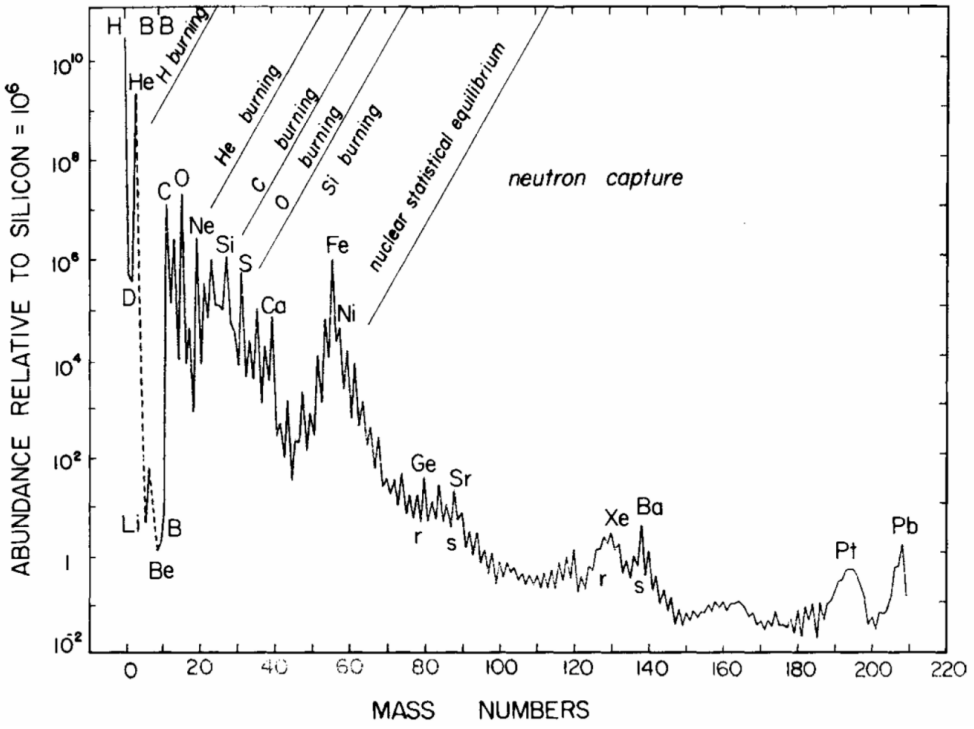

FIGURE 1.4: Elemental solar system abundances, taken from [21].

1.1.7 Star Formation

The first stars formed inside giant cold clouds made from primeval hydrogen and helium, which can contract under the right circumstances, generating heat as gravitation potential is converted to kinetic energy. Although initially most of the energy released is in the form of radiation, once the cloud becomes dense enough its opaqueness reduces heat loss causing the gas temperature to rise. This results in a pressure increase, hence the contraction rate of the central region decreases and as its temperature continues to rise the hydrogen and helium ionize, causing a further reduction in radiation loss due to the extra free electrons which can absorb photons. At this point the collapse of the central part of the cloud halts and a state of hydrostatic equilibrium is reached, although matter is still accreted onto its surface.

When the core temperature reaches a few MK primordial deuterium can fuse with hydrogen and primordial lithium is destroyed, via proton capture, with convection transporting the

energy produced to the surface and causing most of the star's matter to be cycled through its core. In time the temperature rises sufficiently to initiate hydrogen burning, via the pp chain explained below, increasing the energy output from the core. Eventually this source of energy will become the sole resistive force to gravitational collapse and the star will be in both hydrostatic and thermal equilibrium. It can now be referred to as a *main sequence* star, and appears in the appropriate region of the Hertzsprung-Russel diagram (see figure 1.5). The exact position of the star on this diagram depends on its mass, with larger stars being brighter but visibly cooler than their low mass counter parts. Description adapted from [6].

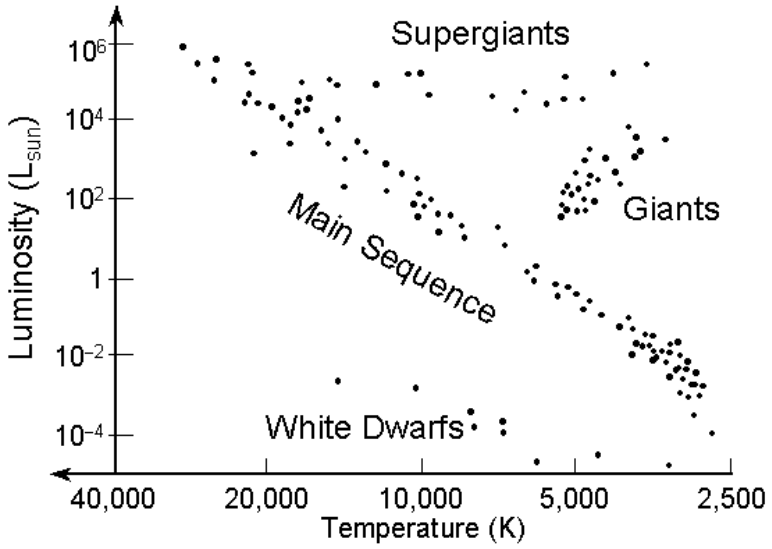

FIGURE 1.5: Hertzsprung Russel diagram showing how surface temperature and luminosity are related for the main stellar phases. Taken from `http://www.astronomy.ohio-state.edu/~pogge/Ast162/Unit1/hrdiag.html`.

1.1.8 pp Chains

The conversion of four protons into a helium nucleus, referred to as hydrogen burning, releases 26.731 MeV and is thus very favourable when considering purely reaction energetics. The specific mechanics of such a process are not as trivial however, as the probability of all four protons colliding simultaneously is far too small to account for main sequence star's heat generation. There are, however, three possible reaction sequences in stars that result in the production of ^{4}He from protons through a sequence of sequential reactions. These sequences are referred to as the pp chains and all three are initiated via the same two reactions: p(p,e$^+\nu$)d and d(p,γ)^{3}He (see figure 1.6). The former relies on the weak nuclear force to convert one of the incident protons into a neutron, which results in the reaction rate being weak (slow) to the point where any direct experimental observation is currently unfeasible. However the theoretical framework for calculating the corresponding S-factor for this reaction is reliable enough that the overall uncertainty in the rate is smaller than many other astrophysical reactions, as it relies on electroweak theory which is well established.

The d(p,γ)^{3}He reaction is the second step in the pp-chain, despite the fact that the competing (d,p) and (d,n) channels have a higher cross section, due to the abundance of protons in the stellar plasma. Experimental data has been obtained at higher energies and extrapolated down to the astrophysical regime [22] however the rate is much more uncertain than the p+p step, at around 30-40%.

pp1 chain The first pp chain is a three step process, the first two already described above, with the final reaction that forms an α particle being: ^{3}He(^{3}He,2p)^{4}He which takes precedence over the (p,γ) channel due to the instability of ^{4}Li. The (^{3}He,2p) mechanism is also favoured over the (d,p) reaction, despite the fact that both have similar cross sections, due to the fact that ^{3}He is produced much more efficiently than it is destroyed. As the relatively large d(p,γ) rate removes synthesized deuterium on a much shorter timescale than the ^{3}He is produced, the ^{3}He(^{3}He,2p)^{4}He has more abundant reactants than ^{3}He(d,p)^{4}He.

pp2 chain At higher temperatures and ^{4}He particle densities the ^{3}He(α,γ)^{7}Be reaction becomes more dominant than the (^{3}He,2p) channel. The ^{7}Be subsequently β-decays to ^{7}Li which is in turn destroyed via ^{7}Li(p,α)α, producing two α particles in the process. This set of reactions, referred to as the pp2 chain, requires one α particle to act as a catalyst.

pp3 chain As the decay of ^{7}Be relies mainly on the weak interaction it has only a small dependence on temperature, the ^{7}Be(p,γ)^{8}B destruction mechanism on the other hand does have such a dependence and becomes more dominant at higher temperatures. ^{8}B β^+ decays to ^{8}Be which in turn breaks up into two α particles; much like the pp2 chain it requires one α to act as a catalyst.

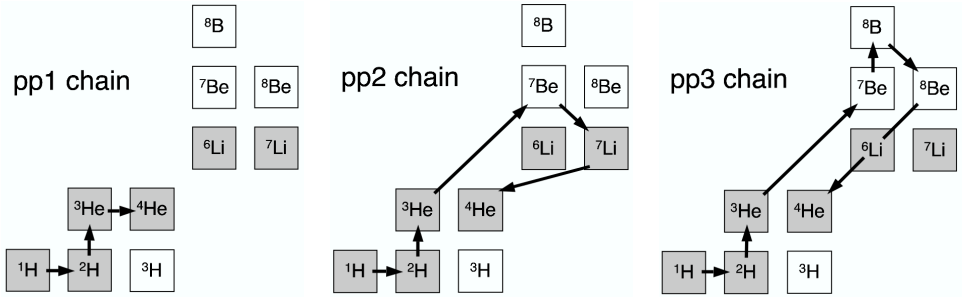

FIGURE 1.6: Illustration of the three pp chain reaction pathways, taken from [6].

All three chains operate simultaneously in H-burning stars, provided there is a sufficiently large α particle density, with chains 1,2 and 3 dominating at $<$ 18 MK, 18$\rightarrow$25 MK and T$>$ 25 MK respectively (see figure 1.7). Direct experimental measurements have been made of d(p,γ)^{3}He, ^{3}He(^{3}He,2p)^{4}He and ^{7}Li(p,α)α reaction rates at the relevant astrophysical energies, however all other reaction rates are too small to be measured with present day experimental techniques and we have to rely on extrapolation and/or theoretical modelling to estimate the rate at solar temperatures.

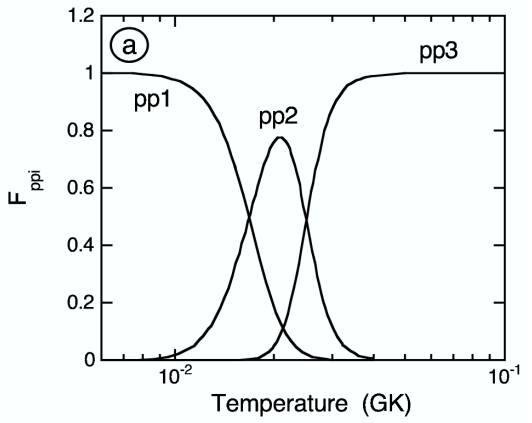

FIGURE 1.7: Graph showing the fraction of α particles produced via each pp chain as a function of temperature, taken from [6].

1.1.9 Helium Burning

Triple α process

The path to synthesizing nuclei heavier than ^{4}He is complicated by the fact that there are no stable nuclides with masses 5 and 8, however ^{12}C is observed to be one of the most abundant nuclides in the universe. Three α particles colliding simultaneously to form ^{12}C is an unfeasible production mechanism for the same reasons given for the four proton scenario in hydrogen burning; the probability of such an event is too small at stellar temperatures. The solution to this problem lies in a two step process, the first being the generation of the unstable nuclei ^{8}Be via an α+α reaction. Despite its short half life, over time enough ^{8}Be forms (at an equilibrium density) for it to undergo radiative capture in the form: ^{8}Be(α,γ)^{12}C.

The second reaction step is made possible at astrophysical energies due to the presence of an s-wave resonance corresponding to a level in ^{12}C near the α particle threshold. Such a state was first predicted by Hoyle [23] and later verified [13, 14], although direct observation remains absent indirect studies have been able to reduce the overall uncertainty in the rate to just 15% [6].

^{12}C(α,γ)^{16}O

In an α rich stellar environment ^{12}C can under go an (α,γ) capture reaction producing ^{16}O. This process is relatively slow however, highlighted by the fact that the observed abundance of ^{16}O is $\approx$0.4 that of ^{12}C, meaning that the latter remains abundant after the helium burning stage. The reaction is very important due to its influence over the given abundance ratio and has been the focus of many studies, however the low reaction rate, due to a lack of resonance(s) in the Gamow peak (see section 1.2.6), makes direct observation beyond what is currently achievable.

1.1.10 CNO Cycles

Most stars contain Carbon, Nitrogen or Oxygen which enables these nuclei to undergo (p,γ) and (p,α) reactions that lead to four cycles of reactions, termed the CNO cycles (see figure 1.8). These cycles act as a substitute for the pp chains in converting four protons into an α particle with the CNO isotopes acting as catalysts. At low stellar temperatures (T<55 MK) the β^+ decays of unstable nuclei in the cycles dominate over the proton capture channel constraining the reaction pathways to the valley of stability and the nuclei immediately around it.

Initially the most abundant catalytic nuclei are ^{12}C and ^{16}O as they are both produced in abundance, relative to nucleons of comparable mass, via the helium burning described above. If we consider just the CNO1 cycle, as illustrated in figure 1.8, with just ^{12}C as seed nuclei at T<0.1 GK, then ^{14}N becomes by far the most abundant nucleus in this region due to its (p,γ) destruction channel being the slowest reaction in the cycle. Hence ^{14}N(p,γ) determines the rate of energy production in the CNO1 cycle, with the reaction being non resonant at low energies leading to a strong temperature dependence; in fact it dominates the pp1 chain rate at T>20 MK. The slow (p,γ) destruction rate also lies behind nitrogen forming part of the prominent peak around carbon and oxygen in the solar abundance curve (figure 1.4).

^{16}O seed nuclei are transformed into ^{17}O, via (p,γ) and the β^+ decay of ^{17}F, with a large fraction destroyed in the (p,α) reaction leading to the CNO1 and 2 cycles. Another possible destruction channel however is the (p,γ) reaction into ^{18}F, leading to the CNO3 and 4 cycles. All four cycles operate simultaneously regardless of seed abundance. Although, as the ^{17}O(p,γ)^{18}F reaction rate is one of the smallest in all four cycles, coupled with the (p,α) rates being stronger than the (p,γ) counterparts on the branching point nuclei (^{15}N,^{17}O, ^{18}O and ^{19}F), the CNO1 cycle dominates energy production at lower temperatures (T<0.1 GK).

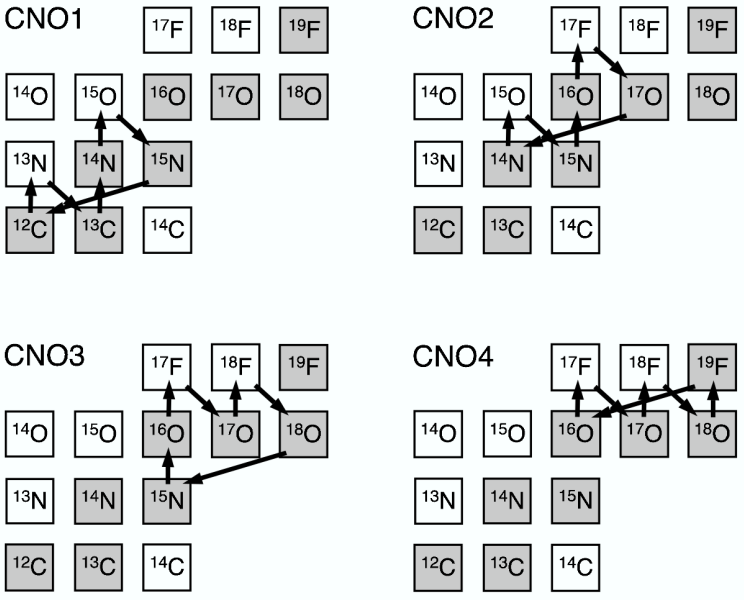

FIGURE 1.8: Outline of all four CNO cycles; the end result is the conversion of four protons into a helium nucleus with CNO seed material acting as a catalyst. Taken from [6].

Hot CNO cycles

At elevated temperatures (T=0.1→0.4 GK) the decay time of certain unstable nuclei participating in the CNO cycles occur on a longer timescale than certain proton capture reactions in this mass region, opening up the possibility of (p,γ) reactions on unstable nuclei. We can see the effects of this scenario by considering the CNO1 cycle described above; the slowest β^+ decay in this cycle comes from ^{13}N and at a certain temperature the competing (p,γ) channel will become the favoured destruction mechanism. As the temperature is increased further eventually even the bottleneck reaction, ^{14}N(p,γ)^{15}O, will proceed faster than the ^{14}O and ^{15}O β^+ decays, leading to the HCNO1 cycle (see figure 1.9). As β^+ decays form the slowest link in the HCNO1 cycle its energy generation rate is independent of temperature, and a large portion of the CNO seed material is synthesized into ^{14}O and ^{15}O.

As the (p,α) channel is far stronger then the (p,γ) for the branching point at ^{15}N, the HCNO1 cycle can be considered an almost closed system. ^{16}O however can also be formed via hydrogen burning, as previously discussed, and can act as a seed nucleus for other hot CNO cycles as outlined in figure 1.9. For T=0.1→0.4 GK the ^{17}O(p,γ) channel allows a small amount of ^{16}O seed material to proceed into the HCNO2 cycle instead of the CNO2 counterpart. Above T=0.23 GK the ^{17}F(p,γ)^{18}Ne can also dominate over the β^+ decay mechanism allowing for the HCNO3 cycle to supplant the CNO3 and 4 paths.

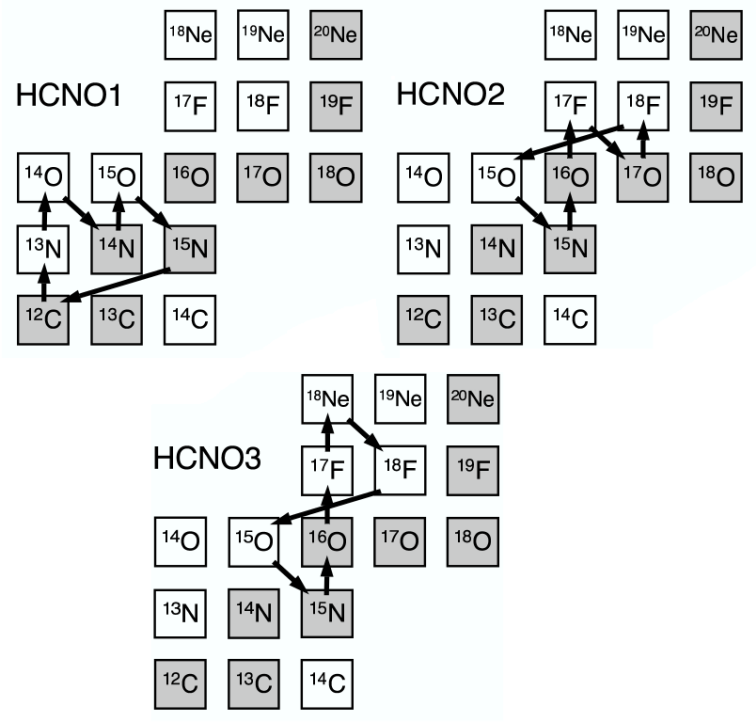

FIGURE 1.9: When stellar temperatures exceed 0.1 GK the three HCNO cycles can dominate energy production given the presence of enough CNO seed material. Taken from [6].

1.1.11 Neutron Capture Processes

As more massive nuclei are synthesized in stars, the prospect for further charged particle capture diminishes due to the greater coulomb repulsion experienced by the reactants. Hence, the prevalence of nuclides with A>60 suggests that another mechanism contributes to their production, as even charge particle capture at the larger temperatures present in explosive scenarios cannot explain their origin. Neutrons however, experience no such repulsion during capture reactions, and so their capture cross sections are quite large, even at lower stellar temperatures. As such, neutron capture reactions provide a reasonable mechanism of production for heavy nuclei, and can explain the abundance of those that have *neutron magic numbers*[4]. As neutrons are unstable, with a decay half life of 614 sec, there is not thought to be a significant concentration of them in the interstellar medium, and so neutron sources are thus required via reactions occurring in stellar environments. The synthesis of heavy elements arising from neutron capture consists of two distinct process: the slow and rapid neutron capture processes, or as they are commonly termed, the *s-* and *r-processes*, described below.

s-process

This scenario is characterized by a series of (n,γ) capture reactions on stable seed nuclei, interspersed with β^- decays. The resulting pathway, illustrated in figure 1.10, never strays far from the chain of stable nuclides that comprise the valley of stability. As such, very neutron rich and deficient nuclei cannot be formed via this process. Another important result of this mechanism is that, as neutron capture cross sections on nuclei with a magic number of neutrons are lower than their neighbour's [6], a waiting point is formed along the process's path. This causes a peak to form in the abundance of such nuclides, accounting for some of the numerous spikes in the abundance plot shown in figure 1.4.

This process is thought to occur in low mass AGB stars, characterized by an inert core of carbon and oxygen, covered by a helium burning shell which is, in turn, enclosed within a hydrogen burning shell. Protons are mixed into the He burning shell, which contains a significant fraction of ^{12}C ($\approx$25% by mass), leading to the production of ^{13}N via proton capture which subsequently β^+ decays into ^{13}C. The reaction ^{13}C(α,n)^{16}O then proceeds, releasing neutrons that are captured by pre-existing seed nuclei, mainly iron, over the course of $\approx$20000 years. This mechanism represents the main component of the s-process, however it is supplemented by the reaction ^{22}Ne(α,n)^{25}Mg, which is activated in the same environment, at higher temperatures (T>0.27 GK).

r-process

In contrast to the slow capture process, the r-process consists of a series of very rapid neutron capture reactions, such that the unstable product nuclei have no time to β decay before the next (n,γ) event. When the neutron source terminates however, β^- decay is allowed to proceed along isobaric chains until a stable nucleus is reached, as illustrated in figure 1.10.

[4] A number of neutrons that corresponds to a filled shell.

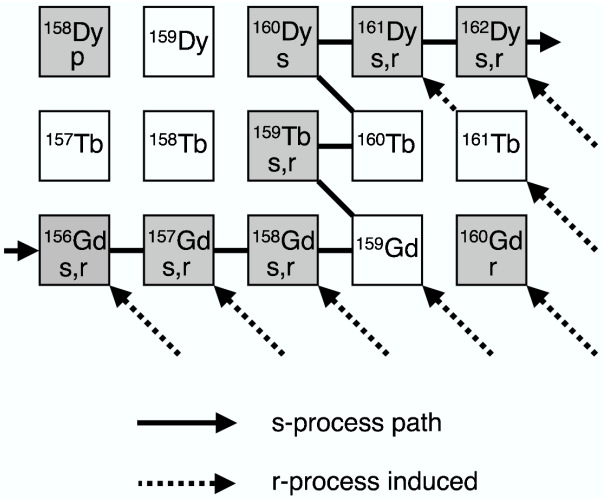

FIGURE 1.10: Illustration of the s- and r-process pathways. Corresponding letters indicate which nuclei can be synthesized via which process (the p-process is explained in section 4.1.1). Taken from [6].

Such a mechanism requires an intense neutron source over a short period of time ($\approx$ seconds) in conjunction with a temperature low enough to prevent photo disintegration. The exact site of the r-process remains ambiguous with several scenarios suggested, including the merger of two neutron stars and core collapse supernovae [6].

1.2 Reaction Cross Sections and Rates in Astrophysical Environments

Ultimately the goal of any experiment of astrophysical importance is to better characterize the reaction's overall rate in a stellar environment. This in done by replicating the reaction, which consists of two bare nuclei colliding with thermal energy, under laboratory conditions. Several complications with this scenario arise however, one of the most prominent being that at astrophysical temperatures nuclei have sub Coulomb barrier energies that severely inhibit the rate of fusion reactions. To compensate for this experiments utilize thick stationary targets, containing many nuclei, and have sophisticated particle ID systems, so that what few reactions occur can be detected with a high efficiency and degree of confidence. Thick targets also have the effect of causing energy loss to the beam meaning that any single measurement using a mono energetic beam incident on a target is actually a measurement at a variety of energies spanning the target depth. This section outlines the basis of how reaction rates at astrophysical temperatures can be extracted from experiments in the laboratory when considering all of the above shortcomings.

1.2.1 Reaction Cross Sections

Cross sections are used as a quantitative way of characterizing reaction rates as a function of energy. They are formally defined in the context of a reaction rate between any interacting particle pair:

$$\frac{N_r}{t} = \frac{N_b}{t}\frac{N_t}{A}\sigma \tag{1.4}$$

Where $\frac{N_b}{t}$ is beam intensity, $\frac{N_t}{A}$ is the target area density and σ is the cross section of the reaction which is proportional to the probability that the reaction will occur, expressed in units of area, typically barn[5]. Sometimes a nuclear fusion reaction can take place through an intermediate state in a compound nucleus, for example the reaction ^{18}F(p,α) can pass through proton capture to form an excited state in ^{19}Ne before alpha decaying into ^{15}O. Such a process greatly increases the reaction's cross section, due to an overlap between the reaction channel and excited state wavefunctions (see section 1.2.4), and is referred to as a resonance. Excited states in nuclei occur at very precise energies but the reaction's cross section is not a delta function[6] centred on this value, but rather, it gradually decreases either side of the peak following the Bright-Wigner formula:

$$\sigma(E) = \frac{\lambda^2}{4\pi}\frac{(2J+1)(1+\delta_{ab})}{(2j_a+1)(2j_b+1)}\frac{\Gamma_a\Gamma_b}{(E_r-E)^2+(\Gamma/2)^2} \tag{1.5}$$

Where J is the spin of the compound system, $j_{a,b}$ is the spin of the reactant particles, λ is the de Broglie wavelength and δ_{ab} equals 1 if particles a and b are identical, zero if not. Γ_a and Γ_b refer to the partial widths of the entrance and exit channels and are directly proportional to the probability of the compound state decaying via a given channel. Using this equation we can see the large effect a resonance can have on the cross section of a reaction (displayed in figure 1.11), in fact the contribution from resonances to the total reaction rate is so great that it can be many orders of magnitude larger than that of non resonant contributions. The definitions and derivations in this section were taken from [6].

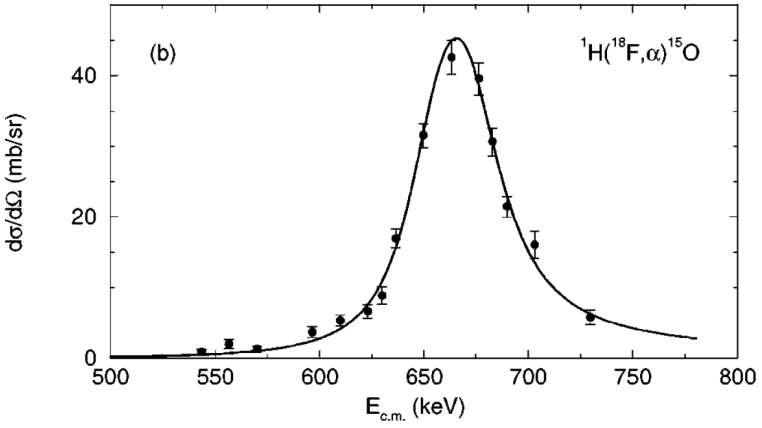

FIGURE 1.11: Graph showing a strong resonance at 665 keV in the ^{18}F(p,α)^{19}Ne reaction, in inverse kinematics. A sharp rise in the differential cross section is clearly visible where this resonance occurs. The solid line shows an R-Matrix fit (see section 1.2.4). Taken from [24].

[5] 1 barn = 10^{-24} cm

[6] a real function that is zero for all values except 0 and has an integral of 1

1.2.2 Reaction Yields in the Laboratory

Often in an experimental analysis extracting a cross section at a specific energy is not feasible, due to the thickness of the target used creating a distribution of possible energies for the reaction to occur, and so the immediate goal is to determine the ratio of the number of reactions to the number of incident beam particles:

$$Y = \frac{N_r}{N_b} \tag{1.6}$$

This quantity is referred to as the yield per incident ion. If we consider a target where energy loss per unit length is constant then using equation (1.4) and (1.6) we can deduce:

$$Y = \sigma \frac{N_t}{A} = \sigma \frac{N_t}{V} \Delta x; \tag{1.7}$$

Where Δx is the target thickness and $\frac{N_t}{V}$ is the target's particle density in volume. Extracting resonance parameters from the yield is complicated by the fact that both beam energy and cross section are varying over the course of the target. This can be properly accounted for however by including the spatial dependence of these variables and integrating over the entire depth of the target:

$$Y = \int_{x_0+\Delta x}^{x_0} \sigma(x) N(x) \, \mathrm{d}x; \tag{1.8}$$

With N being the target density at any given point. Since the Bright-Wigner cross section varies with energy, the target stopping power is needed, which tells us the rate at which the incident beam loses energy whilst traversing the target.

$$\epsilon(E) = -\frac{V}{N_t} \frac{\mathrm{d}E}{\mathrm{d}x} \tag{1.9}$$

Substituting this into equation (1.8) yields:

$$Y = \int_{E_0-\Delta E}^{E_0} \frac{\sigma(E)}{\epsilon(E)} \, \mathrm{d}E \tag{1.10}$$

For a resonant reaction we use equation (1.5) for the cross section:

$$Y = \int_{E_0-\Delta E}^{E_0} \frac{1}{\epsilon(E)} \frac{\lambda^2(E)}{4\pi} \omega \frac{\Gamma_a \Gamma_b}{(E_r - E)^2 + (\Gamma/2)^2} \, \mathrm{d}E \tag{1.11}$$

Here ω is used as a substitute for the δ and spin terms in equation (1.5). Making some more substitutions and assuming the stopping power and De Broglie wavelength remain constant over the energy range we find that equation (1.11) can be solved analytically:

$$Y = \frac{\lambda^2(E_r)}{2\pi} \frac{\omega\gamma}{\epsilon(E_r)} \left[\arctan\left(\frac{E_0 - E_r}{\Gamma/2} \right) - \arctan\left(\frac{E_0 - E_r - \Delta E}{\Gamma/2} \right) \right] \tag{1.12}$$

Where a new quantity has been defined:

$$\omega\gamma = \frac{(2J+1)(1+\delta_{ab})}{(2j_a+1)(2j_b+1)} \gamma = \frac{(2J+1)(1+\delta_{ab})}{(2j_a+1)(2j_b+1)} \frac{\Gamma_a \Gamma_b}{\Gamma} \tag{1.13}$$

This is the resonance strength and is proportional to the integral of the cross section across the resonance energy range. Specific resonance parameters, used for calculating cross sections and reaction rates, can be extracted from the solution of equation 1.11 in this way. The definitions and derivations in this section were taken from [6].

1.2.3 Reaction Rates in Stellar Environments

In simulations of stellar environments the reaction rate per unit volume is used to calculate the total energy produced at any given moment in a body. This quantity is defined, using equation 1.4, as:

$$\frac{N_r}{Vt} = r_{01} = \sigma \frac{N_t}{V} v \frac{N_b}{V} = N_0 N_1 v \sigma \tag{1.14}$$

Where N_0 and N_1 are the number densities of the interacting nuclei. In stellar plasma the relative velocity of interacting nuclei is not constant but varies with a probability function $P(v)$, defined as:

$$\int_0^\infty P(v)\ \mathrm{d}v = 1 \tag{1.15}$$

So equation 1.14 can be expressed as:

$$r_{01} = N_0 N_1 \int_0^\infty v P(v) \sigma(v)\ \mathrm{d}v = N_0 N_1 \langle \sigma v \rangle_{01} \tag{1.16}$$

The quantity $\langle \sigma v \rangle$ gives the reaction rate per particle pair and is solely dependant on nuclear structure information rather than the stellar environment and is often quoted in units of $\mathrm{cm}^3/\mathrm{mol}/\mathrm{sec}$. Using the Maxwell Boltzmann distribution the velocity distribution can be defined as:

$$P(v)\ \mathrm{d}v = \frac{m_{01}}{2\pi k T^{3/2}} e^{\frac{-m_{01}v^2}{2kT}} 4\pi v^2\ \mathrm{d}v \tag{1.17}$$

Where m_{01} is the systems *reduced mass*[7]. Combining this with $\mathrm{d}E/\mathrm{d}v = m_{01}v$ and after some re-arranging we can define the reaction rate as:

$$N_A \langle \sigma v \rangle_{01} = \left(\frac{8}{\pi m_{01}} \right)^{1/2} \frac{N_A}{(kT)^{3/2}} \int_0^\infty E \sigma(E) e^{-\frac{E}{kT}}\ \mathrm{d}E \tag{1.18}$$

Where N_a is the Avogadro constant and T is a specific temperature. If the reaction rate is primarily determined by a specific resonance then we can define the cross section as equation 1.5. Substituting this into equation 1.18 gives us:

$$N_A \langle \sigma v \rangle_{01} = \sqrt{2\pi} \frac{N_A \omega \hbar^2}{(m_{01} k T)^{3/2}} \int_0^\infty e^{-\frac{E}{kT}} \frac{\Gamma_a(E) \Gamma_b(E + Q - E_f)}{(E_r - E)^2 + \Gamma(E)^2/4}\ \mathrm{d}E \tag{1.19}$$

Here Q is the reaction Q-value defined as the mass energy difference between the products and reactants whilst E_f is the final energy state of the recoil. For a broad resonance which is loosely defined as a resonance that has a total width greater than a few keV, the

[7] For a two body system defined as: $\frac{m_0 m_1}{m_0 + m_1}$

energy dependence of the partial widths has to be taken into account due to reaction rate contributions from the cross section distribution that lie outside the resonances total width, referred to as tails. They can have a large effect on the total reaction rate and for s-wave (no angular momentum transfer) resonances below the Coulomb barrier the partial widths in these regions can be approximated to:

$$\Gamma_a(E) = \Gamma_a(E_r)\frac{e^{-2\pi\eta(E)}}{e^{-2\pi\eta(E_r)}} \tag{1.20}$$

$$\Gamma_b(E+Q-E_f) = \Gamma_b(E_r+Q-E_f)\frac{e^{-2\pi\eta(E+Q-E_f)}}{e^{-2\pi\eta(E_r+Q-E_f)}} \tag{1.21}$$

In which the Somerfeld parameter is:

$$\eta = \frac{q_a q_b e^2}{\hbar}\sqrt{\frac{1}{E}\frac{m_a m_b}{m_a+m_b}} \tag{1.22}$$

When this is substituted into equation 1.19 the resulting function cannot be solved analytically but must be tackled numerically. These methods can be used to approximately calculate reaction rates in stellar environments, using experimentally obtained data in the laboratory, however they fail to take into account the phase mixing between states with the same spin and parity (see the next section for more details). The definitions and derivations in this section were taken from [6].

1.2.4 R-Matrix Theory

The theory pertaining to capture reactions forming a compound nucleus, presented earlier in this section, is only technically valid for the case of an isolated resonance. In the case of multiple levels in the compound nucleus, which is a typical scenario, separate resonances may interfere with each other, resulting in phase mixing that can alter the reaction's resulting cross section at a variety of energies. The R-Matrix (Reaction Matrix) theory provides a mathematical formalism that can be used to address such issues. The following is a very brief introduction to the subject, for a more complete description the reader is referred to [25].

The basic framework of this method involves defining a *nuclear surface*, within which all nucleons are considered to be a part of the compound nucleus. Conversely, outside of this same surface particles are considered to be separate entities. Such a model with a well defined boundary can be considered due to the short range nature of the strong nuclear force. All of the possible particles that can exist outside of this surface constitute the various reaction channels that populate the compound state. Figure 1.12 illustrates the situation when populating the ^{19}Ne nucleus, as was the case for the experiment expounded in chapter 3.

In a quantum mechanical system, particles can be considered as waves with an associated wavefunction. Various properties of the particle and its environment define such a mathematical function. In the R-Matrix formalism the internal and external regions are deemed separate enough that the reaction channel wavefunctions are constructed quite separately from the interior ones. Each excited state in the compound nucleus corresponds to a distinct stationary wavefunction within the nuclear surface; when the external wave overlaps with this

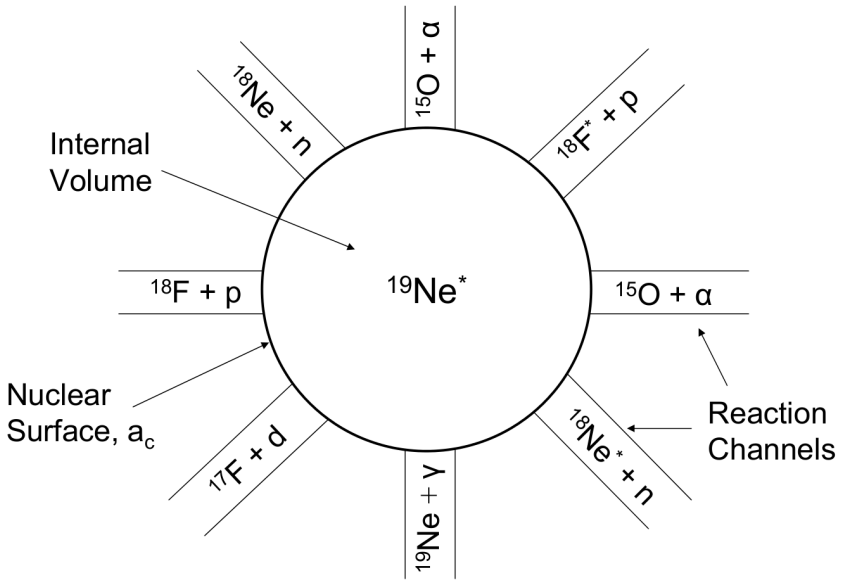

FIGURE 1.12: Visual outline of various reaction channels separated from the internal volume of the compound nucleus, at the nuclear surface. Taken from [26].

the reaction's cross section is greatly enhanced, leading to resonances at energies corresponding to specific states. Certain properties of the compound nucleus have to be determined experimentally, such as the position (E_x), strength ($\omega\gamma$) and widths (Γ_i) of individual states, and so the theory is phenomenological in nature.

Once the relevant wavefunctions have been constructed they are combined to form what is termed a *collision matrix* from which cross sections can be extracted at specific energies. Hence the theory can provide, with the aid of experimental data, a complete description of a reactions cross section that properly accounts for the interference between excited states in the compound nucleus. It should be noted however that only those states with an identical spin and parity (J^π) will interfere in such a way as to alter the resulting cross section.

1.2.5 Reciprocity Theorm

Often in experimental physics the time reverse of a desired reaction rate is measured so as to enable the forward rate to be calculated. Such a situation arises when the observation of a reaction is not possible due to experimental constraints, and an experiment involving the time reverse counterpart is deemed more feasible. In order to relate the forward and reverse reaction rates we must first consider the fact that under stellar conditions ions are not all in their ground state, but rather they have a distribution of states that is dependant on the temperature of the plasma they are in. This complicates matters somewhat as, in the laboratory, we measure the reaction rate with the target (or projectile in the case of inverse kinematics) in its ground state, and so we measure the cross section for just the transition originating from the target's ground state. Figure 1.13 illustrates the situation for a reaction, $A(a,b)B$, occurring through a compound state in a nucleus C, only the transition from A_0 to the compound state is observed, labelled as a_0.

The rate we deduce from experiments then is not the stellar rate but just the ground state contribution to the rate. The ratio R^*/R_0 is used to quantify how the ground state rate differs to the stellar rate, and is termed the *stellar enhancement factor* (f_{SEP}). Here, R_0 is the reaction rate per particle pair from the ground state and R^* is the rate per particle pair under stellar conditions, equivalent to $\langle \sigma v \rangle$ (defined in equation 1.16) when the cross section under stellar conditions is used, defined as:

$$\sigma^*(E,T) = \frac{\sigma^{eff}}{G_0(T)} \tag{1.23}$$

where σ^{eff} is called the effective cross section, which is a weighted sum of over every energetically accessible transition's cross section:

$$\sigma^{eff} = \sum_i \sum_j \frac{(2J_i+1)}{(2J_0+1)} \frac{E-E_i}{E} \sigma^{i\to j}(E-E_i) \tag{1.24}$$

Here i represents every possible intial state and j every accessible final one. G_0 is the partition function, normalized to the ground state spin of the target nuclei:

$$G_0 = \sum_i \frac{(2J_i+1)e^{-E_i/(kt)}}{(2J_0+1)} \tag{1.25}$$

We can now use this reaction theory to relate the forward ($A(a,b)B$) and reverse ($B(b,a)A$) reaction rate with the equation [27]:

$$\frac{R^*_{Bb}}{R^*_{Aa}} = \frac{(2J^A_0+1)(2J_a+1)}{(2J^B_0+1)(2J_b+1)} \frac{G^A_0(T)}{G^B_0(T)} \left(\frac{m_{Aa}}{m_{Bb}}\right)^{3/2} e^{-Q_{Aa}/(kT)} \tag{1.26}$$

J^A_0 and J^B_0 are the ground state spin of the target and ejectile respectively or, in the case of inverse kinematics, beam ion and recoil. J_a and J_b are the spins of the light particle reactant and product, usually an alpha particle, proton or gamma ray. For the case when b is a photon, equation 1.26 becomes:

$$\frac{R^*_{B\gamma}}{R^*_{Aa}} = \frac{(2J^A_0+1)(2J_a+1)}{(2J^B_0+1)} \frac{G^A_0(T)}{G^B_0(T)} \left(\frac{m_{Aa}kT}{2\pi\hbar^2}\right)^{3/2} e^{-Q_{Aa}/(kT)} \tag{1.27}$$

1.2.6 Gamow Window

In stellar plasmas most nuclear reactions occur over a relatively small energy range, referred to as the *Gamow peak* or *Gamow window*. To understand the reasons for such behaviour we must first define the *astrophysical S-factor* ($S(E)$) as:

$$\sigma(E) = \frac{1}{E} e^{-2\pi\eta} S(E) \tag{1.28}$$

Where all of the variables have been defined earlier in this section. The S-factor removes both the $1/E$ dependence and Coulomb barrier transmission effects from the cross section. Substituting this equation into the reaction rate formula (equation 1.18) gives:

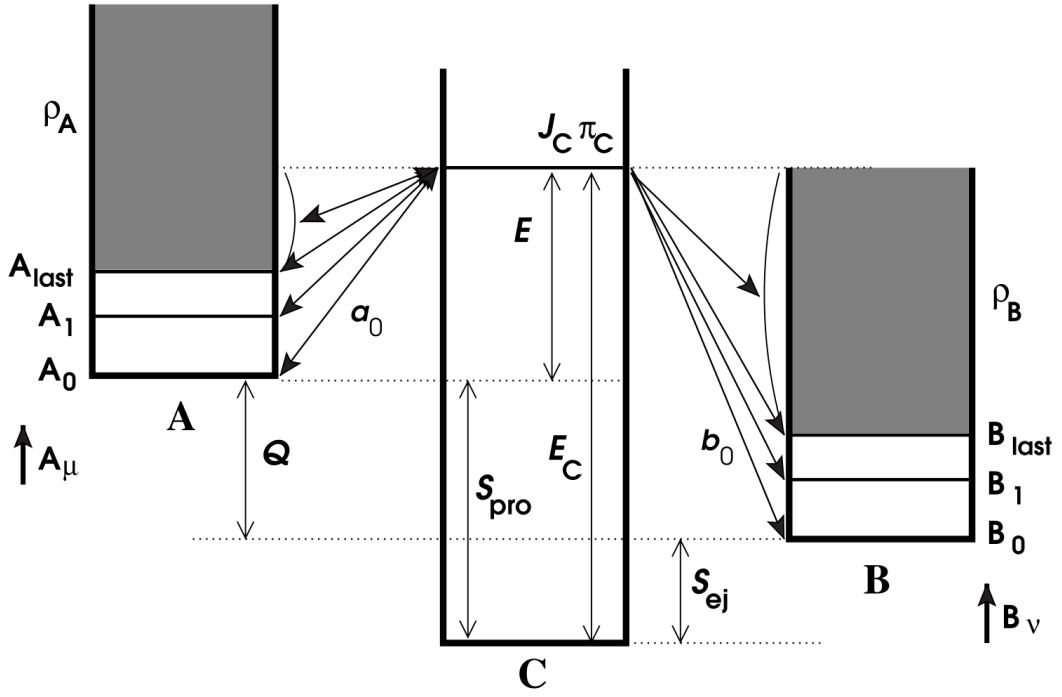

FIGURE 1.13: Energy level diagram of the reaction $A(a,b)B$ taking place through an excited state in the compound nucleus C. In a laboratory experiment only the transition from A_0 to the compound state is observed, labelled as a_0. Taken from [28].

$$N_A\langle\sigma v\rangle_{01} = \left(\frac{8}{\pi m_{01}}\right)^{1/2} \frac{N_A}{(kT)^{3/2}} \int_0^\infty e^{-2\pi\eta} e^{-\frac{E}{kT}} S(E)\,\mathrm{d}E \tag{1.29}$$

And if $S(E)$ is a constant (S_0), such is approximately the case with a non resonant reaction, then we have:

$$N_A\langle\sigma v\rangle_{01} = \left(\frac{8}{\pi m_{01}}\right)^{1/2} \frac{N_A S_0}{(kT)^{3/2}} \int_0^\infty e^{-2\pi\eta} e^{-\frac{E}{kT}}\,\mathrm{d}E \tag{1.30}$$

The majority of the contribution to the overall reactions rate at a given temperature comes from the region where the product $e^{-2\pi\eta}e^{-\frac{E}{kT}}$ is at, or close to, its maxima. The situation is illustrated in figure 1.14, where this product is plotted for the reaction ^{18}F(p,γ)^{19}Ne at T=0.4 GK; it can be seen that the resulting function takes the approximate form of a Gaussian distribution. This peak is referred to as the Gamow window and is where, for non-resonant reactions, the majority of the overall reactions rate comes from. For resonant reactions however, the situation is somewhat more complicated and the conventional Gamow window can only be used as a first approximation as to the energy region dominating the reactions rate.

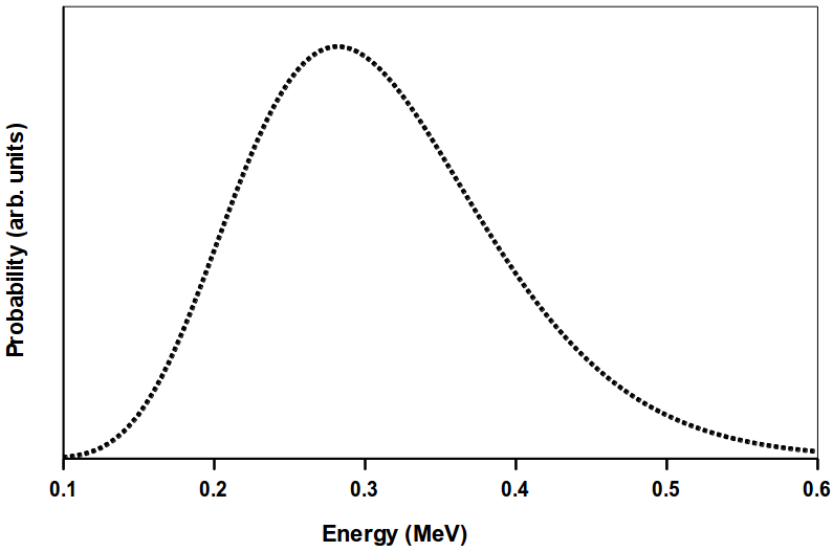

FIGURE 1.14: The product $e^{-2\pi\eta}e^{-\frac{E}{kT}}$ for the reaction ^{18}F(p,γ)^{19}Ne at T=0.4 GK. A clear peak can be seen around 0.3 MeV, forming the Gamow window.

Chapter 2

Experimental Approaches

2.1 TRIUMF

The TRI University Meson Facility (TRIUMF) is Canada's national laboratory for nuclear and particle physics research, located on the University of British Columbia campus in Vancouver, Canada. Both of the experiments expounded in this thesis were conducted here utilizing the laboratory's radioactive and stable beam capabilities. This section gives a brief overview of the laboratory's facilities and capabilities.

2.1.1 ISOL

The Isotope Separator and Accelerator (ISAC) is a facility located at TRIUMF which is used for generating rare-isotope beams (RIB) using the Isotope Separation On-Line technique (ISOL). This method works by having a primary beam incident on a thick target creating a multitude of spallation, fragmentation and fission reactions which produce the desired beam nuclide. At TRIUMF a cyclotron is used to create 500 MeV protons that embody the primary beam, these are stopped completely in the target material with any products diffusing from the target into the ion source where they are ionized to charge state 1^+ for subsequent re-acceleration. Before being sent to the experimental halls this ion beam is separated via an isotope separator which bends different mass particles at different radii using a magnetic field, with slits then being used to select a single mass with high precision. See figure 2.1 for a schematic of the ISOL process.

2.1.2 ISAC-I

After the mass separator the beam is transported into the Low Energy Beam Transport section (LEBT) consisting of an electrostatic beam line and switch-yard, which is used to channel the ions into the low energy ISAC-I experimental hall. The first stage of ISAC-I comprises a pre-buncher and radio frequency quadrupole (RFQ), used to accelerate particles with an A/q of up to 30 to an energy range of 2→150 keV/u. The pre-buncher bunches the beam to the third sub harmonic of the RFQ resonant frequency, 11.7 and 35 MHz respectively, improving its quality and transmission. An 11 MHz chopper located directly downstream of the RFQ is used to remove satellite peaks formed during the bunching process. The beam then passes

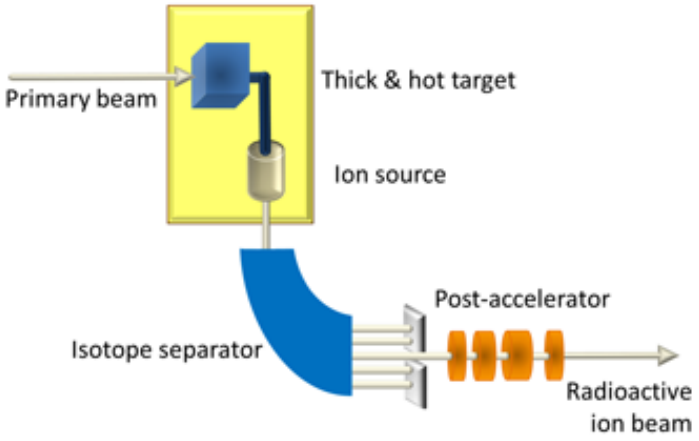

FIGURE 2.1: Schematic of ISOL beam production at TRIUMF, taken from `http://isolmyrrha.sckcen.be/en/Introduction`.

through the Medium Energy Beam Transport section (MEBT) where its charge state is then increased by means of a carbon stripping foil, the efficiency of which varies between 30→50% depending on the nuclide, before being rebunched in the MEBT rebuncher and entering the Drift Tube Linac (DTL). This machine consists of eight modules: five accelerating structures and three bunchers which accelerate the beam to an energy range of 150 keV/u→1.9 MeV/u for an A/q range of 2→6. A downstream buncher allows for further bunching from 1→4 ns or greater energy resolution in the range of 0.1→0.4%, after which the beam is delivered to the High Energy Beam Transport section (HEBT) where it is directed to the desired experimental apparatus. See figure 2.2 for a schematic of ISAC-I.

2.1.3 OLIS

In addition to ISAC, TRIUMF is also equipped with an Off-Line Ion Source (OLIS) which consists of a microwave cusp, surface and multicharge (supernanogan) ion source [29, 30], providing stable beams from gaseous, liquid and solid elements. Figure 2.3 gives a schematic of the facility.

2.2 DRAGON

The facility called DRAGON (Detector of Recoils And Gamma-rays of Nuclear reactions) is situated in the ISAC-I experimental hall at TRIUMF (see figure 2.4) and was designed specifically to measure the cross sections of radiative capture nuclear reactions at astrophysical energies. It consists primarily of a windowless gas target, γ-ray detection array, electromagnetic separator and a set of particle ID detectors for measuring energy loss and time of flight (see figure 2.5). Radiative capture reactions are an important step in nucleosynthesis for a variety of stellar scenarios, however their direct observation is complicated by the sub Coulomb barrier energies involved. DRAGON's architecture was constructed to deal with

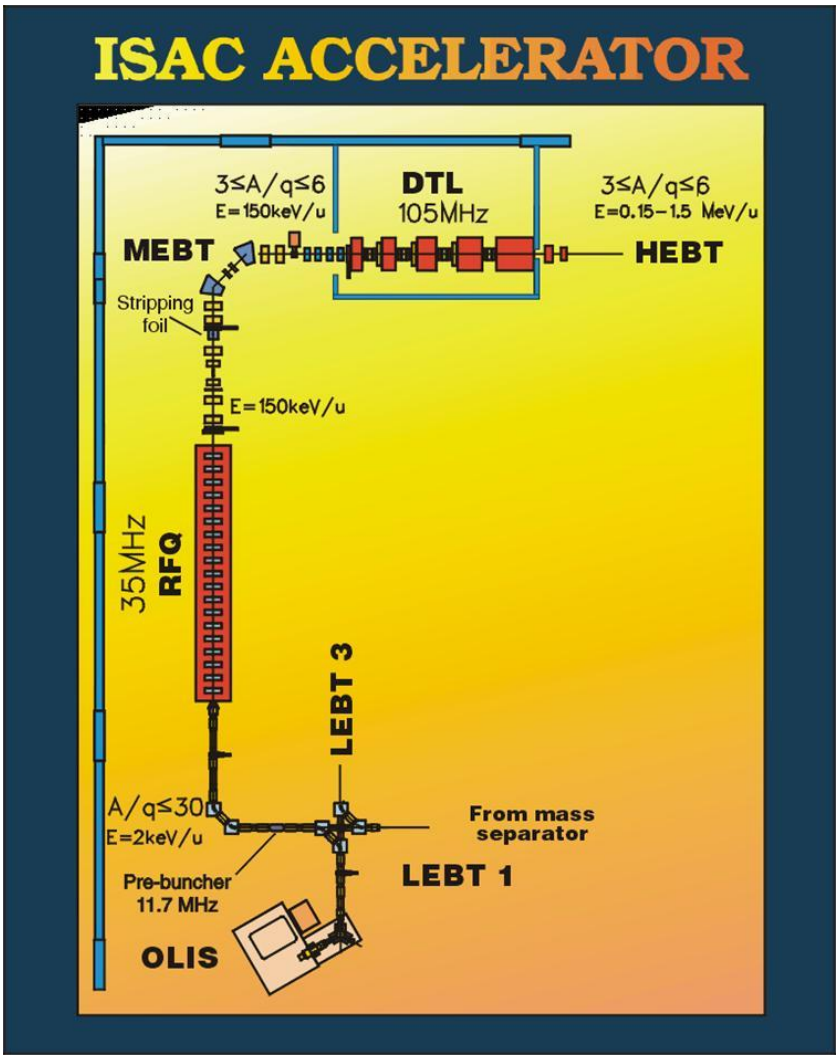

FIGURE 2.2: Drawing of ISAC-I beam transportation and acceleration facility at TRIUMF.

such low yields with an extremely high background suppression, meaning that only a small number of reactions inside the target are required to extract reliable limits on measurements.

2.2.1 Gas Target & Pumping System

Beam enters DRAGON via a windowless gas target which is filled with either hydrogen or helium for observation of either (p,γ) or (α,γ) reactions respectively. The energy spread of ISAC beams ($\approx$1 keV/u FWHM), coupled with frequent uncertainty in the energy of specific resonances of interest, require the use of a dense, long target. This ensures the resonance or energy region of interest resides within the target region due to a relatively large beam energy loss across its length. A limit on the target length is provided by the need for a tight recoil cone angle to ensure transmission through the separator stage. Consequently the distance between the two innermost apertures, which define the length of the target gas volume, is 11 cm although the target's effective length varies between 12$\rightarrow$13 cm [31] depending on gas pressure, which has a limit of 8 Torr due to pumping constraints. Two silicon detectors are also located inside the target chamber for the purposes of monitoring beam intensity, via

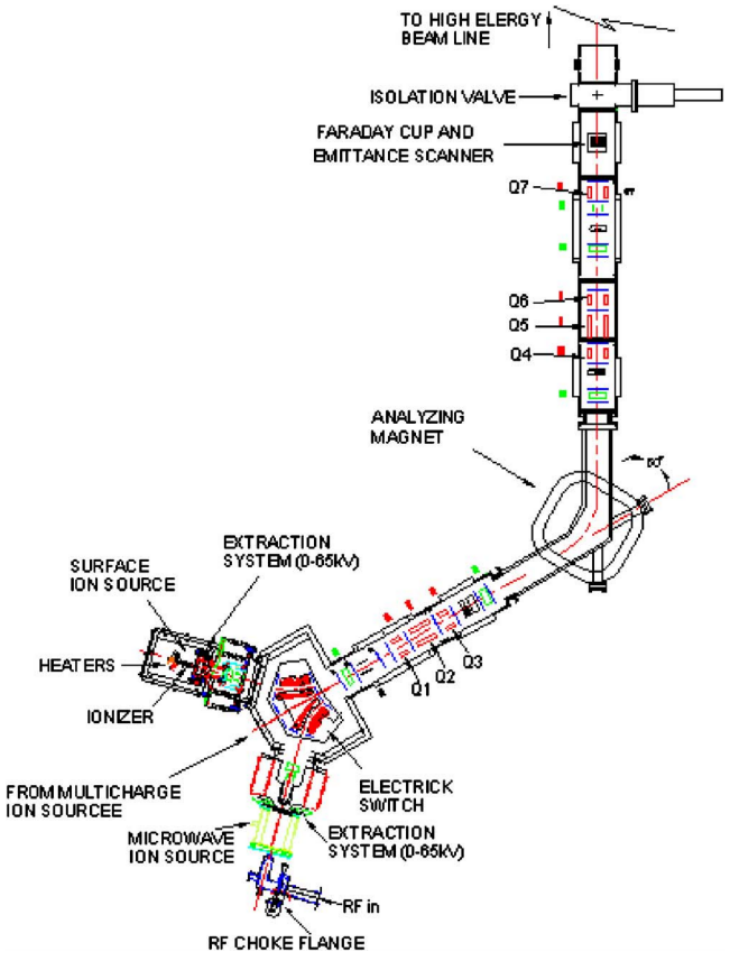

FIGURE 2.3: Outline of the OLIS facility located in the ISAC-I hall. Taken from [29].

elastic scattering on the target nuclei. The target is enclosed inside an aluminium pumping target box designed with thin walls to minimize the attenuation of prompt γ-rays produced inside the target. Feedthoughs in the lower section of the box allow for detector and sensor cables, that measure target pressure and temperature, together with a gas supply line (see figure 2.6). The target chamber's trapezoidal shape, resulting from the lower plane being smaller than the top plane, aids the pressure differential by deflecting jets of gas leaving the cell away from the pumping tubes.

Gas that leaks into the target box through the central chamber apertures is removed and recirculated via a series of Roots blowers consisting of: two Leybold WSU2001 (in parallel), two WSU501 (in parallel) and one WS500 (as shown in figure 2.7). These raise the gas-flow pressure to >40 Torr before channelling it into a liquid nitrogen cooled Zeolite trap, where 21 molecular sieves absorb the hydrogen or helium creating a ≈10 second delay in recirculation. This buffer of gas adds to target pressure stability which is observed to remain within 1% of its value without user intervention. The beam-line either side of the target box consists of a series of pumping tubes which are pumped via seven Varian V1000HT turbo molecular pumps. These pumping tubes are tapered both sides of the target to converge towards it, accommodating beam shape and recoil cone angles, as shown if figure 2.8. This differential

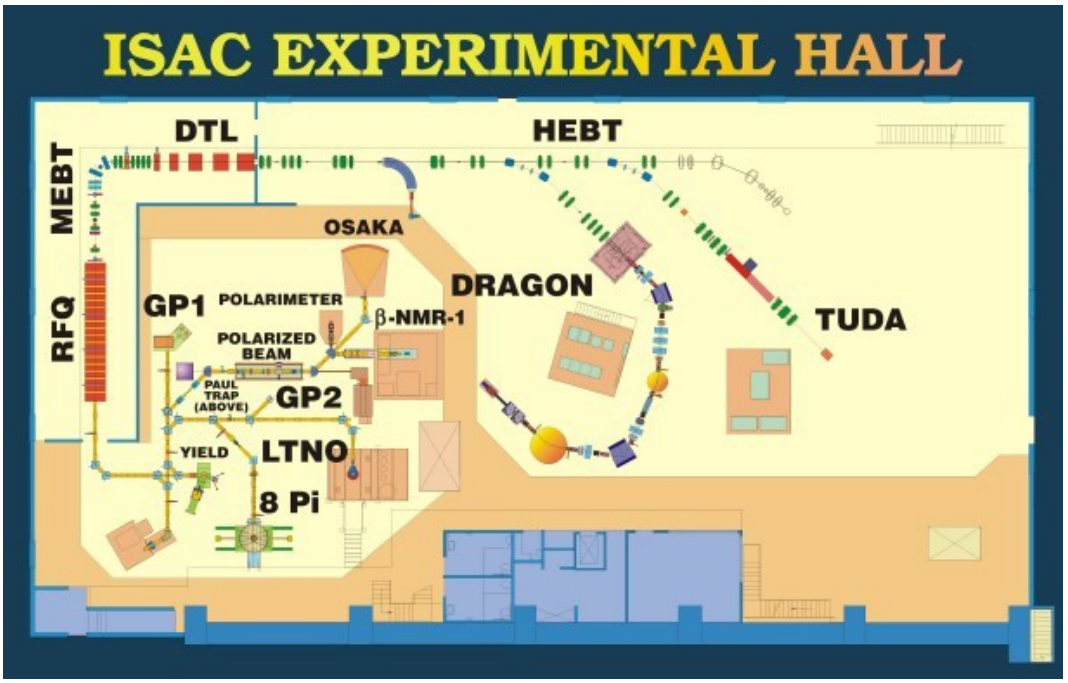

FIGURE 2.4: Schematic showing the location of DRAGON in the ISAC-I experimental hall. Taken from `http://www.sfu.ca/triumf/isac.htm`.

pumping system allows for a large drop in pressure ($< 3 \times 10^{-6}$ Torr) down and upstream of the outermost turbo pumps, which is important when considering the final charge state of beam and recoil ions.

2.2.2 Elastic Scattering Detectors

Located inside the central chamber are two ORTEC Ultra Cam silicon detectors, one is mounted at a 30° angle to the incoming beam and the other at 57°, their position is illustrated in figure 2.6. Both detectors are collimated to view the central section of the gas target and, in tandem with Faraday cup readings, are used to normalize beam intensity. This is done using the fact that for a given number of target nuclei the rate of elastic scattering resulting from a beam of ions is directly proportional to the intensity of the given beam. In the presence of a stable target pressure, as is usually the case with DRAGON, this means that the detection rate on the silicon detectors can be directly related to beam intensity on target.

2.2.3 BGO γ-array

Surrounding the target box is a γ-array comprised of 30 BGO scintillation detectors allowing for the detection of prompt γ-rays produced inside the target. Their hexagonal shape allows for two tessellated side arrays, each with 10 detectors, flanking the chamber with the remaining 10 crowning the top and sides for optimal solid angle coverage, in the range of 89→92 % (see figure 2.9). The array allows for the observation of coincident γ events with potential recoil events and so aids particle identification. As such, a good timing resolution and high γ detection efficiency was required in order to minimize false negative recoil coincidence events

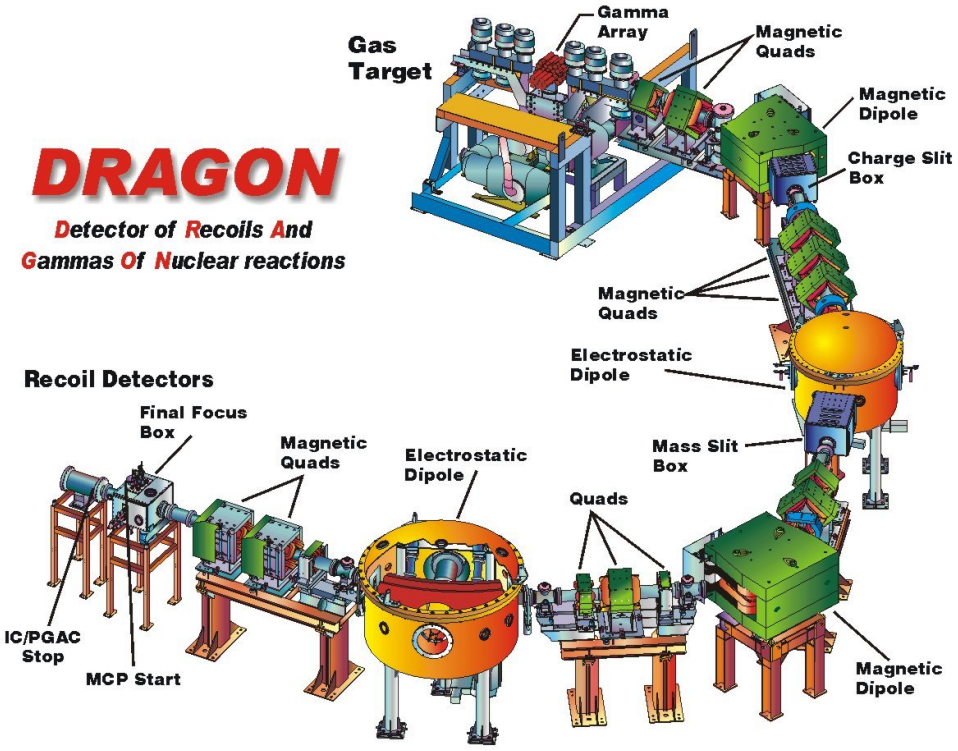

FIGURE 2.5: Drawing of the DRAGON facility at TRIUMF. Beam enters via the gas target at the top of the diagram. Taken from `http://dragon.triumf.ca/system.html`.

in the presence of high intensity radioactive beams. The BGO crystals were selected for these reasons, and were coupled with cylindrical photomultiplier tubes which gave an energy resolution of 7% full width half maximum at 6.13 MeV.

The detectors have a face 57.8 mm across whilst their PMT's measure 51 mm in diameter. Their crystals are surrounded by a 0.0355 mm thick layer of MgO, a highly reflective material designed to maximize detection efficiency, which is in turn surrounded by a 0.5 mm thick layer of Al. The two crowning detectors upstream of the target are retracted by 7.3 cm to accommodate lead shielding, designed to reduce 511 keV beam induced background from the target apertures. Figure 2.10 gives a more detailed picture of the detectors.

2.2.4 Electromagnetic Recoil Separator

For capture reactions, momentum conservation means that recoil nuclei move forward at almost (see later) zero degrees causing them to be immersed within the much more numerous unreacted beam particles. The DRAGON recoil separator is comprised of a complex arrangement of electric and magnetic fields that allow for the recoil products of interest to be separated from beam ions and transmitted to a focal plane for detection. The situation is somewhat complicated by the fact that recoils are not formed with identical trajectories, they are dispersed due to the momentum kick received when the prompt gamma is emitted. This gives them a cone shaped dispersion in the laboratory frame and the separator can only accept those that lie within a certain angular range of the beam axis. Care is taken with preliminary calculations to make sure that the reaction of interest will produce recoils that

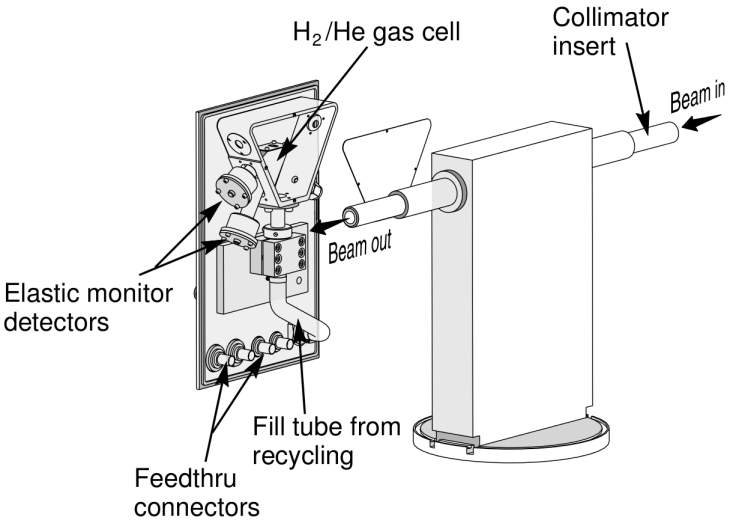

FIGURE 2.6: Scale drawing of the target box at DRAGON with the central chamber piece retracted, taken from [31].

lie within this range, or if not, simulations run to properly characterize the number lost. DRAGON's separator has an acceptance angular range of ±20 mrad [31] which is more than adequate when considering most (p,γ) and (α,γ) reactions of astrophysical interest.

The separator consists of a series of magnetic and electric dipoles (MD's & ED's), for beam suppression, interspersed with magnetic quadruples and sextupoles for focusing. Both magnetic dipoles are equipped with Nuclear Magnetic Resonance (NMR) probes allowing for precise readings of field strength. Recoils are transmitted with a high efficiency, typically >95%, to a focal plane consisting of a series of particle ID detectors which allow for recoil events to be discerned from any stray beam particles that have been scattered or involved in charge exchange with residual gas.

Due to the mono-energetic beam, energy loss in the target scaling linearly with Z^2, and the zero rest mass of γ emission, beam and recoil ions leave the target with approximately the same momentum. In addition to this, charge exchange in the target disperses the charge state of passing ions, all of which is problematic when considering beam suppression. The solution relies on having a series of two magnetic and electric dipoles (named MD1 and 2 and ED1 and 2) with the former separating the beam with respect to charge state and momentum, and the latter separating the remaining ions in mass. See figure 2.11 for the precise location of the dipoles relative to the gas target, and Table 2.1 for a list of geometric and performance properties.

For a more quantitative description consider the Lorentz force which describes the force acting on a point charge when subjected to an electromagnetic field:

$$\mathbf{F} = q(\mathbf{E} + \mathbf{v} \times \mathbf{B}) \tag{2.1}$$

Here q is the charge on the ion, $\mathbf{E}$ is the electric field vector, $\mathbf{B}$ is the magnetic field vector, $\mathbf{v}$ is the ions velocity vector and $\mathbf{F}$ is the resultant force on the ion. In the presence of just a magnetic field perpendicular to the ions trajectory, such as that present in DRAGON's MD's,

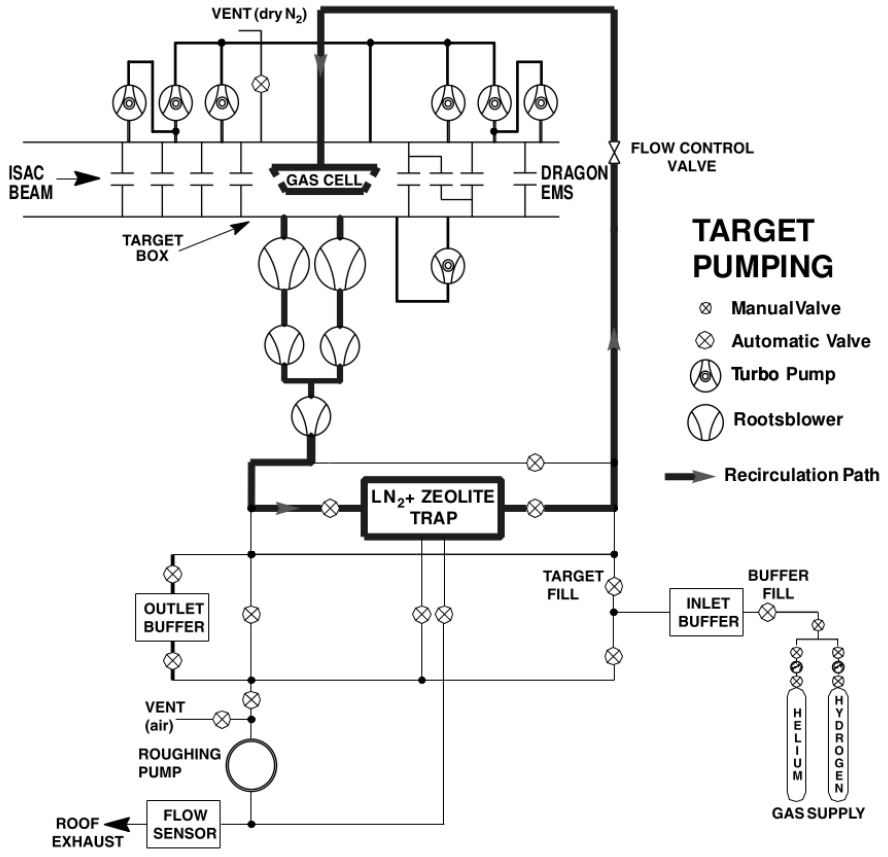

FIGURE 2.7: Outline of DRAGON's recirculation system showing all major components, taken from [31].

equation 2.1 is simplified and, using the equation for centripetal force, can be presented in the context of a radius of curvature for the ion's trajectory:

$$r = \frac{p}{qB} \tag{2.2}$$

Where p is the momentum of the particle. This is a measure of how significantly the dipoles displace the ions trajectory. Slits are located after MD1 to select those with a specific radius, here equivalent to magnetic rigidity ($\frac{p}{q}$) for a given field B, to be transmitted through to the rest of the separator. The MD's field can be tuned to transmit just ions which have a rigidity corresponding to recoil events in their most abundant charge state. As radiative capture permits the prompt gamma(s) to be emitted in a variety of directions, recoils produced have a distribution of energies and can also be produced at a variety of positions along the target, depending on the resonance width, meaning that they lose a varying amount of energy in the gas before entering the separator. This results in the recoil's most abundant rigidity being a non singular value but rather a distribution of values, requiring the charge slits to be wide enough to transmit the vast majority of them. The major drawback of this is that inevitably some beam ions will pass though the slits as their rigidity is also a distribution, characterized by tails that can overlap with the recoil's distribution.

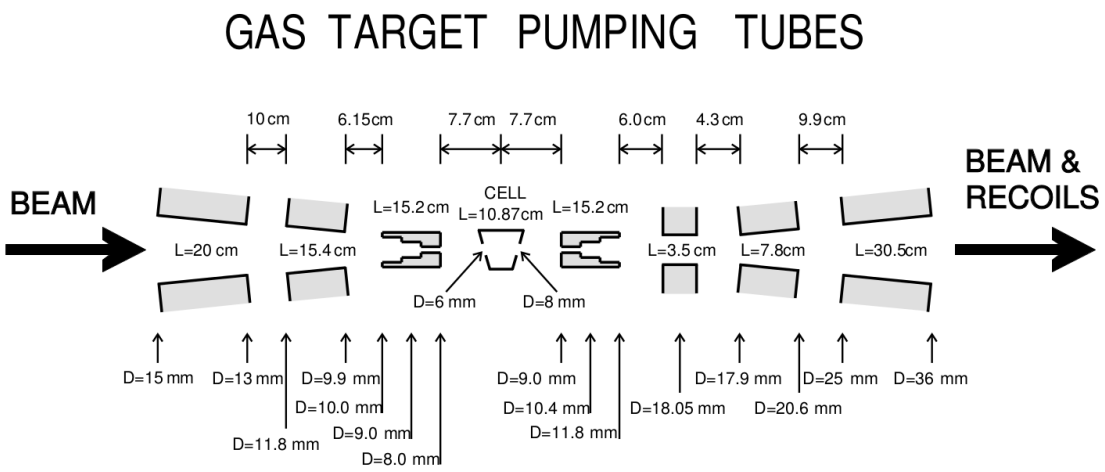

FIGURE 2.8: Schematic of the pumping tubes located either side of the central chamber, taken from [31].

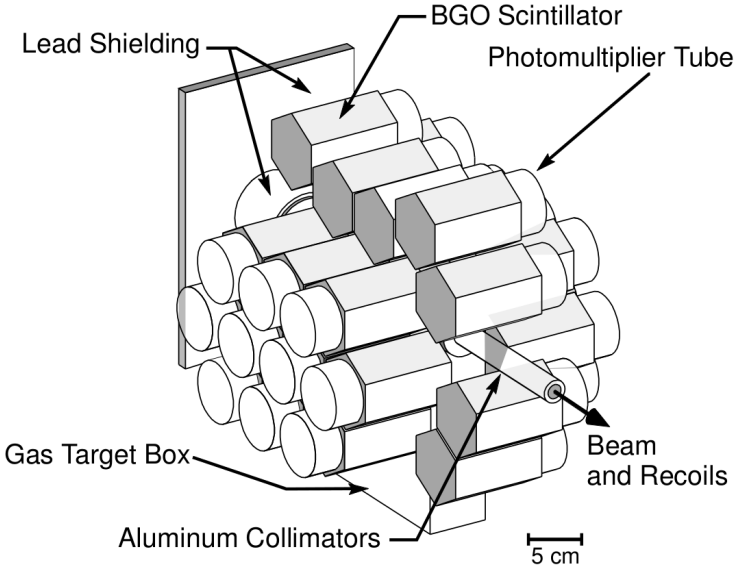

FIGURE 2.9: Drawing of the BGO gamma array surrounding DRAGON's gas target, taken from [31].

As the number of beam ions sent through the target is far greater than the number of recoils produced, usually by the order of $\approx 10^{10} \rightarrow 10^{15}$ for astrophysical reactions, just MD's are not sufficient for the purposes of beam suppression, hence two ED's are also utilized. If we now consider equation 2.1 in the context of just an electric field acting perpendicular to the ions trajectory then the radius of curvature becomes:

$$r = \frac{vp}{qE} \tag{2.3}$$

This requires that ions with the rigidity selected to pass through MD1 must also have a specific magnitude of velocity (v) to pass through the slits located after ED1 (mass slits). As the momenta of recoil and beam ions are so similar but their mass different, their velocity

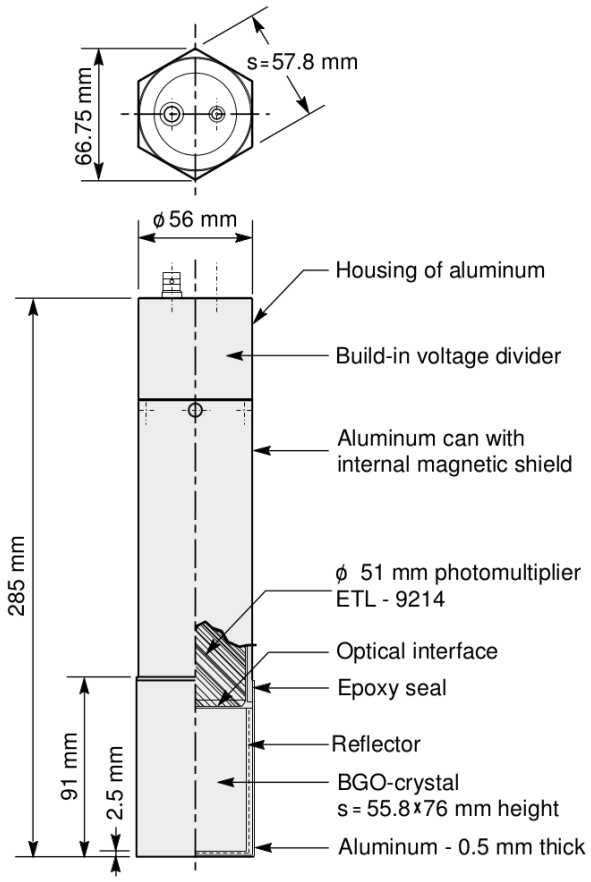

FIGURE 2.10: Schematic of one of the BGO gamma detectors, taken from [32].

must be different too, such that their radius of curvature is distinct, allowing them to be blocked by the mass slits. As with the MD however, beam particles are not bent into an infinitely narrow trajectory as they pass through the ED, their radius of curvature has a distribution of values tailing either side of a peak value allowing some ions at the extremities to pass unimpeded. As such, the combination of MD and ED is repeated to further reduce the abundance of these leaky beam ions at the end detectors. Test measurements have shown that this arrangement can produce very high beam suppression, in the region of $\approx 10^{-10} \rightarrow 10^{-15}$ leaky beam events per beam ion on target, depending on the beam and target species [34]. Such a high suppression allows DRAGON to push the current boundaries of what astrophysical reactions can be observed experimentally. A detailed description of the procedure necessary to tune a beam through the separator is given in A.

2.2.5 Ion Chamber

The ion chamber at DRAGON consists of a central isobutane gas volume containing four separate anode plates for charge collection, with a thin Mylar foil covering the chamber's entrance. Ion chambers rely on the fact that as fast ions, such as recoil nuclei, travel through gas they ionize molecules creating ion pairs, which are positively charged ions accompanied by free electrons. Such ionization is achieved via the impulse felt by electrons surrounding the gas molecules caused by the coulomb force of the incident ion.

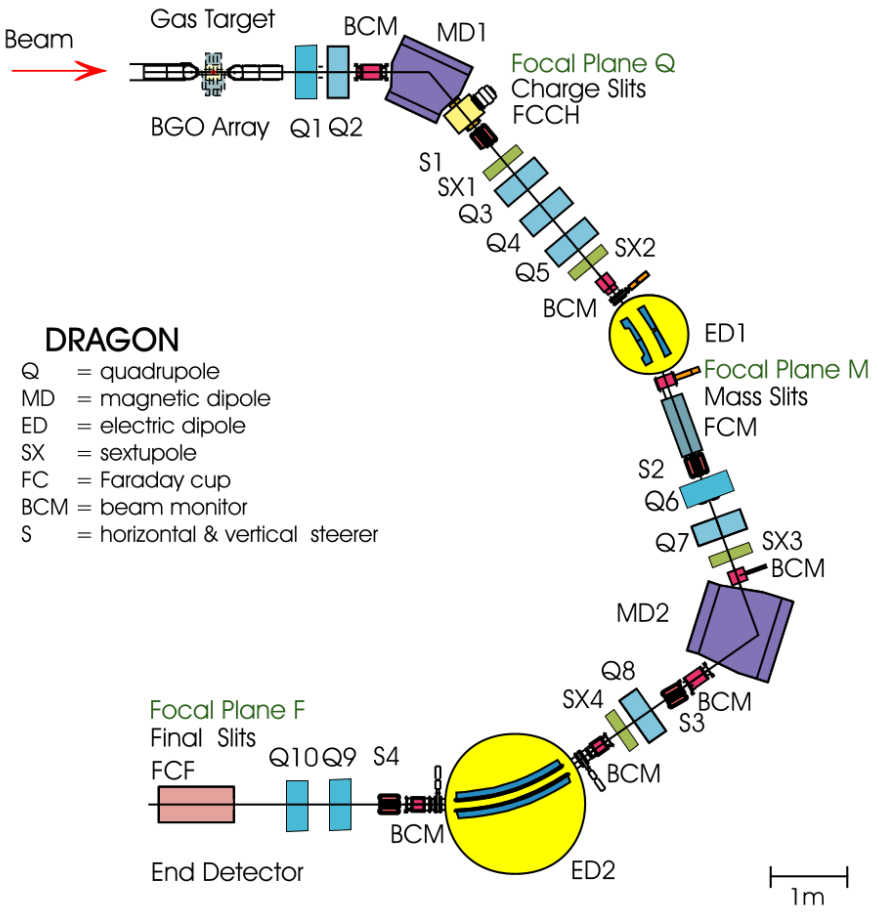

FIGURE 2.11: Scale drawing outlining of DRAGON's recoil separator showing the location of important elements relative to the gas target. Taken from [33].

Magnetic dipole property	MD1	MD2
Bending radius	1.00 m	0.813 m
Bending angle	50°	75°
Maximum field (@500 A)	5.9 kG	8.2 kG
Electric dipole property	ED1	ED2
Bending radius	2.00 m	2.50 m
Bending angle	20°	35°
Height of electrodes	280 mm	300 mm
Maximum voltage	±200 kV	±160 kV

TABLE 2.1: Magnetic and electric dipole properties

A voltage is applied across the gas volume via anode and cathode plates across its length, see figure 2.12 for a schematic representation. The resulting electric field causes free electrons produced to drift towards the anodes, inducing a current in them, which constitutes the detector's output signal. If the field is strong enough then all of the ion pairs produced will completely separate in this way, resulting in *ion saturation*. Several processes, such as inelastic scattering, compete with ion pair formation in the gas so that not all of the energy

transfered by the incident ion is lost in this way. As a result not all of the energy lost by the ion in the gas volume is detected via the anodes, reducing the detector's energy resolution.

As the signal from the anode is generated from the drift motion of the electrons, the height and shape of the resulting pulse depends on the point of ion pair creation [35]. A *Frisch grid* is often used to remedy this situation. This consists of an electron transparent grid that separates the cathode and anode, with an intermediate voltage. The electrons are initially drawn to the grid without inducing any current on the anode, only their subsequent motion after passing the grid produces an electronic signal. As a result such a grid improves the detector's timing and resolution.

The chamber at DRAGON has four anodes (referred to as IC0, IC1, IC2 and IC3, ordered sequentially in position from front to back) along its length as this allows the incident ions energy loss to be characterized as a function of depth. As different species of nuclei lose energy at different rates in gas this information can then be used to help discern which species has been observed, aiding particle identification.

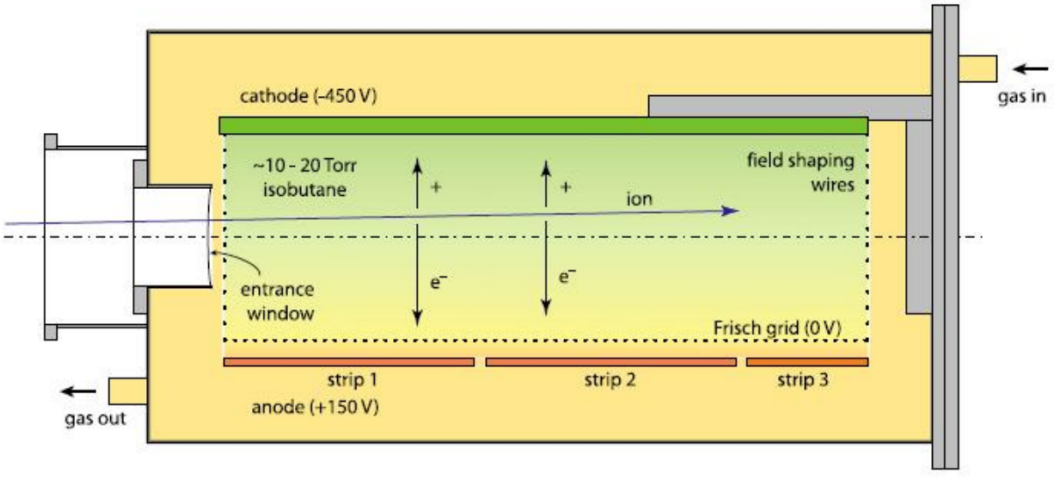

FIGURE 2.12: Schematic of DRAGON's ion chamber showing the location of the cathode, anodes and Frisch grid. Note that four anodes were actually used for the experiments described in this thesis. Taken from [36].

2.2.6 Multi Channel Plate Detectors

DRAGON is equipped with two multi channel plate detectors (MCP's) which allow for time of flight measurements of incident ions. MCP's work by having a series of hollow semi conducting cylinders that function as secondary electron emitters, such that a single incident electron can produce a cascade of output electrons creating a discernible signal from the detector. At DRAGON thin carbon foils are placed along the beam axis causing electrons to be liberated by incident ions. These subsequently travel downstream to a biased grid of wires at 45° to the beamline and deflected to the MCP located vertically above.

The two MCP's located after the separator[1] have very good timing resolution and thus can be used to calculate a time of flight for a given section of beamline when used in tandem.

[1]See figure A.1 for their exact location.

As recoil products and beam ions have differing energy and mass they also have differing velocity, hence the time of flight between MCP's provides particle identification. The carbon foils needed for electron generation are so thin that they do not interfere appreciably with the ions energy or trajectory allowing for this system to be used in parallel with the ion chamber located directly downstream.

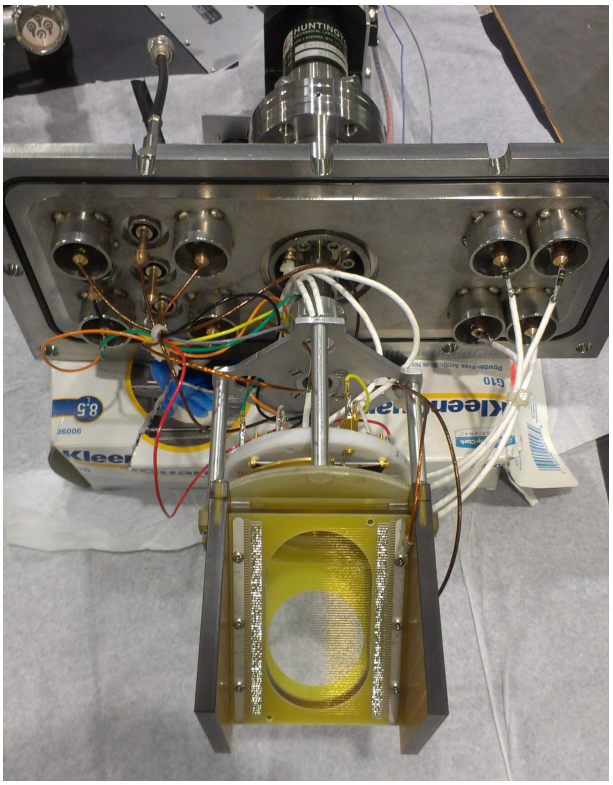

FIGURE 2.13: Photograph of one of DRAGON's MCP mounts. The carbon foil is removed showing the biased wires at 45° used to deflect electrons onto the MCP's, located on the piece of white plastic directly above.

2.2.7 Detector Electronics and Data Acquisition System

DRAGON's Data Acquisition System (DAQ) needs to be able to trigger on individual ion events (at the focal plane) and gamma events (at the target) and promptly recognize them as being singular or coincident with one another for the purposes of data analysis. This was previously done using hardware gating but was later upgraded to a timestamp based system. The former was utilised for the experiment described in chapter 3 and the latter was used for the experiment described in chapter 4.

The Hardware Gating Based System

The previous DAQ used a combination of trigger logic to identify coincident ion events by processing signals from both the gamma array detectors and the end detectors simultaneously. All of the electronics were enclosed in two nuclear instrumentation modules (NIM), one computer automated measurement and control (CAMAC) frontend system and one Eurocrate

powered chassis. All 30 outputs from the BGO photomultiplier tubes (PMT's) were fed into resistive splitters, one output going to an analogue to digital converter (ADC) the other to an amplifier where the signal is split again. From here one output was fed to a leading edge discriminator (LED) and the other to a constant fraction discriminator (CFD). The latter are then sent to an OR gate for all 30 signals in order to produce a master gate signal for gamma events which is fed to the ADC and TDC, which process the signal data and sends it to a memory buffer. The logical OR gate sets the event start time and implements a hardware voltage threshold, usually corresponding to an event depositing 0.5→2 MeV, which must be exceeded in at least one BGO detector signal for the event to be written to memory. The master gate is 20 μs long which creates a delay triggering all 30 ADC's to process their input signals, making the system blind to other events. Due to multiple decay cascade scenarios and Compton scattering within the detectors it is possible for multiple BGO detectors to register hits from a single event, in which case their signals are also analyzed by the ADC's during the same master gate generation phase. Figure 2.14 outlines the gamma array electronics in the form of a block diagram.

In the gamma detection system the dead time is calculated by dividing the total number of gamma events (also referred to as *triggers*) acquired by the total number of gamma events presented to the system. Triggers acquired are the number of events that produced an analogue signal accompanied by a master gate signal in the ADC, and are hence written to memory. Triggers presented include all events that are acquired in addition to all events that generated an analogue signal in the ADC with no master gate signal, due to the system being busy processing a previous event. As such, the total presented events should always be at least as great as the total number acquired, referred to as gammas presented and acquired respectively with the number of each such event being recorded in a scalar unit. The precise location of the scalar logic can be seen in figure 2.14.

The heavy ion detection system consists of either a double sided silicon strip detector (DSSSD) or an ion chamber (IC). Figure 2.15 shows the DSSSD electronics, although the IC was in fact used for both experiments in this thesis, the main difference being that the IC has only 4 preamp outputs, one for each anode, instead of 16. These preamplifiers feed each detector signal to an amplifier and discriminator module in parallel. A heavy ion trigger in generated by the logical OR from all the discriminator outputs which triggers an ADC and TDC for each detector channel. These then process the analogue signals and write them to a heavy ion memory buffer. The TDC's also receive a trigger from the gamma array's master gate allowing for ion events to be tagged as coincident if they occur within 4.5 μs of a gamma event.

Live time for heavy ion events is calculated in much the same way as for gamma events, by dividing the total number of acquired scalars by the total number of presented scalars, but referring to only those events that generate signals in the heavy ion side of the electrons instead. Deciding which live time to used when calculating a total yield for an experiment depends on weather the experimenter has used singles or coincidence ion events for analysis. Singles events only require the heavy ion detection dead time since they ignore any accompanying gamma events completely, coincidence events however require summing scalar triggers

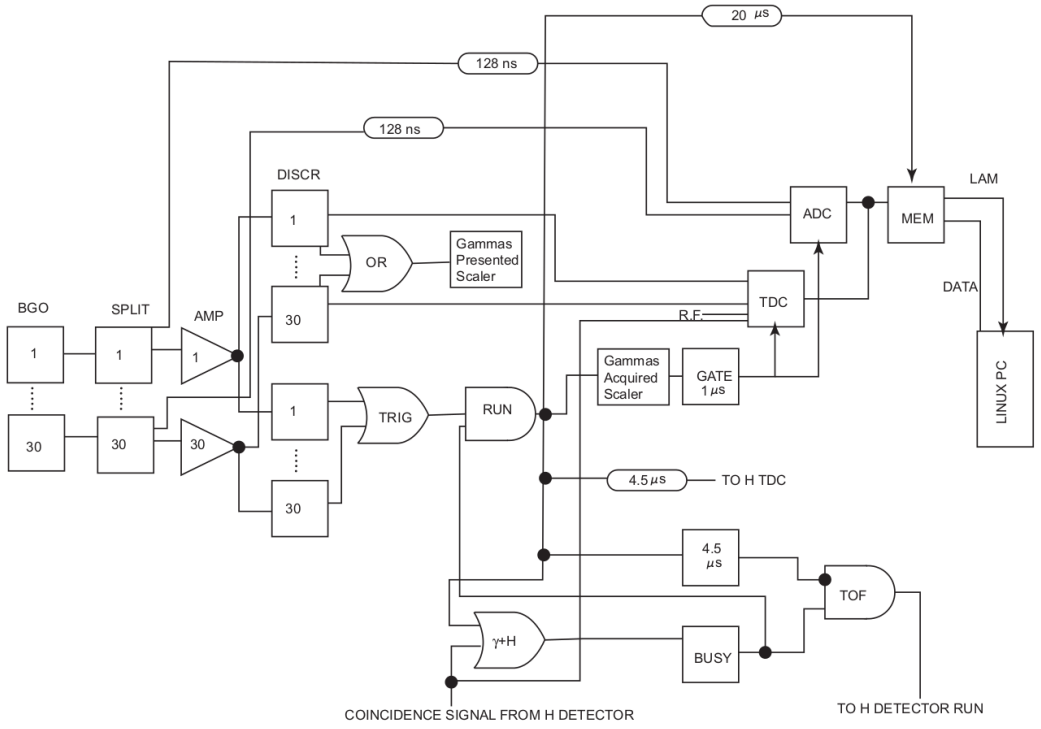

FIGURE 2.14: Block diagram detailing the gamma array electronics in the previous DAQ setup, taken from [32].

for both ion and gamma systems. As the BGO gamma array can trigger independently of the heavy ion system this does mean that some recoil events occur when the array is busy processing a previous event. This can be accounted for by including the array live time during analysis. As the gamma detection live time is typically greater than 90% not a significant number of coincidence events are lost due to this effect however.

The Timestamp Based System

The new DRAGON DAQ identifies coincidence events via their timestamp rather than hardware gating, such that the gamma and heavy ion system's trigger and read out independently of each other; events are only designated as being either single or coincident at a later analysis stage, by a *backend* computer. This required upgrading the frontend CAMAC system to a VERSAmodule Eurocard (VME) and transferring part of the trigger logic from NIM electronics to a field programmable gate array (FPGA). The gamma detection electronics, or *head end* as it is now referred, consists of the same 30 BGO detectors whose anode signals are split into analogue and logic channels, the latter of which is fed into a charge to digital converter (QDC). The former are sent to CFD's with each channel then fed to a TDC whilst the logical OR of all channels combined is sent to a general purpose VME module where an Altera Cyclone-I FPGA [37] is housed (referred to as the IO32), which does the majority of the trigger logic and timing analysis. The generated event trigger is sent to both the head and heavy ion TDC's allowing for the separator time of flight to be calculated. The heavy ion, or *tail side*, electronics now consists primarily of another IO32 module which receives the

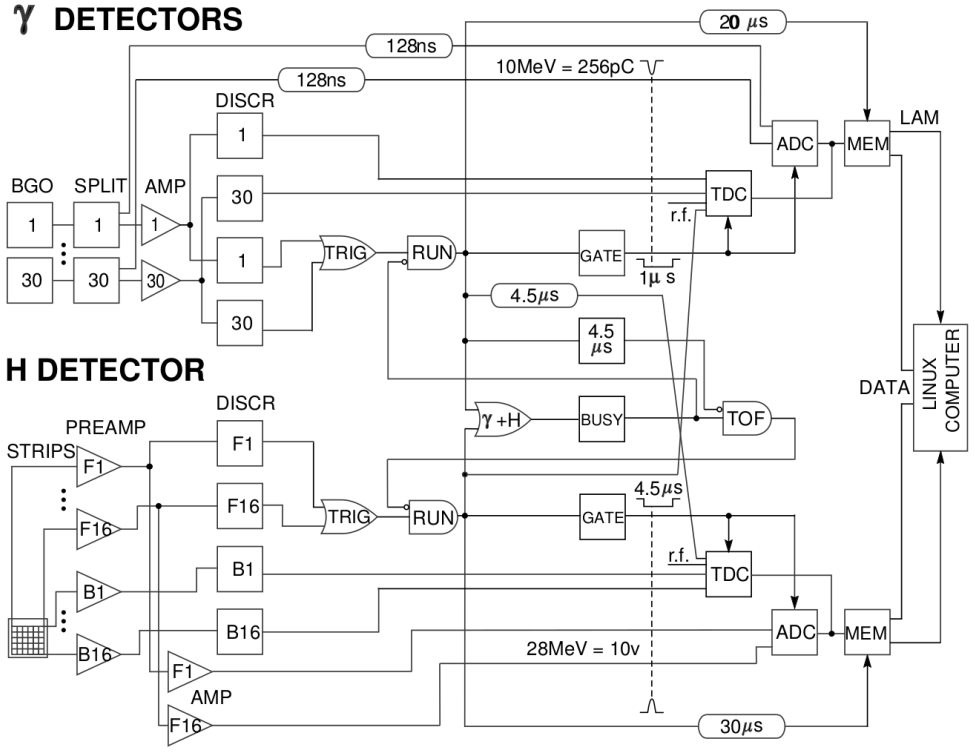

FIGURE 2.15: Block diagram of both heavy ion and gamma array electronics for the previous DAQ system, taken from [31].

logic signal from all the heavy ion detectors whose corresponding analogue signals are sent to an ADC channel by channel. See figure 2.16 for an overview of the system.

Backend processing of coincidence events requires an algorithm that matches head and tail events based on their timestamp for a given time period, since the *frontend* VME processor sends packets of data in 1 second intervals. This requires a buffer of both head and tail events, ordered chronologically by their trigger time, whereby the whole array is searched for a coincidence match with the first. Events are classed as such if another event is found with a timestamp difference of <10 μs over a four second buffer and they are then sent to a coincidence event processor, with only the earliest of the two subsequently removed from the buffer. All buffer events are eventually sent to a singles processor before being removed regardless of coincidence matching, figure 2.17 gives an overview of the process.

This system of having two independently running detector systems requires modifying the coincidence live time calculation as event tagging occurs at a much later stage, making the timestamping of every presented trigger problematic. An alternative involves analyzing the busy time, that being the time after an event that the DAQ does not process other incoming signals, for every recorded event. Busy times are calculated by the IO32 and stored in the data steam for every recorded event. To use this information properly we must consider the number of events lost (n_{lost}) in a Poisson process with non-paralyzable detectors[2]:

[2]DRAGON's detectors are assumed to be non-paralyzable such that events occurring during the dead period immediately after a previous event have no effect on the detector's behaviour.

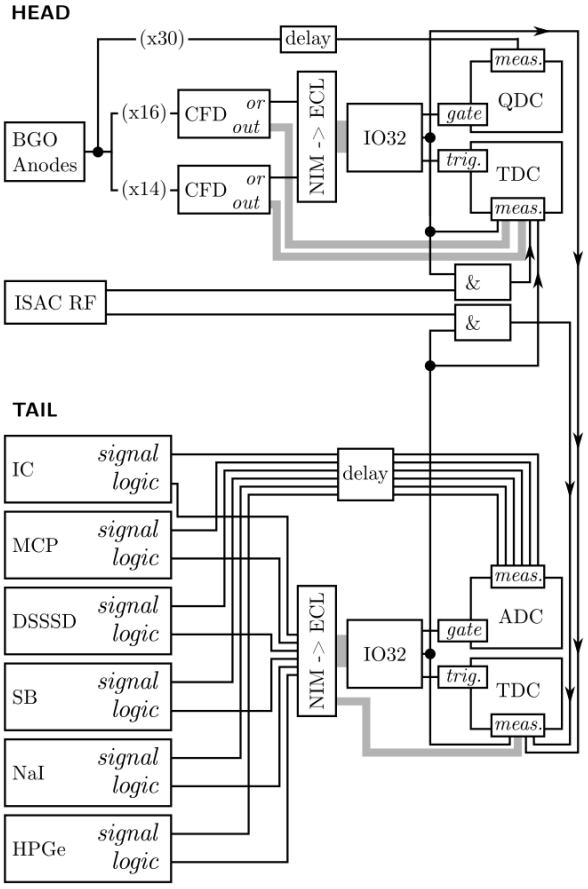

FIGURE 2.16: Block diagram of both heavy ion (TAIL) and gamma array (HEAD) electronics for the new DAQ system, taken from [38].

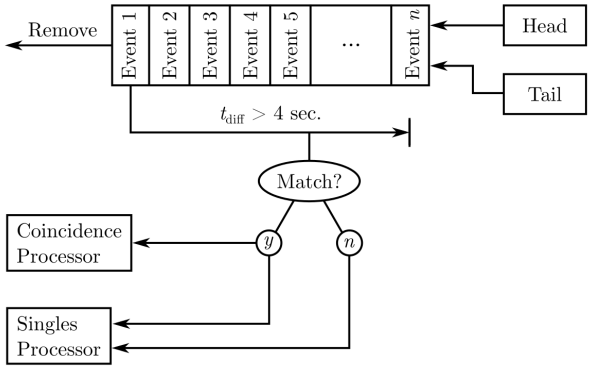

FIGURE 2.17: Flow diagram illustrating the coincidence matching algorithm in DRAGON's new DAQ. Taken from [38].

$$n_{lost} = \lambda \sum_{i=0}^{n} \tau_i = \lambda\tau \tag{2.4}$$

Here n is the total number of events recorded, λ is the rate of event production, τ_i is the busy time for the *ith* recorded event with τ being their sum over n. The total number of

generated events can also be defined as:

$$N = n + n_{lost} \tag{2.5}$$

Substituting equation 2.4 into 2.5 and using N/T in place of λ we can arrive at:

$$N = \frac{n}{1 - \tau/T} \tag{2.6}$$

Which infers that the system live time (LT) is in fact:

$$LT = 1 - \tau/T \tag{2.7}$$

Note that in this case the total system busy time is explicitly the time the system is busy processing either head OR tail events, where OR has inclusive logic. Despite the fact that this method assumes a constant beam intensity, its results have been observed to be consistent to within 2% of both the non-Poisson and scalar method, used for the old DAQ, with even better agreement in the absence of serious beam fluctuations [38].

2.2.8 γ Radiation Detection and Spectra

The interaction of photons, generated via astrophysical reactions, with the detectors at DRAGON (specifically the BGO array) is dominated by three processes:

Photoelectric Absorption In this scenario the γ ray photon is completely absorbed by an atom comprising the detector crystal, and as a result a photo-electron is liberated from one of the latter's most bound electron shells. The energy of the photo-electron is given by:

$$E_{e-} = E_\gamma - E_b \tag{2.8}$$

where E_γ is the γ energy and E_b is the binding energy of the photo-electron's previously occupied shell. The resulting shell vacancy is subsequently filled by either free electrons or a cascade of currently occupied states, generating characteristic X-rays.

Compton Scattering This process describes the act of a γ ray photon being deflected by an electron in the target atom. As all available angles of scattering are possible the energy lost by the photon can vary considerably, according to:

$$E'_\gamma = \frac{E_\gamma}{1 + \frac{E_\gamma}{m_e}(1 - \cos(\theta))} \tag{2.9}$$

where E'_γ is the post scattering energy of the photon, m_e is the electron rest mass (511 keV) and θ is the photons angle of scattering. In practice all scattering angles occur in the detector crystal and so a *Compton continuum* of energies is produced in the resulting spectra, as shown in figure 2.18.

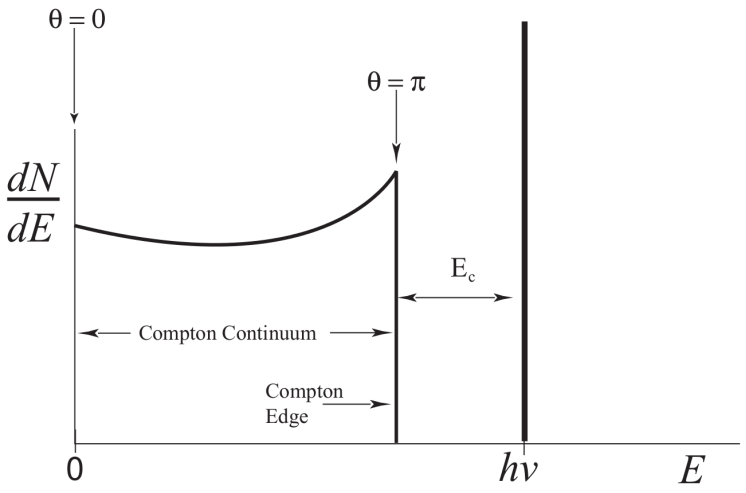

FIGURE 2.18: Example γ ray spectrum showing the effect of Compton scattering. As a range of scattering angles θ are possible a continuum of detection energies forms below the photopeak ($h\nu$). E_c is the energy between the photo peak and the scattering scenario that minimizes photon energy loss. Taken from [32].

Pair Production In this scenario the incident γ ray transforms into an electron positron pair, and so must have an energy at least greater than twice m_e. This process can only occur in the presence of the coulomb field generated by a nucleus. The electron produced loses its energy over the course of a few millimetres, and the positron annihilates, forming two secondary 511 keV γ rays. It is entirely possible that one or both of these subsequently escape the detector crystal undetected, resulting in a secondary *single* or *double escape peak* located 1 or 2 m_e (511 or 1022 keV) below the full energy peak[3], respectively. The energies and type of absorber atoms where each process becomes dominant is shown in figure 2.19.

2.3 Statistical Analysis of Experimental Data

Any measurement taken in the laboratory is never exact, there is always some intrinsic uncertainty in whatever is being observed which propagates as multiple measurements are combined. The treatment of such uncertainties, or errors as they are also referred as, requires a detailed mathematical framework which is outlined in this section.

2.3.1 Central Limit Theorem

Errors in observed quantities can arise from a multitude of different sources and can mostly be modelled as following a Gaussian (or normal) distribution. The reason for this is described in the central limit theorem (CLT), which states that:

If you take the sum X of N independent variables, x_i, where $i = 1, 2, 3, ..., N$, each taken from a distribution of mean μ_i and variance V_i or σ_i^2, the distribution for X:

a) has an expectation value:

[3]also termed the photopeak

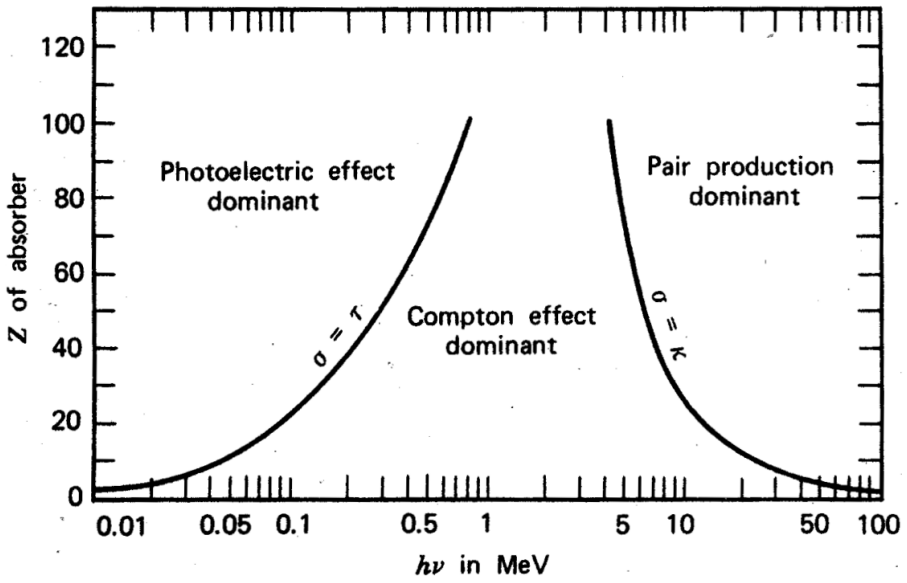

FIGURE 2.19: Illustration of the regions where each γ detection process is dominant. Taken from [35].

$$< X >= \sum \mu_i \tag{2.10}$$

b) has variance:

$$V(X) = \sum V_i = \sum \sigma_i^2 \tag{2.11}$$

c) becomes Gaussian as $N \to \infty$

This means that any observable that is the product of numerous independent variables can be modelled as having a Gaussian distribution regardless of the independent variable's distribution. In practice however distributions of variables can deviate from the normal in regions far away from the expectation value. These areas are typically referred to as *wings* or *tails* and can pose significant problems during experimental analysis.

An important consequence of CLT can be inferred by considering an observable that is measured several times, such that each independent variable now has the same value. Using equation 2.10 we can say:

$$\langle X \rangle = \sum \mu = N\mu \tag{2.12}$$

And by defining the average of our measurements as $\overline{x} = X/N$ we get:

$$\langle \overline{x} \rangle = \mu \tag{2.13}$$

and using the definition of variance:

$$V(X) = \langle (X - \langle X \rangle)^2 \rangle \tag{2.14a}$$

$$\Rightarrow V(\overline{x}) = \frac{1}{N^2} \langle (X - \langle X \rangle)^2 \rangle \tag{2.14b}$$

$$\Rightarrow V(\overline{x}) = \frac{1}{N^2} V(X) = \frac{1}{N^2} \sum \sigma_i^2 \tag{2.14c}$$

$$\Rightarrow \sigma_{\overline{x}} = \frac{\sigma}{\sqrt{N}} \tag{2.14d}$$

Equation 2.14d gives us the standard error in the mean ($\sigma_{\overline{x}}$), which is dependant on the standard deviation of the observable we are measuring (σ) as well as the number of measurements taken (N). This tells us that if we take N measurements, their average ($\overline{x}$) will have a standard deviation that depends on $1/\sqrt{N}$, thus taking repeat measurements of an observable and averaging will reduce uncertainty in the final result. This result is important as reducing uncertainty in observed parameters is a cornerstone of experimental science. Ultimately however, this effect becomes impractical as in order to halve an error you need to take four times as many measurements or run your experiment for four times as long.

2.3.2 Error Propagation

Credible scientific results require analysis of single or multiple measurements each of which contains an error, thus it is inevitable that the final result will also have an uncertainty associated with it. To see how errors propagate from initial observation when combined consider the function $f(x)$ expanded as a Taylor series about x_0:

$$f(x) \approx f(x_0) + (x - x_0) \left(\frac{df}{dx} \right)_{x=x_0} \tag{2.15}$$

By substituting this into equation 2.14a it can be seen that:

$$V(f) \approx \left(\frac{df}{dx} \right)^2 V(x) \tag{2.16a}$$

$$\Rightarrow \sigma_f \approx |\frac{df}{dx}| \sigma_x \tag{2.16b}$$

Note that this approximation is valid in the region around x_0, which requires that the differential does not change significantly within a couple of σ. If we now consider a function of two or more variables, $f(x, y)$, and again use equation 2.14a we can see that:

$$V(f) = \left(\frac{df}{dx} \right)^2 V(x) + \left(\frac{df}{dy} \right)^2 V(y) + 2 \left(\frac{df}{dx} \right) \left(\frac{df}{dy} \right) \mathrm{cov}(x, y) \tag{2.17}$$

If the two observed variables are independent then their covariance will be zero and the last term in equation 2.17 vanishes so that the error can be expressed as:

$$\sigma_f^2 = \left(\frac{df}{dx}\right)^2 \sigma_x^2 + \left(\frac{df}{dy}\right)^2 \sigma_y^2 \tag{2.18}$$

This equation tells us that the relative error on results, that are a combination of multiple observables, is smaller than the sum of the relative error on those observables. This can be understood if you consider the fact that a measurement of x yielding a value higher than μ (the expectation of the populations mean) can be compensated for by a comparatively lower measurement of y. Equation 2.18 can be extended to functions of three or more variables by consecutively adding them in quadrature.

2.3.3 Systematic Errors

Unlike random errors systematic effects on data are not independent as they shift every observation made equally, complicating the situation as repeat readings will fail to yield the magnitude or even existence of such an error. An example of such an uncertainty is the activity of a source used for calibrating a detector, no matter how many decay events discerned in the spectrum, if the sources activity is not properly calibrated the calculated efficiency will be subject to a systematic effect. Since this can occur without the experimenter noticing, these kind of uncertainties can be particularly dangerous and should be carefully considered at all stages of experimentation and analysis.

As systematic effects are independent from random errors, CLT allows us to add them in quadrature to give the total uncertainty in our final result, however it is common practice to quote the random and systematic uncertainties of a measurement separately. This is because often the randomness of data can be quantified more reliably than the systematic part, which may also be subject to change in the future as you better characterize your apparatus and/or simulations.

2.3.4 Bayesian Statistics

Usually when observing events due to a specific reaction in an experiment a spectrum is formed with enough counts to distinguish the peak of interest from background events. Ideally there will be enough counts in the peak for it to take the form of a Gaussian in which case the CLT can be applied. However when very few events are observed the situation becomes more complicated, requiring different techniques to be utilized in order to assign a region of uncertainty, or a confidence level, to a measurement.

The goal in most experiments is to obtain a measurement of a certain parameter (μ) in order to gain better insight on its true value (μ_t). This parameter is measured by making observations of an experimental variable (x) which depends on μ, thus we can construct a *probability density function* (pdf) that tells us the likelihood of measuring a certain value of x (x_0) given the unknown parameter μ, depicted as $P(x_0 \mid \mu)$. We can then calculate the pdf for μ_t given the result x_0 by using Bayes's theorem:

$$P(\mu_t \mid x_0) = P(x_0 \mid \mu_t)P(\mu_t)/P(x_0) \tag{2.19}$$

Here $P(\mu_t)$ is called the prior pdf, $P(\mu_t \mid x_0)$ is referred to as the posterior pdf and $P(x_0)$ is just a normalization constant. The prior pdf can include personal prejudice, and results from previous experiments, making it subjective in which case if an experiment measures a value of μ significantly different to expectations the prior will take a very low value, casting doubt over the results validity. Various methods are available to make the prior pdf objective rather than subjective [39][40].

Bayesian intervals can be deduced using:

$$\int_{\mu_1}^{\mu_2} P(\mu_t \mid x_0)\, \mathrm{d}\mu_t = \alpha \tag{2.20}$$

This gives us a degree of belief (α) that the true value of μ (μ_t) lies within the region $[\mu_1, \mu_2]$, given our measurement x_0. The limits of equation 2.20 can be altered freely depending on whether an upper, lower or central confidence level is required.

2.3.5 Classical Statistics

Classical confidence intervals do not involve the use of a prior pdf [41] but instead involve inferences about $P(x \mid \mu)$ rather than the posterior. Due to the lack of a subjective prior it can be argued that classical intervals are the best way to present scientific results in an objective way [42]. Classically such confidence intervals are defined as:

$$P(\mu \in [\mu_1, \mu_2]) = \alpha \tag{2.21}$$

This equation states that the confidence interval $[\mu_1, \mu_2]$ will enclose μ_t a fraction α of the time for any given set of identical experiments, a very different notion to the Bayesian interval which gives a degree of belief that μ_t lies within the interval $[\mu_1, \mu_2]$. To construct confidence intervals we require the method of confidence belts [40], which involves calculating, for each value of μ, the interval:

$$P(x \in [x_1, x_2] \mid \mu) = \alpha \tag{2.22}$$

Which is $P(x \mid \mu)$, for which x is a member of the region $[x_1, x_2]$, with a confidence level α. When plotted on a graph of x vs μ these intervals appear as horizontal lines, as shown in figure(2.20), with the resulting structure referred to as a confidence belt. The confidence interval α is the set containing all the points where the vertical line drawn up though x_0 intercepts the confidence belt $[\mu_1, \mu_2]$.

In classical intervals the acceptance region $[x_1, x_2]$ cannot be influenced by the measured data x_0, as letting our measurement dictate what confidence regions we use distorts the acceptance region to the point where equation 2.22 is no longer valid. This can cause the acceptance region to cover less than α of $P(x \mid \mu)$, referred to as under coverage, and is a flaw in any confidence band.

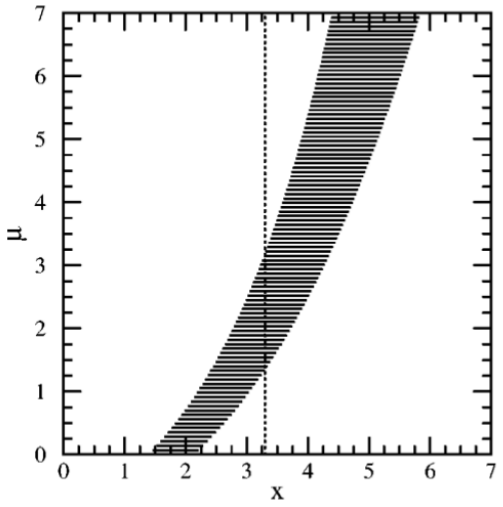

FIGURE 2.20: Graph illustrating the horizontal acceptance regions from equation 2.22. Confidence intervals for x_0 can be extracted by drawing vertical lines through the measured quantity, with the points of intercept giving the interval $[\mu_1, \mu_2]$. The inclusion of background events as a nuisance parameter creates the offset in x relative to μ. Taken from [42].

2.3.6 Profile Likelihood Technique

One of the drawbacks to the confidence belt described in figure 2.20 (also see [42]) is the non inclusion of multiple *nuisance parameters*, which are not the parameters of interest per se, but must be included in the analysis of any data obtained (such as detector efficiency or background contamination). Another approach to constructing confidence intervals involves using the profile likelihood technique which allows the characterization of collected data purely in terms of the parameter of interest, usually the number of events due to the reaction that was observed, whilst taking into account all of the nuisance parameters [43].

The profile likelihood technique uses the data's likelihood function in the form:

$$L(\pi, \theta|X) = \prod_{i=1}^{n} P(X_i|\pi, \theta) \tag{2.23}$$

Here π is the parameter of interest, θ represents the nuisance parameters and X is our data set. The likelihood is the product of each observables (X_i) probability (P) with the profile likelihood being the ratio of two hypothesis H_0 (where $\pi = \pi_0$) and H_a ($\pi \neq \pi_0$), which tells us how likely H_0 is relative to all other possible alternatives:

$$\lambda(\pi_0|X) = \frac{\sup\{L(\pi_0, \theta|X); \theta\}}{\sup\{L(\pi, \theta|X); \pi, \theta\}} \tag{2.24}$$

Here, the *supremum* (sup) is the least upper bound of a specified set of numbers. Equation 2.24 allows us to produce a likelihood function that depends on only our parameter of interest and the observed data. We are essentially varying π and θ for a multitude of possible scenarios and calculating how likely each one is based on our observed data (X); the most likely becomes the denominator of equation 2.24 ($\sup\{L(\pi, \theta|X); \pi, \theta\}$). π is then held constant, becoming π_0, and likelihoods calculated for all possible values of θ. The most likely of these is divided

by $\sup\{L(\pi, \theta|X); \pi, \theta\}$ and becomes the profile likelihood value for this π_0. This process is then repeated for all values of π_0 such that a continuous function is created, meaning every π_0 has a corresponding profile likelihood value. The minimum of the function -2 $\log(\lambda)$ (which corresponds to the most likely scenario) converges to a χ^2 distribution [44], which can be used to extract limits on π_0 as when the -2 $\log(\lambda)$ curve increases by an α percentile of the χ^2 distribution, with one degree of freedom, the corresponding values taken by π_0 give a 100(1-α)% confidence interval [43].

Chapter 3

Measuring the ^{18}F(p,γ)^{19}Ne Reaction Rate

The titled reaction is one of the two focal points of this thesis. Its importance is due to its relevance in the observation of novae. The following chapter describes the reasons for looking at such a reaction, specifically the 665 keV resonance, and details the experimental procedure necessary to gain credible results on parameters of interest. It should be noted that the analysis presented in here was previously published, by the author, in the journal *Physics Review Letters* [45].

3.1 Background

3.1.1 Novae

Nova outbursts are one of the most explosive and commonly observed events in the universe, only supernovae and gamma-ray bursts outshine them. Given the rate at which novae occur in our galaxy ($\approx$ 30 events/yr), their mean ejected mass ($\approx 2 \times 10^{-5} M_{\odot}$) and the galactic age ($\approx 10^9$ yr), it is highly unlikely that they contribute in a significant way to the current galactic metalicity (the proportion of a bodies mass that is not H or He). They may however be responsible for a few lower mass (A<40) isotopes which appear to be largely over abundant, such as ^{13}C, ^{15}N and ^{17}O [46, 47]. Their observation has also proved to be an important resource for testing stellar models [48].

Classical Novae occur as a result of mass accretion[1] in a binary system; material in an envelope of a main sequence star that has filled its Roche lobe[2] is captured by an accompanying white dwarf star (WD), compressing it to such an extent that it becomes electron degenerate. As matter in this phase does not expand when heated, the heat released from the eventual triggering of H burning in the shell surrounding the WD does not cause it to expand and cool, and so a thermonuclear runaway reaction (TNR) results. The thermal radiation is not sufficient to disperse all the energy being produced though and so convection occurs, transporting β unstable nuclei to outer, cooler regions of the burning shell. Their subsequent

[1] A star's growth due to gravitationally attracted matter from a companion star
[2] The spatial region surrounding a star that is gravitationally bound to it

decay releases enough energy to lift the shell's material out of degeneracy causing expansion and eventual ejection.

The TNR initially occurs when enough H-rich material is accreted onto the WD ($M \approx 10^{-6} \rightarrow 10^{-4} M_{\odot}$) for the innermost layers surrounding the star to become compressed to the point where it becomes electron degenerate. Burning takes place initially via the pp chain, then later via CNO cycles (see sections 1.1.8 and 1.1.10), with the heating from compression and nuclear synthesis ultimately leading to an outburst of material. The CNO and hot CNO cycles are responsible for powering the TNR, rather than the pp chain which is more influential during the accretion phase. As the rate of energy generation from the CNO cycles is temperature independent above 10^8 K, production is instead determined by the abundance of C, N, O, Ne and Mg in the envelope. This requires a significant enrichment of CNO nuclei to occur in order for the outburst to occur. Convection, which proceeds throughout the accreted envelope, provides this by transporting the necessary nuclei to the burning layer. Once T> 10^8 K is achieved most of the CNO nuclei proton capture, becoming β^+ unstable, and a large portion are carried to the surface where they decay, releasing heat and flattening the temperature gradient of the envelope which ends the convection phase. As mentioned earlier, this same release of energy also contributes to the final ejection of accreted material. The timescale of burning and subsequent mass ejection varies from tens to hundreds of seconds, depending on the composition and mass of the nova model [49].

WD's in these binary systems fall into two categories: carbon-oxygen (CO) and oxygen-neon (ONe). The former are remnants of low mass stars ($< 10\, M_{\odot}$) which have undergone only H and He burning. The latter form from higher mass progenitors which allowed for carbon burning, resulting in an ONe core. Despite their name these ONe WD's are surrounded by a thick CO buffer region so that their spectra don't show particularly strong Ne lines. As there is no source of neutrons in these outburst most of the reactions are either (p,γ) or (p,α), and such reactions in the mass and temperature range relevant to novae are mostly within the means of current experimental facilities. This makes them special in that they are the only explosive astrophysical site that can be modelled primarily with experimentally observed data [6]. The framework for the given description of novae was taken from [50].

3.1.2 Motivation

The observation of γ-rays and X-rays from radioisotope decay by satellite missions is a powerful tool for providing information on the astrophysical processes occurring during the lives and deaths of stars. In 2002, ESA launched the INTEGRAL satellite with the goal of mapping out γ-ray emission across the whole sky; NASA also launched the SWIFT γ-ray burst telescope in 2004 and both are capable of making γ-ray spectroscopic measurements of stellar objects. Observations from these missions can provide data on the abundance of particular isotopes synthesized in such environments and thus put constraints on the astrophysical models. For example, the recent INTEGRAL observation of hard X-rays from Supernova 1987A [51] allowed the amount of ^{44}Ti produced during the core collapse supernova explosion to be derived and compared to that predicted by different models.

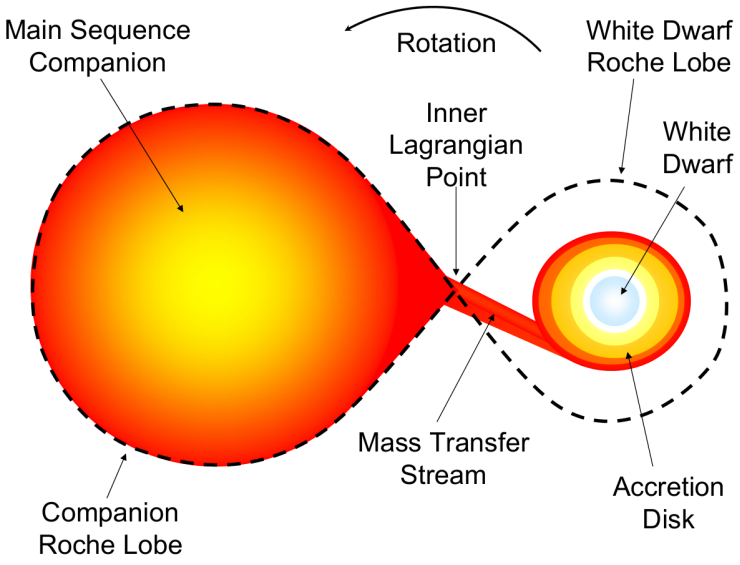

FIGURE 3.1: Drawing illustrating the major components of novae, taken from [26].

In the case of nova explosions (see section 3.1.1) one radioisotope of interest is ^{18}F [47], which is thought to be the major source of line emission γ-rays, at 511 keV, after the nova outburst; such gammas are produced as a result of positron annihilation following its β^+ decay. What makes this nucleus special is that the relatively long half life of ^{18}F ($t_{1/2}$=110 mins) means that a significant number of positrons are emitted shortly after the expanding nova envelope becomes transparent to γ-rays. If the reaction rates for the production and destruction of ^{18}F are sufficiently well known then observations of this γ-ray emission can provide constraints on physical conditions inside novae, leading to improvements in astrophysical models [48]. This could, for instance, help address the discrepancy between the observed ejected mass and that predicted by current models [52]. Observation of 511 keV γ-ray line emission, however, requires the difficult task of a-posteriori searches of data from wide field instruments as the peak optical brightness occurs days after the positron annihilation flash [52, 53]. Of the two types of white dwarf stars responsible for novae, carbon-oxygen (CO) and oxygen-neon (ONe), the latter result in hotter novae that eject more ^{18}F, and are thus of greater interest for satellite observations.

Although there is still some uncertainty in the reaction's production rate at nova temperatures, between 0.1 and 0.4 GK [54, 55] (and references therein), the main uncertainty in the final abundance of ^{18}F depends on its destruction rate via the (p,γ) and (p,α) pathways. The ^{18}F(p,α)^{15}O reaction is estimated to be a few thousand times faster [56] and thus it has been the focus of many studies (see later). By contrast, little effort has gone into probing the properties of the ^{18}F(p,γ)^{19}Ne reaction as a result of the much lower estimated cross section, and limited available beam intensity. However, a sensitivity study by Iliadis *et al.* [57] indicates that, for ONe novae, a factor of 10 increase or decrease in the (p,γ) rate changes the abundance of ^{18}F by a factor of 2.5 or 0.9 respectively, significantly affecting the potential number of novae detectable via satellite missions. Although counter intuitive, since the (p,γ) reaction destroys ^{18}F, the abundance change can be understood in terms of the reaction

pathway taken in order for ^{18}F to be recycled (see figure (3.2)). When ^{18}F is destroyed via the (p,γ) channel it has to pass through ^{19}Ne which has a relatively short half life of 17 sec. The pathway initiated via (p,α) however must traverse the isotope ^{15}O which has a longer half life of 122 s, and so not all the ^{15}O ends up back as ^{18}F. Thus the (p,γ) pathway is much more efficient at recycling ^{18}F.

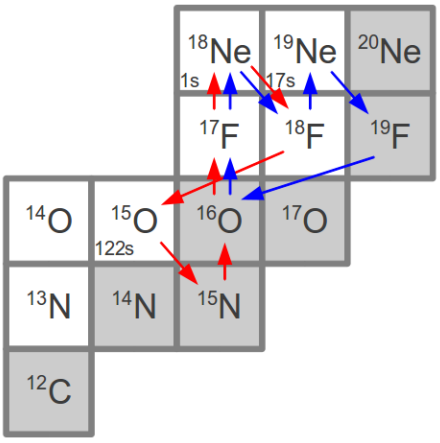

FIGURE 3.2: Destruction of ^{18}F via (p,α) means that the reaction path (red) will have to travel through ^{15}O, which has a relatively long decay time, to get back to ^{18}F. The (p,γ) reaction leads to a pathway in which ^{18}F can be recycled much more efficiently (blue).

3.1.3 Past and Present Studies of the ^{19}Ne Level Structure

The ^{18}F(p,γ)^{19}Ne reaction proceeds through proton capture into states in ^{19}Ne in an excitation range which is currently still not fully described. A host of different approaches have been used in the past to probe further into ^{19}Ne's level structure, with the most relevant studies outlined in this section.

Initial Studies with a ^{18}F Beam

Direct measurements of both the (p,γ) and (p,α) channel cross sections were not possible until the development of ^{18}F beams of sufficient intensity, after which a flurry of activity followed: Rehm *et al.* [58–60], Coszach *et al.* [61] and Graulich *et al.* [62, 63]. The first of such observations [58], focusing on the (p,α) channel, utilized a tandem accelerator to send ^{18}F ions onto a 118 μg/cm^2 polypropylene target in the laboratory energy range 11.7→15.1 MeV which corresponds to an excitation region in ^{19}Ne where a broad state was suspected to reside [64]. ^{15}O recoils were separated from reaction contaminants via a gas filled magnet, which distinguishes nuclei based on their magnetic rigidity, and two parallel grid avalanche counters (PGACs) for time of flight measurements.

Genuine recoil events were observed for three beam energies at θ_{cm}=110° corresponding to a resonance strength ($\omega\gamma$) of 3.7±0.9 keV at E$_{cm}$=660 keV. Analysis showed that the most likely spin assignment was 3/2$^+$ based on the assumption of a single resonance of width 40 keV, as previously deduced from [64]. The same method was used again the following year with a thinner target, a Si strip detector for detection of recoil events, and coincidence gating

on α particles for better background suppression [59]. Analysis of that data using the ratio of proton to alpha widths from [65] yielded a similar result; a single resonance with $J^{\pi}=3/2^{+}$ at E_{cm}=652 keV with a total width (Γ) of 13.6±4.6 keV and $\omega\gamma$=2.1±0.7 keV.

This work was done in parallel, but separately, with Coszach *et al.* who used a 14 MeV ^{18}F beam incident on a thick 200 μg/cm^2 polyethylene target to create a single step centre of mass energy range of 550→740 keV. The work was carried out using the Louvain-la-Neuve radioactive beam facility using a large annular multistrip silicon detector for PID at a variety of angles. The resulting spectra from (p,α) and (p,p) events exhibited a clear resonant structure at E_{cm}=638±15 keV with Γ=37±5 keV; the proton scattering data favoured a $3/2^{+}$ spin assignment. Normalization of the α spectrum relative to the scattering data yielded $\omega\gamma$=5.6±0.6 keV which when considered alongside the ^{19}F(^{3}He,tp) and ^{19}F(^{3}He,tα) studies at Notre Dame [66] (later published by Utku *et al.* [56]) gave further credence to the J^{π} assignment.

Graulich *et al.*[62] subsequently repeated this experiment at a lower energy with the resulting α spectrum showing a clear resonance at E_{cm}=324±7 keV of strength $\omega\gamma$=3.5±1.6 eV.

The Coszach *et al.* study disagreed with Rehm *et al.* work over both the $\omega\gamma$ and Γ of the broad resonance at E_{cm} ≈653 keV although, as pointed out in Graulich *et al.*, the results from the Louvain-la-Neuve facility gave much better agreement with the ^{19}F(^{3}He,tp) and ^{19}F(^{3}He,tα) work at Notre Dame, details of which are given below.

Initial Indirect Experiments

As already stated, the direct ^{18}F beam experiments were supplemented by indirect studies undertaken by Utku *et al.* [56] and Butt *et al.* [67], the former of which used a ^{3}He beam, at Princeton, to look at the ^{19}F(^{3}He,tα)^{15}O and ^{19}F(^{3}He,tp)^{18}F reaction with a 50 μg/cm^2 CaF_2 target. Tritons emitted from the reaction were detected with the Princeton QDDD spectrometer; coincident protons and alphas, from the subsequent decay of the ^{19}Ne nuclei populated in the (^{3}He,t) reaction, were observed via surface barrier silicon detectors located at three separate angles. The resulting α and proton spectra were used to determine the relative strength of each decay branch (Γ_{α}/Γ and Γ_{p}/Γ). Another experiment was also carried out, at both the University of Notre Dame and Princeton, with the same beam and target but observing just tritons from the ^{19}F(^{3}He,t)^{19}Ne reaction; six previously unknown levels in the region 6.4$\leqslant E_x \leqslant$7.4 MeV of ^{19}Ne were discerned. In order to identify possible isospin mirror states in ^{19}F two sets of mirror reaction pairs were also observed in the form of ^{16}O(^{6}Li,t)^{19}Ne vs ^{16}O(^{6}Li,^{3}He)^{19}F and ^{20}Ne(d,t)^{19}Ne vs ^{20}Ne(d,^{3}He)^{19}F. Analysis of these data sets suggested four new such mirror pairings.

The ^{15}N(α,γ)^{19}Ne reaction was also used to probe the mirror of the E_{cm} ≈653 keV state in ^{19}Ne in an experiment by Butt *et al.*; analysis confirmed the state's width as measured by Coszach *et al.*.

Previous ^{18}F(p,γ)^{19}Ne Study

The competing (p,γ) channel was first observed experimentally by Rehm *et al.* in 1997 [60] using a solid 80-100 μg/cm^2 CH_2 target. A two stage method was used for beam generation: ^{18}F material was first synthesized via the ^{18}O(p,n)^{18}F reaction using the cyclotron at the University of Wisconsin and subsequently flown to the Argonne National Laboratory, a journey made feasible by the nuclides relatively long half life. After arrival it was installed onto the negative ion source of the ATLAS tandem injector and delivered to the experiment with the same tandem accelerator as the (p,α) studies authored by Rehm *et al.*, described above.

A fragment mass analyzer (FMA), consisting of one magnetic and two electric dipoles, was used to separate beam from recoil ions by dispersing their respective spatial trajectories, in much the same way as DRAGON (see section 2.2.4). The FMA was tuned such that any recoils produced in a given charge state were guided to a focal plane where a PGAC and ion chamber provided for PID analysis. A calibration run with ^{18}O(p,γ)^{19}F in inverse kinematics was performed with the FMA, set to transmit ^{19}F products in the 7^+ charge state. The ion chamber was used to produce a ΔE-E plot, with ΔE being energy loss in the first portion of the chamber and E being total energy loss, which showed loci corresponding to the presence of both ^{19}F recoils and ^{18}O beam ions. Separation of the two nuclei regions was good enough for them to be distinguished, allowing for a cross section to be extracted for a range of energies, all of which showed good agreement with previous data from [68].

For the ^{18}F run a beam energy was selected to place the E_{cm}=652 keV resonance, as measured from the (p,α) studies described earlier, near the centre of the target, accounting for energy loss. Total integrated beam current was calculated by collecting elastically scattered ^{18}F beam ions on a circular aperture and subsequently measuring its β^+ decay activity. Variations in beam intensity were monitored from β^+ decay on the collimator after the first electric dipole, where ^{18}F beam ions in non selected charge states were stopped. An average beam intensity of 3×10^5 ^{18}F particles/sec was determined in this way with an ^{18}O contamination ratio (^{18}O/ ^{18}F) of 2500. Five different samples of ^{18}F were used in separate runs with the separator tuned for 7^+ ^{19}Ne recoils.

PID data was analyzed in the form of a ΔE-E plot with a region where ^{19}Ne recoils were expected chosen using data from the ^{18}O(p,γ)^{19}F calibration run in tandem with simulations of the ion chamber. In total three events resided inside this recoil cut region however their proximity to the ^{19}F peak region, formed due to ^{18}O beam contamination proton capturing in the target, warranted further investigation. This was done by moddeling the expected ^{19}Ne peak in the focal plane detector as a Gaussian distribution based on the calibration data. This was subsequently used to calculate that the probability of detecting three ^{19}Ne events with a ΔE_1 (energy loss in the first portion of the focal plane detector) as small or smaller than those observed to be <0.003. As such, the authors conceded that all three events were likely due to ^{19}F and so calculated an upper limit on the cross section, on the basis of there being just one ^{19}Ne event in the set recoil region. This yielded resonance parameters of $\omega\gamma \leqslant$740 meV and $\Gamma_\gamma \leqslant$3 eV.

Later Work

Rate estimates at novae temperature were made using the available information by Coc *et al.* in 2000 [69] who highlighted the need for more theoretical and experimental studies to reduce the large uncertainties in the ^{18}F+p rate. This was provided in the form of Graulich *et al.* [63], de Sereville *et al.* [70–73], Kozub *et al.* [74, 75] and Bardayan *et al.* [24, 76–78]

The second Graulich study [63] repeated the Cozach experiment, again focusing on the broader higher energy resonance, finding: E_r=657.5±0.7±1.7, Γ=34.2±2.2 keV, Γ_p/Γ=0.47±0.02 and $\omega\gamma$=4.7±0.2 keV.

An elastic scattering and (p,α) experiment by Bardayan *et al.* [24, 76, 77] using a thin 35 μg/cm^3 polypropylene target helped resolve some of the discrepancies from previous work. By detecting protons and α particles on a silicon detector array in coincidence with recoil ^{18}F ions values of E_r=664.7±1.6 keV, Γ=39.0±1.6 keV and Γ_p/Γ=0.39±0.02 were obtained, strongly favouring the Graulich *et al.* and Utku *et al.* results over the Rehm *et al.* work. Bardayan *et al.* utilized the same method again [78] to observe the lower energy resonance, as previously seen by Graulich *et al.* [62]. A fit to the resulting cross section data yielded $J^\pi=3/2^+$ and Γ_p=2.22±0.69 eV. Chae *et al.* [79] later used the same beam facility and experimental procedure to observe the energy range E_{cm}=663→877 keV. Lack of beam purity hindered precise measurement of the cross section at some energies however the 665 keV resonance was found to have positive interference with two higher energy $3/2^+$ states. The implications of this result at novae temperatures was minimal however [73].

Kozub *et al.* [74] conducted an indirect study via the (d,p) reaction on ^{18}F. Their results suggested that the 8 keV resonance was the dominant contributor to the (p,α) rate from the two states near the proton threshold.

In 2007 de Sereville *et al.* [72] also conducted further indirect studies in the form of a ^{18}F(d,p) reaction measurement with a ^{18}F beam incident on a CD_2 target, although at a much higher beam energy than Kozub *et al.*. Analysis showed two expected low lying $3/2^+$ resonances at 8 and 38 keV and highlighted their potential influence on the (p,α) rate, which remained uncertain due to the unknown interference effect with the 665 keV resonance.

de Sereville *et al.* [73] also conducted a (p,α) experiment, aiming to characterize interference effects at novae temperatures, with ^{18}F beam using a polyethylene target and silicon strip detectors. The study resulted in no definite conclusions however, other than highlighting the need for more direct measurements at lower energies.

In 2009 Dalouzy *et al.* [80] used inelastic scattering to observe a broad J=1/2 resonance at E_{cm}=1.45 MeV, significantly enhancing the (p,α) destruction rate on ^{18}F.

Nesaraja *et al.* conducted a review of ^{19}Ne levels relevant to novae nucleosynthesis in 2007 for the purposes of reaction rate calculations. Unknown parameters were estimated, providing the currently accepted value for the 665 keV resonances Γ_γ of 1 eV. Fig 3.3 shows the level diagram from this paper which highlights analogue assignments with ^{19}F.

More recent work on identifying and categorizing levels in ^{19}Ne include two studies looking at both the (p,α) and (p,p) reaction channels on ^{18}F [81, 82]. The first study identifies two new states and the second put constraints on seven resonances of astrophysical interest whilst confirming the presence of the broad state seen by Dalouzy *et al.*.

In 2011 A. S. Adekola *et al.* [83, 84] used proton and neutron transfer reactions to populate states in both ^{19}Ne and ^{19}F. The states observed were consistent with those previously known and the authors asserted that their data showed that the two lower lying resonances (8 and 38 keV) played only minor roles in the ^{18}F(p,α) rate at novae temperatures.

The same year Beer *et al.* [85] conducted the lowest direct measurement of the ^{18}F(p,α) cross section to date, which was done using the same beam facilities as the main experiment discussed in this chapter. Results suggested that a sub threshold state may in fact have a strong contribution to this reaction rate.

A recent study by Laird *et al.* [86] involved using the ^{19}F(^{3}He,t)^{19}Ne reaction to observe states near the proton threshold in ^{19}Ne. In contrast to previous work three levels were observed in this region, all with different angular distributions, none of which were $3/2^{+}$ inferring that possible interference effects with the 665 keV resonance do not dominate the (p,α) rate.

3.1.4 Current Knowledge of the ^{18}F(p,γ)^{19}Ne Rate

Not all expected states have been observed in ^{19}Ne but it was previously thought that the E_{cm}=330 keV (E_x=6.741 MeV) resonance was the main contributor to the reaction rate in novae, together with the 665 keV (E_x=7.076 MeV) resonance at the higher temperatures reached in ONe nova [56, 69, 89]. There is also a non-resonant direct capture contribution that becomes influential at lower novae temperatures, considered in [56, 60, 89]. The Laird *et al.* work does suggests new energies and spin assignments for states, which may have an impact on the interference from the 665 keV resonance at lower energies relevant to ONe novae.

Although the α and proton partial widths (Γ_α and Γ_p) are well known for the 665 keV resonance, as previously discussed, the radiative width Γ_γ remains unmeasured and the lack of an analogue state assignment [90] means no reliable estimate can be made. The experimental upper limit set by Rehm *et al.* does not constrain the reaction rate contribution of this state at nova temperatures by a significant margin. An arbitrary value of 1 eV [88] is therefore currently assumed in the literature, taken from surrounding states in ^{19}F.

Similarly, the Γ_γ of the 330 keV resonance has not been experimentally determined and a value of 5.0±2.6 eV is used based on an assumed analogue assignment determined from the study by Utku *et al.* [56]. The quoted Γ_α (effectively the total width) of 5.2±3.7 keV is also based on this analogue assignment. By contrast, the Γ_p has been determined experimentally to be 2.22±0.69 eV, from the direct measurement mentioned earlier [78]. A Γ_p of 7.3±0.6 eV was extracted from proton transfer data [83] but here the population of the 330 keV resonance could have been contaminated by nearby states. Consequently key parameters of both these resonances are experimentally unconstrained and thus the ^{18}F(p,γ)^{19}Ne reaction rate, and its impact on ^{18}F abundance, must be regarded as very uncertain. This was the scientific drive for us to undertake a new attempt to extend direct measurements of the ^{18}F(p,γ)^{19}Ne reaction rate to the relevant energy region. This was carried out as explained in the next section, using the DRAGON facility at the TRIUMF laboratory.

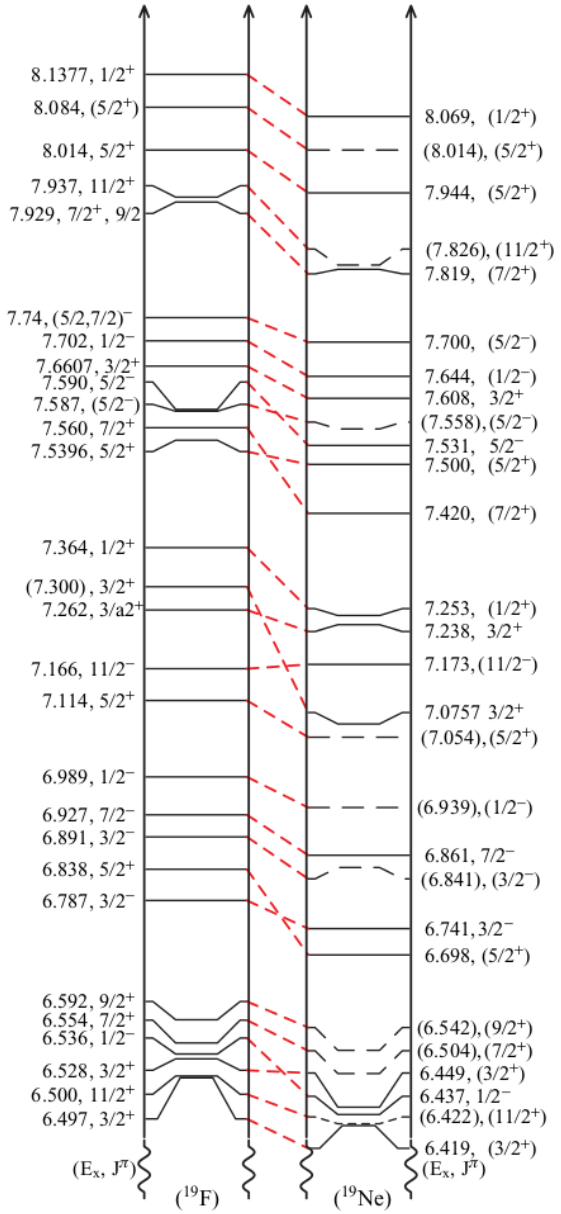

FIGURE 3.3: Level scheme of ^{19}F and its mirror ^{19}Ne with analogue assignments shown in red. Values in parenthesis are inferred from analogue levels. Note that this figure does not include the broad $1/2^+$ state seen by [80, 82] and includes the two $3/2^+$ low lying states (6.419 and 6.449 keV) currently disputed by [86]. The proton separation energies (S_p) for ^{19}F and ^{19}Ne are 7.994 and 6.411 MeV, respectively [87]. Figure taken from [88]. Note that the analogue state in ^{19}F to the 7.0757 MeV state in ^{19}Ne (E_{cm}=665 keV) in this figure is purely speculative and has not been observed, as such it cannot be used to infer properties of the latter.

3.2 Experimental Procedure

3.2.1 Preliminary Work and Pilot Beam

In the week prior to receiving beam the BGO array was calibrated using a ^{244}Cm^{13}C gamma source which allowed for hardware thresholds to be reliably set, see appendix B for more

details. The ion chamber was also gain matched such that all four anodes gave consistent voltage outputs for a given signal input.

In order to properly calibrate the magnetic and electric fields on DRAGON it is standard operating procedure to receive a pilot beam, similar in energy, mass and charge to the primary beam, which allows operators to tune attenuated beam through the target and separator such that optimal field values can be found for the electric and magnetic dipoles[3].

For the ^{18}F(p,γ) experiment a stable ^{18}O beam from OLIS (see section 2.1.3) was used for the pilot run with several beam energies. The first was at 15.47 MeV in the laboratory frame and was chosen to centre a broad resonance in ^{18}O(p,γ)^{19}F in the gas target, allowing for a radiative capture test run of a previously observed state in the relevant mass energy range. The beam was tuned through the separator and the magnetic and electric dipole fields subsequently scaled to the appropriate value corresponding to recoil particles in the 7^+ charge state, predicted to be the most abundant using the analysis from [91]. Due to the ^{18}O(p,γ) reaction's resonance strength [87], coupled with beam intensity, measured to be on average 5.22×10^9 ions/sec, an abundance of recoil events were observed in the ion chamber.

Extracting a yield for this measurement was complicated by the fact that the silicon detector scaler was left unplugged for the duration of the run. Since the number of scalers read by this detector is an essential part of the beam normalization procedure for DRAGON, any precise measurement of this value was impossible. Also the beam transmission, defined as the percentage of ions that are transmitted through the central chambers upstream aperture, was not recorded as an oversight, further complicating the result's precision. Instead, the FC reading at the start and end of each individual run were averaged in order to gain a mean beam current intensity on target, which was then multiplied by the run time and divided by the beam ion charge to get a total beam intensity on target value. Such a method is rather crude but sufficient for the purposes of a test run acting as a prelude to the main experiment. A final value of 4.1×10^{-10} was calculated for the yield, compared to a value of $5.8\pm0.8\times10^{-10}$ taken from the published resonance strength. Due to the mentioned short comings in the run the DRAGON value was close enough to the literature for us to have confidence in the separator's performance.

A second ^{18}O beam energy of 12.9 MeV was chosen to match that requested for ^{18}F. This was done not just for the purposes of calibration but also to properly account for any possible ^{18}O(p,γ)^{19}F events that could have contributed to background. The results of this run are presented later in the analysis section.

3.2.2 ^{18}F Beam Run

^{18}F beam was produced using a 500 MeV proton beam incident on a silicon carbide target, mass 18 products were extracted then ionized in a FEBIAD ion source [92] and subsequently filtered using a high resolution mass separator, with a mass resolving power of 10,000 [93]. An average $^{18}F^{4+}$ beam intensity of 1.74×10^6 ions/sec was delivered to the experiment, as determined by the two silicon scattering detectors located inside the target chamber (see later).

[3] A detailed description of the procedure necessary to tune a beam through the separator is given in appendix A

A laboratory beam energy of 12.9 MeV (717 keV/u) was chosen, to place the E_{cm}=665 keV resonance near the centre of the target, and initially the separator was tuned to transmit attenuated beam, for the purposes of calculating the optimal tune for recoil products formed inside the target. Such a calculation uses the relationship between field strength and particle momentum/energy; the radius of curvature for a charged particle in a magnetic field is dependant on its momentum, charge and the strength of the applied field (explained in more detail in section 2.2.4). As recoil momentum and charge state are similar to that of the beam the radius of curvature of the former can be extrapolated from the latter. In fact, as gamma cascades and angular distributions are often not known, the dipole scaling program at DRAGON assumes that recoil products have identical momenta to their beam particle progenitors. Hence the field strength in the magnetic dipoles remains constant when scaling to recoils, provided the attenuated beam has been tuned in an identical charge state. In an electric field, however, radius curvature is dependant on energy rather than momentum and as such the electric dipole field strengths do require scaling.

Attenuated beam runs also enabled its purity to be properly characterized, using the IC at the end of DRAGON. It was possible to distinguish between the ^{18}F ions and accompanying ^{18}O ion contaminants via the IC energy spectrum, as the latter have a smaller energy loss differential in isobutane gas. Observation of the first anode in the IC gave an initial ^{18}O/^{18}F ratio of 1/20, and this fraction was monitored at regular intervals throughout the experiment, see figure 3.4 for an example IC spectrum.

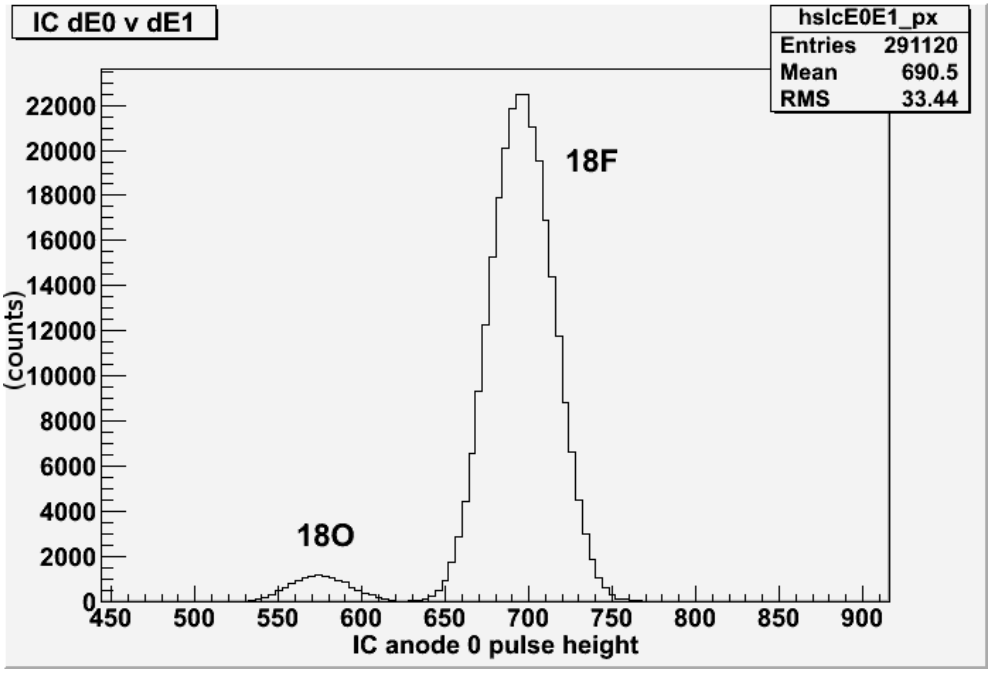

FIGURE 3.4: IC front anode signal histogram for attenuated beam. The two nuclides are clearly distinguishable as ^{18}F has a greater atomic mass than ^{18}O, resulting in a greater energy loss differential through the chambers gas.

The recoil separator was subsequently tuned to accept recoil ions with the most abundant charge state, calculated using [91], which was 6^+. Their maximum recoil cone angle was

calculated to be just 11 mrad, well within DRAGON's limits (see section 2.2.4). In total we were tuned to recoils for 9 days although due to several DAQ crashes, which did not compromise the data, and attenuated beam runs, ultimately we had 6.6 days of continuous beam on target run time.

3.3 Analysis

Extracting the reaction cross section from the number of reaction events measured requires a knowledge of the integrated beam exposure, number density of target nuclei and the overall detection efficiency, such that an experimental yield can be calculated. The number density of target nuclei is deduced from the central gas pressure, of around 7.5 Torr, chosen to ensure as much of the resonance was contained within the target region as possible without stressing the recirculation pumps. Energy loss was determined using the first dipole magnet of the separator to measure the beam energy, with and without gas in the target. The gas pressure was monitored throughout the experiment and remained within the range 7.3 to 7.6 Torr.

When calculating the total number of reactions that occurred during a run, the total efficiency of detection must be considered. In the case of a DRAGON experiment this includes: BGO detection efficiency (ϵ_{BGO}), transmission through the separator (ϵ_{ERS}), recoil charge state abundance (ϵ_{CSD}), MCP transmission (ϵ_{MCP}), efficiency of end detectors (ϵ_{det}) and detection live time (ϵ_{LT}). The number of observed recoils (N_r^{det}) must be divided by each of these factors in order to calculate the total number of reactions of interest (N_r^{tot}):

$$N_r^{tot} = \frac{N_r^{det}}{\epsilon_{BGO}\,\epsilon_{ERS}\,\epsilon_{CSD}\,\epsilon_{MCP}\,\epsilon_{det}\,\epsilon_{LT}} \tag{3.1}$$

And the yield is then:

$$Y = \frac{N_r^{tot}}{N_b} \tag{3.2}$$

Where N_b is the total integrated beam on target for the whole duration of the run. From the yield various properties of the excitation level of interest can be extracted, as described in section 1.2.

As only one recoil charge state may be transmitted through DRAGON's separator for a given run, it is necessary to calculate what fraction of all recoil ions produced have such a charge immediately before they enter MD1 (ϵ_{CSD}). As an ion's charge state distribution in a medium is dominated by its atomic number and velocity, different recoil isotopes provide an acceptable surrogate for the charge state abundance of the ^{19}Ne ions produced in the reaction. In this case charge state distributions for ^{20}Ne were measured, at an ion velocity corresponding to recoil products from the earlier ^{18}F run, and the 6^+ charge state fraction was found to be 23.7±1.1%. See appendix C for more details on how charge state abundances are determined experimentally.

Recoil ion transmission through the grid-supported foils of the MCP system was measured to be 66.5±2.1% in a later ^{15}N beam run, see appendix D for more details. The end detector efficiencies were calculated using the method described in appendix E. Attenuated beam data

was used and both the ^{18}F and ^{18}O peaks were gated on in both the IC and MCP spectra. An IC efficiency of 80.21±0.07% and a MCP efficiency of 99.42±0.01% were calculated, which combined, give a total end detector efficiency of ϵ_{det}=79.75±0.07%.

3.3.1 Beam Normalization and Energy Loss

The total number of incident beam particles is usually determined by normalizing the measured rate of target nuclei, elastically scattered by the beam into two silicon detectors mounted inside the target assembly, to Faraday Cup (FC) readings from just before and after the target [94]. However, due to the low beam intensity, the FC's could not provide a reliable current measurement and so an alternative approach was employed, using a Monte Carlo simulation of the gas target, together with elastic cross section data from [82] and SRIM [95] energy loss calculations. The latter provided an energy loss value 8.9% higher than that measured experimentally for the ^{18}O beam run however. This was not entirely unexpected as inspection of SRIM's experimental database showed that calculated stopping powers were consistent with experimental values to the order of 8.3% for hydrogen targets. Due to ^{18}F's similarity in charge and mass its energy loss value, as determined by SRIM, was corrected by the same factor and 9.8% adopted as an estimate as to its uncertainty. This value was slightly larger than the correction factor's uncertainty due to the effects of variations in pressure during the run, which affected the beams energy loss. A final energy loss of 458±45 keV resulted, which is 24.1±2.4 keV in the centre of mass frame.

The Monte Carlo simulation then enabled the number of incident beam particles to be determined, from the number of events detected in the silicon detector inside the target, which was angled at 30 degrees to the beamline. A detailed discussion of this procedure is given in Appendix F. Variations in beam position, energy loss and angle were considered in the simulation and gave a maximum deviation of 10% in the calculated beam intensity, which was then adopted for the simulation's accuracy so as to account for any such systematic effects. Comparisons of the experimental data points in [82] with the corresponding R-matrix fit were also used to determine uncertainty in the input data, approximated to be 15%. Adding the two in quadrature gave a total uncertainty of 18% in the beam normalization analysis. Given that the total uncertainty in the reaction yield was dominated by the low count rate of recoil events such approximations in the beam normalization were inconsequential with regards to the final result. Using this simulation, the ratio $\frac{N_{beam}}{N_{Sb}}$ was found, allowing the total integrated beam intensity on target to be calculated from the silicon detector data, giving a value of $9.9\pm1.8\times10^{11}$ ^{18}F ions.

The simulation's ability to calculate the beam intensity was later tested by comparing results from the simulation to the normal DRAGON procedure for the ^{76}Sn(α,γ)^{80}Kr run (see chapter 4 for details), which had precise FC cup data available. Cross section data was approximated to be purely Rutherford as elastic scattering is dominated by the Coulomb interaction at the simulated energies in this mass range [27]. Simulation results for the total integrated beam agreed to within 10% of those calculated using the traditional method (see section 4.3.1 for a more detailed explanation of this method).

3.3.2 Particle ID

Three potential sources of background were identified: ^{18}F beam particles that managed to pass through the recoil separator (referred to as *leaky beam*), ^{18}O leaky beam contaminants and ^{19}F recoil events from ^{18}O beam contamination. Using attenuated beam, a ΔE plot from the IC allowed the locus of such background events to be determined, as displayed in figure 3.5. From this figure the ^{18}F attenuated beam events are visible in the larger black locus, with the smaller black locus being due to ^{18}O contamination. There is a clear tailing effect below the ^{18}F peak, due to some of the incident ions scattering and loosing energy in the detector gas volume. There are also high energy tails located to the right and above the main peak due to pile up. This effect occurs when the count rate is large enough that some of the pulses generated by ion events overlap, such that the resulting signal is greater than that which could be produced by a single event [35].

Two events appeared in a region of minimal background, to the lower right of the ^{18}F locus in figure 3.5, and were considered to be recoil candidates. Another three events appeared in the IC region corresponding to ^{18}F leaky beam, which was expected when the total beam intensity and DRAGON's typical suppression factor are taken into account. However, the uncertainty in ion energy loss in the IC meant that these could also potentially have been recoil events. This issue was resolved by looking at the MCP data which gave TOF information on each particle, as attenuated beam runs provided an expected TOF region where leaky beam particles would appear. The three suspected leaky beam events all have TOF values consistent with the ^{18}F region, to within 2σ, and the two recoil candidates resided in a region with minimal background, calculated to be just 3×10^{-5} events per channel (calculated by considering ratios of events in attenuated beam and recoil runs for a given region, see figure 3.6).

When calculating the background in the MCP signal region, a gate was placed on this spectrum such that only events that appeared above channel 174 in IC0 were included, a value that corresponds to the highest channel in which we observed ^{18}O(p,γ)^{19}F events (see figure 3.7). The second peak in the attenuated beam data is most likely an electronic artifact, and as it accounts for just 0.33% of the real peak events any recoils that experience this same effect would still be distinguishable from leaky beam, in this spectrum and in figure 3.5.

The level of isobaric contamination from ^{18}O was measured, at regular intervals, by sending attenuated beam directly into the IC and measuring the ratio of peaks due to ^{18}O and ^{18}F (see figure 3.5). The ^{18}O:^{18}F ratio was observed to decrease from 1:20 to 1:260 throughout the experiment, as the residual gas in the ion source diminished. The position of the ^{18}O and ^{18}F peaks in the IC spectrum was reproduced each time, and the position of the ^{18}O peak was in good agreement with the peak from the ^{18}O beam runs.

The IC spectrum from the ^{18}O run is shown in figure 3.7 together with the position of the two ^{19}Ne recoil events. Analysis of the silicon detector data together with the isobaric contamination ratio for these runs allowed the expected number of background events from ^{18}O(p,γ)^{19}F to be calculated. Only 0.40$\pm$0.08 background ^{19}F events were expected in total and a negligible fraction of them were predicted to appear above channel 174 during the ^{18}F(p,γ)^{19}Ne run.

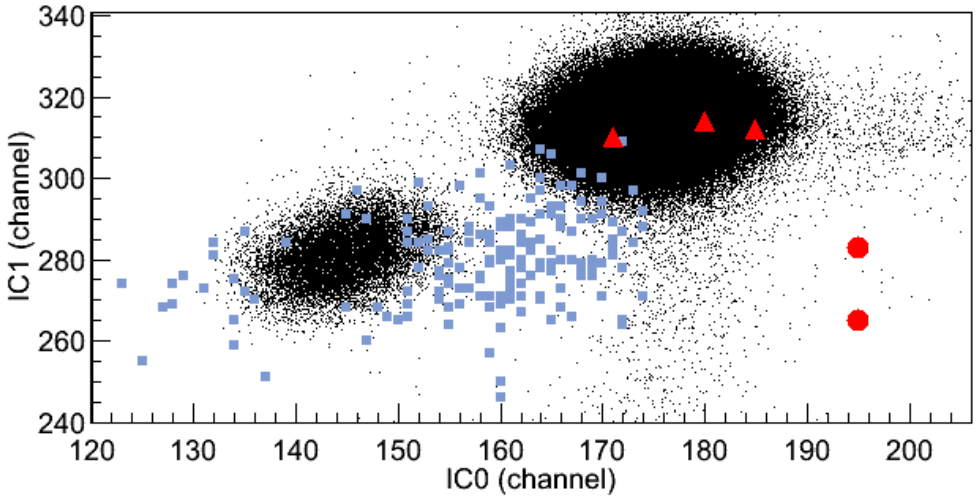

FIGURE 3.5: Energy loss vs. energy loss plot obtained from the first two anodes in the IC. The attenuated beam run is shown in black and two well-separated loci are clearly visible signifying the presence of both ^{18}F and ^{18}O. Circles (triangles), both red, correspond to observed ^{19}Ne (^{18}F) events when the separator was tuned to recoils. Squares (blue) correspond to ^{19}F recoils during the separate ^{18}O beam run.

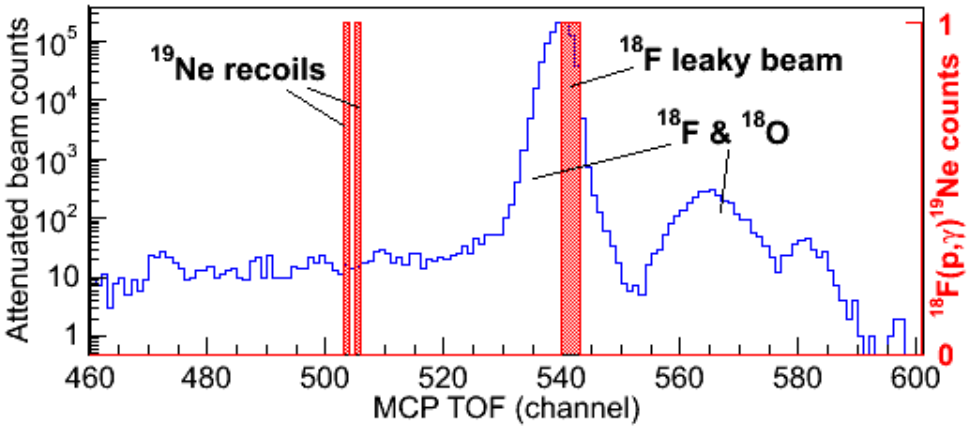

FIGURE 3.6: MCP time of flight spectrum showing where ^{18}F was observed during the attenuated beam run (blue) and events when tuned to ^{19}Ne recoils (red). Leaky beam during the recoil run is clearly identified as it appears in the ^{18}F peak.

There were also events in the lower energy region of the IC spectrum corresponding to particles scattered inside the recoil separator, changing charge state and losing momentum, that were able to reach the IC via an extremely erratic path. As they appear so far away from the leaky beam and recoil loci they do not contribute to the region of interest however.

Neither of the potential ^{19}Ne recoils had a coincident γ-event detected in the BGO's which is often used as an additional source of background suppression. Lack of ^{19}Ne level structure data also made predicting the BGO efficiency difficult. A GEANT simulation was used with gamma cascades assumed from ^{19}F states in an excitation region near to that populated in the ^{18}F run (E_x=7090→7066 keV). The results are presented in table 3.1 and, once the BGO live time for the run (98.2%) is taken into account, give a detection efficiency range of

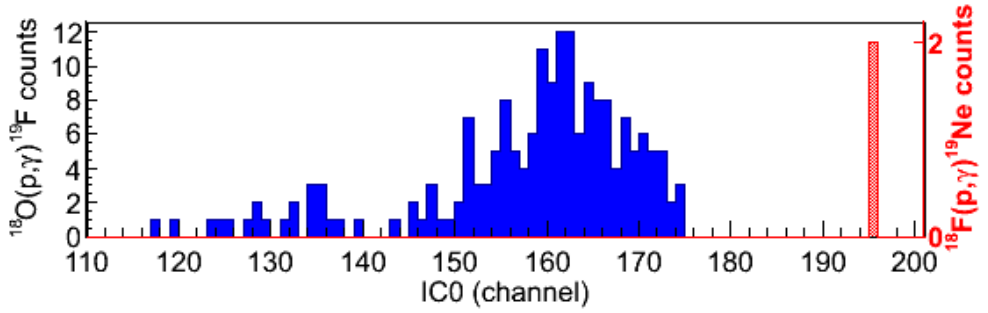

FIGURE 3.7: Energy loss plot from the IC's first anode showing the position of ^{18}O(p,γ)^{19}F (blue) and ^{19}Ne events (red). Level schemes taken from [87].

^{19}F level	ϵ_{BGO}
DC	62%
6927 keV	66%
7166 keV	87%

TABLE 3.1: BGO gamma detection efficiencies (ϵ_{BGO}) obtained from the Geant4 simulation for states in ^{19}F in the excitation region close that that populated during the ^{18}F(p,γ)^{19}Ne run. DC refers to a purely ground state transition. Level decay schemes taken from [87].

61→85% (see appendix I for more details of this simulation). As only two events in the recoil region were observed, the lack of γ-heavy ion coincidence events is not inconsistent with the observed singles yield.

In order to gain confidence in the BGO simulation's ability to calculate gamma detection efficiencies in this mass and energy region, further analysis was conducted using the ^{18}O(p,γ)^{19}F run data. Placing a gate on the MCP time of flight data, together with the IC0 vs IC1 data from figure 3.5, allowed for recoil events to be discerned in both singles and coincidence data sets. A gamma detection efficiency could then be determined by dividing the total number of coincidence recoil events by the total number of recoil events[4]. The gamma detection efficiency was subsequently calculated to be 69.9±3.8%[5] for the ^{18}O run. This compares favourable with the simulation's calculations, which were done for a purely ground state transition and the two nearest states (8650 and 8629 keV) to the excitation energy range accessible within the target (8675→8654 keV). The efficiency calculations are displayed in table 3.2 and the level decay schemes were taken from [87]. The comparison between the simulations results and the experimentally determined value compares well enough for the author to be confident in its ability to estimate gamma detection efficiencies for ^{19}Ne in this energy region.

All of these techniques and data cuts can give a high confidence that the two events observed are ^{19}Ne recoils, in a region of negligible background. A detected recoil count of $2.0^{+4.8}_{-1.7}$ was calculated, at the 95% confidence level, using the profile likelihood technique outlined in section 2.3.6. This process involves characterizing the likelihood function for the

[4]The coincident event count also has to include the gamma array live time, in this case 95.4%.

[5]Uncertainty calculated using binomial statistics, treating each recoil event as a trial, in the same way as described in appendix E

^{19}F level	ϵ_{BGO}
DC	63%
8650 keV	71%
8629 keV	74%

TABLE 3.2: BGO gamma detection efficiencies (ϵ_{BGO}) obtained from the Geant4 simulation for states populated during the ^{18}O(p,γ)^{19}F run. DC refers to a purely ground state transition. Level decay schemes taken from [87].

Source of uncertainty	Uncertainty
Beam Normalization	18%
Charge state distribution	1.3%
Target stopping power	9.8%
MCP efficiency	3.4%
Target Length	3.3% [31]

TABLE 3.3: List of systematic experimental uncertainties

data, including the parameters of interest as well as nuisance variables. For this analysis the signal and background were treated as Poisson distributions whilst the beam normalization, detector efficiencies and other nuisance parameters were modelled as Gaussian. The profile likelihood, given as λ, can then be calculated giving the likelihood of observing the given parameter of interest as a function of that parameter only, in the absence of nuisance ones. A more detailed discussion of this method's implementation is given in Appendix H. The main sources of systematic uncertainties are given in table 3.3.

Chapter 4

Measuring the ^{76}Se(α,γ)^{80}Kr Reaction Rate

This reaction's importance is due to its time reversed counterpart's influence on the abundance of p-nuclei, which are the 35 proton rich (neutron deficient) nuclides heavier than ^{56}Fe that cannot be created via the s- or r-processes (as described in section 1.1.11). This chapter expounds the experimental procedure necessary to extract an experimental limit on these reaction cross sections at astrophysical energies, under laboratory conditions.

4.1 Background

4.1.1 P-nuclei

Of the nuclei heavier than ^{56}Fe, numerous isotopes on the proton rich side of the valley of stability cannot be synthesized solely via the neutron capture processes and β^- decays (see figure 4.1). The 35 naturally occurring nuclides that fit this template are referred to as p-nuclei and generally exhibit a natural abundance one to two orders of magnitude smaller than their respective neutron capture mass neighbours. There is, however, thought to be a significant contribution to the production of several of these nuclides from the slow neutron capture process [96] so their current number should not be considered definite.

Candidates for production site(s) and mechanism(s) remain ambiguous with overall production mechanism termed the *p-process*. The currently favoured scenario is the ONe shell of massive stars during their core collapse stage [27]. This model however, fails to generate their observed solar abundances, whilst additional reaction rate uncertainties arise from individual reactions experimental data of which is scarce [27].

Possible production mechanisms include a sequence of (p,γ) reactions originating from lower mass nuclides although Coulomb repulsion, a necessity for a proton rich environment and the prevalence of (γ,p) photodisintigrations significantly inhibits this process at astrophysical energies. A series of (γ,n) reactions from s/r seed nuclei present another feasible mechanism for production, termed the γ-process (see figure 4.2). The currently accepted scenario is that several independently operating processes contribute to the overall abundance of p-nuclides [27].

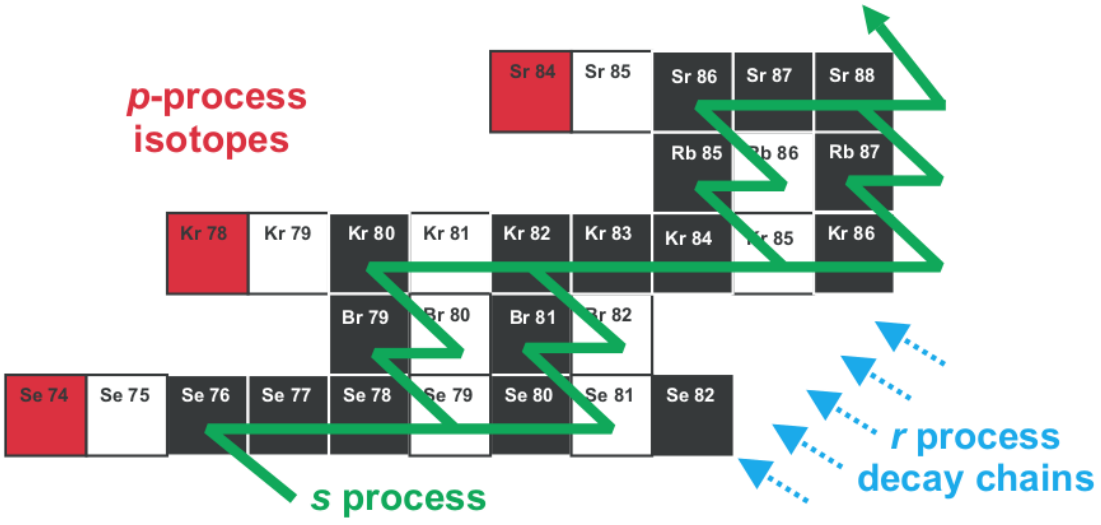

FIGURE 4.1: Illustration of how the valley of stability shields p-nuclei from the neutron capture processes and β^- decays that synthesize other high mass nuclides, taken from [27].

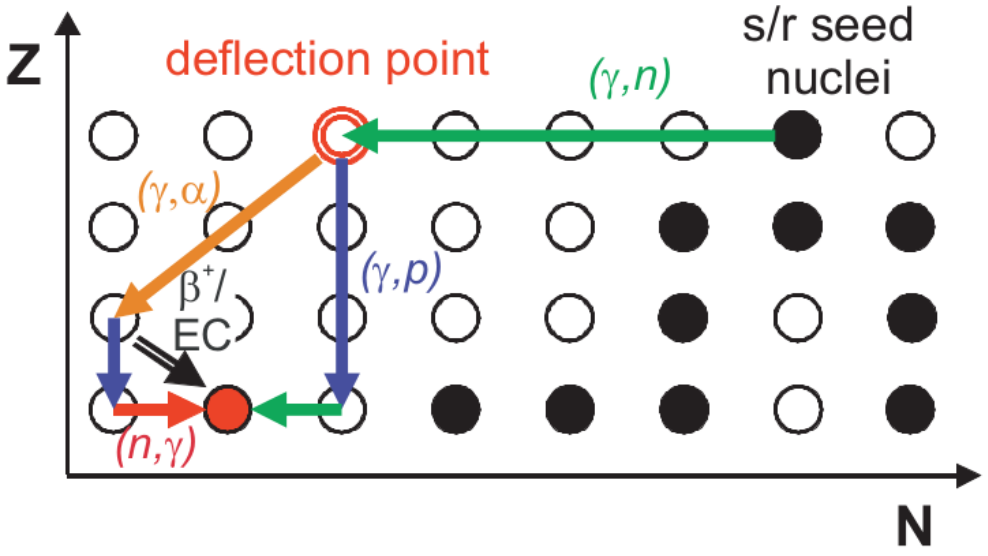

FIGURE 4.2: The γ-process consists of a series of (γ,n) photodisintigration from s/r seed nuclei punctuated by (γ,α) and (γ,p) reactions at specific branching (or deflection) points, taken from [27].

4.1.2 Motivation

The γ process reaction pathways leads to the proton rich side of the valley of stability, initially via a single isotope chain, however at some point (γ,p) and/or (γ,α) reactions become dominant and the pathway is shifted to a lower isotope or diverges. The location of such instances are referred to as branching points [97] and locating them can be critical when calculating the final abundance of p-nuclei.

Despite the large number of reactions contributing to the γ-process only a select few have a large impact on abundance calculations [97, 98], one of them being ^{80}Kr(γ,α)^{76}Se. This is due to ^{80}Kr being identified as a branching point nucleus, as illustrated in figure 4.3. If

the (γ,p) and/or (γ,α) reactions dominate over the (γ,n) at this location then the pathway is diverted into either the Br or Se elemental chains, significantly inhibiting production of the p-nucleus ^{78}Kr.

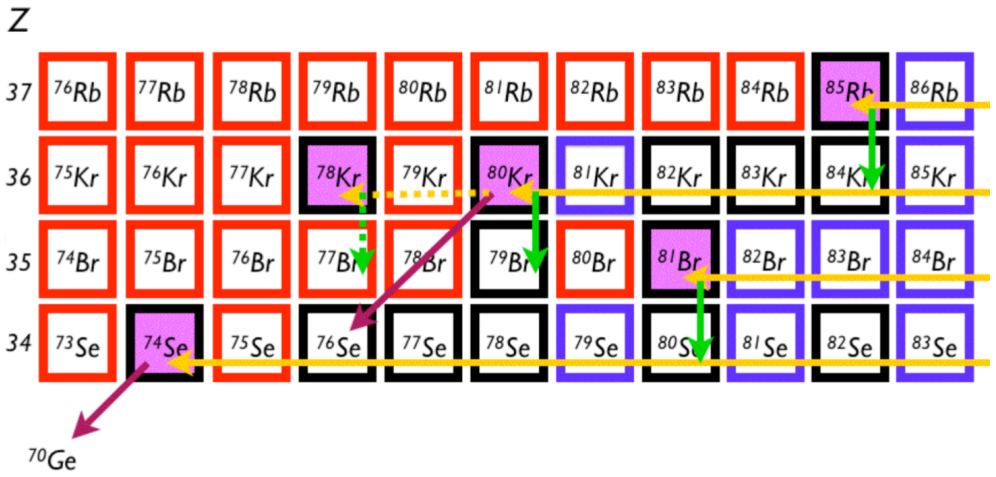

FIGURE 4.3: γ-process pathway, highlighting ^{80}Kr as a branching point, based on the study by Rauscher [97]. If the (γ,p) and/or (γ,α) reactions dominate over the (γ,n) at this location then the pathway is promptly diverted into either the Br or Se elemental chains. Taken from an EEC proposal, authored by A.M. Laird.

Calculating reaction rates for the γ-process is complicated by the nature of nuclear reactions in this temperature and mass regime. As higher mass nuclei have a greater nuclear level density and larger Coulomb barriers, capture reactions require a higher temperature, and so take place through a distribution of excited states in the target nuclei (see section 1.2.5 for more details). Experiments in the laboratory only provide data on the cross section originating from the ground state of the target nuclei and so need to be supplemented by theory. As there are very little experimental data in the energy region of interest, greater knowledge constraining the reaction rate's uncertainties is needed to improve theoretical predictions. Such data may also allow for the negation of certain astrophysical models [27].

Currently, the majority of γ-process reactions are calculated using the Hauser-Feshbach statistical model [99], which assumes a large number of available states in the compound nucleus. As the relevant reactions pertain to heavy nuclei in an excitation region far above the ground state, this is assumed to be the case. Such statistical models require various input parameters, including optical potentials (the potential a particle experiences from a nucleus due to the strong interaction), level densities and nuclear masses. These parameters do not always have experimental constraints and so theoretical calculations of cross sections and reaction rates should not be regarded as definite; experimental data is always desired where absent.

The ^{80}Kr(γ,α) rate can be inferred by the time reversed reaction ^{76}Se(α,γ)^{80}Kr, via the reciprocity theorem as outlined in section 1.2.5. As previously mentioned, laboratory data only gives the ground state (g.s.) contribution to the cross section of interest, and the difference between the total stellar rate and that arising purely due to the ground state is termed the *stellar enhancement factor* (R^*/R_0). One problem with this quantity, however,

T(GK)	E(MeV)	f_{SEF}	X_0
2.5	4.32→6.47	0.914	0.749
3.0	4.69→6.62	0.808	0.661
3.5	4.87→6.68	0.779	0.611

TABLE 4.1: Gamow window, stellar enhancement factor and ground state contribution at temperatures relevant to the p-process, for the reaction ^{76}Se(α,γ). Taken from [101].

is that it does not distinguish between a purely g.s. contribution to the stellar rate or an amalgamation of contributions, from various states, that result in a reaction rate equal to the former. In both cases f_{SEF}=1, however the latter can represent the case where a significant contribution to the stellar rate arises from excited states in the target nuclei (the situation is described in greater depth by Rauscher *et al.* [100]).

For this reason it is more useful to instead use the ground state contribution to the stellar rate (X_0), defined as:

$$X_0 = \frac{R_0}{\int \sigma^{eff}(E)\Phi(E,T)\,\mathrm{d}E} = \frac{1}{f_{SEF}G_0} \tag{4.1}$$

where R_0 is the rate due to only the ground state and the denominator represents the rate from the effective cross section (σ^{eff}), which is a weighted sum over every energetically accessible transitions cross section (defined in equation 1.24). $\Phi(E,T)$ is the Maxwell Boltzmann distribution and G_0 is the partition function of the target, normalized to the ground state spin (defined in equation 1.25).

X_0 can only take values between 0 and 1 and, also, it can be shown [100] that the relative magnitude of X_0 remains constant even in the presence of large uncertainties in the g.s. cross section, making it a convenient and robust unit of comparison. Given the prevalence of low X_0 values for γ induced reactions in the mass and energy range of interest [27], radiative capture reactions represent a far more desirable mechanism for observation. Observation of table 4.1 shows that, in the case of ^{80}Kr(γ,α), the ground state is the dominant contributor to the astrophysical rate at the relevant temperatures. As is the case for a significant portion of p-process reactions, this does mean however that any experimental measurements have to be supplemented by theoretical calculations.

Cross section measurements are most useful when conducted in the energy region relevant to stellar temperatures, as the sensitivity of reaction rates to a specific nuclear property can vary strongly as a function of temperature. Here, sensitivity has a specific definition [100]:

$$s = \frac{v_\Omega - 1}{v_q - 1} \tag{4.2}$$

where $v_q = q_{new}/q_{old}$ and $v_\Omega = \Omega_{new}/\Omega_{old}$. The former is a measure of how much a specific property (q) is varied and the latter gives a measure of how much the resulting parameter of interest (Ω) varies accordingly. s can only take values between 1 and 0, with 1 representing the case where the result varies by a factor consistent with the variation of q. At the other extreme, when s=0, there is no effect on Ω from the parameter q.

In the case of low mass p-nuclides, such as ^{76}Se, the temperature range of interest is 2.5→3.5 GK [27], corresponding to a centre of mass energy region of 4.32→6.68 MeV. It can be seen in figure 4.4 that the α width dominates the ^{76}Se(α,γ) astrophysical rate sensitivity for the temperature region pertaining to the p-process. It should be noted that in this figure the ratio v_q is equal to 2, that is, the widths were increased by a factor of two when calculating the sensitivity from equation 4.2. It can also be seen, from figure 4.5, that the reactions ground state cross section sensitivity is also dominated by the α width in this region. Thus this reaction provides us with a good case for investigating how well the available theoretical models are at calculating α widths in this mass/energy region.

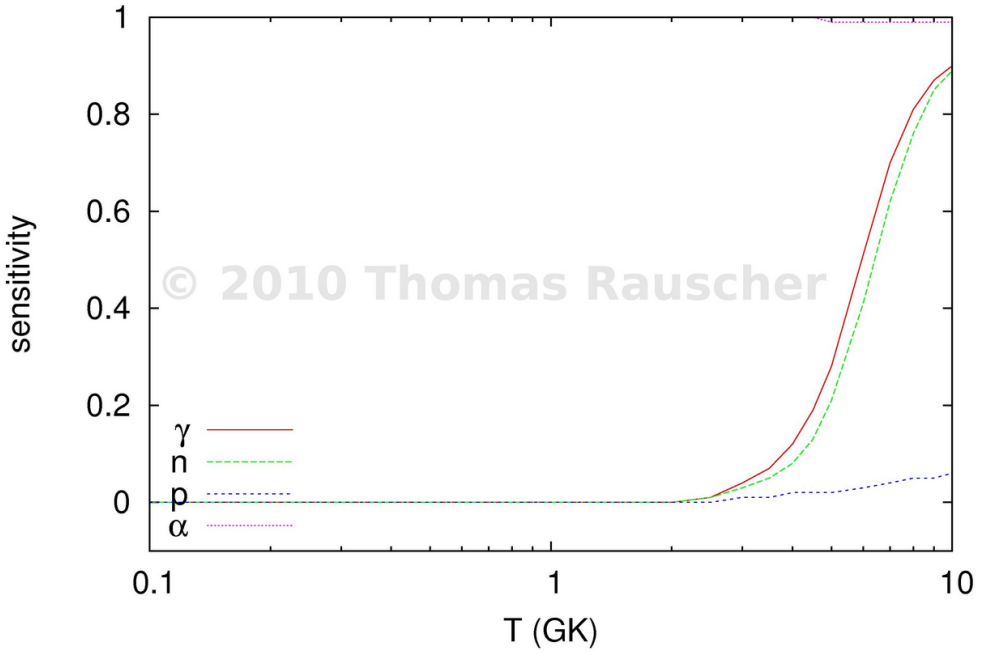

FIGURE 4.4: The sensitivity of the ^{76}Se(α,γ) astrophysical reaction rate that results from increasing the γ, neutron, proton and α partial widths by a factor of two. The temperature range of astrophysical interest is 2.5→3.5 GK [27]. Note that the sensitivity of the α partial width is equal to one below 4 GK and does not show on the figure. Taken from `http://nucastro.org/nonsmoker.html`.

4.1.3 Previous Work

As already mentioned, the low ground state contribution to the cross section for γ-induced reactions in the mass and energy range relevant to p-nuclei production makes observation of the time reversed radiative capture reaction more desirable [27]. Experimental data remain scarce relative to the large number of participating reactions in the γ-process, with two distinct techniques currently being used for cross section measurements; the in-beam γ-detection technique and the activation method.

In-beam γ-detection technique In this scenario, the prompt γ emission is observed in solid state or scintillation detectors and used to determine the exact number of capture reactions that have taken place. Complications arise due to the dense level scheme of heavy

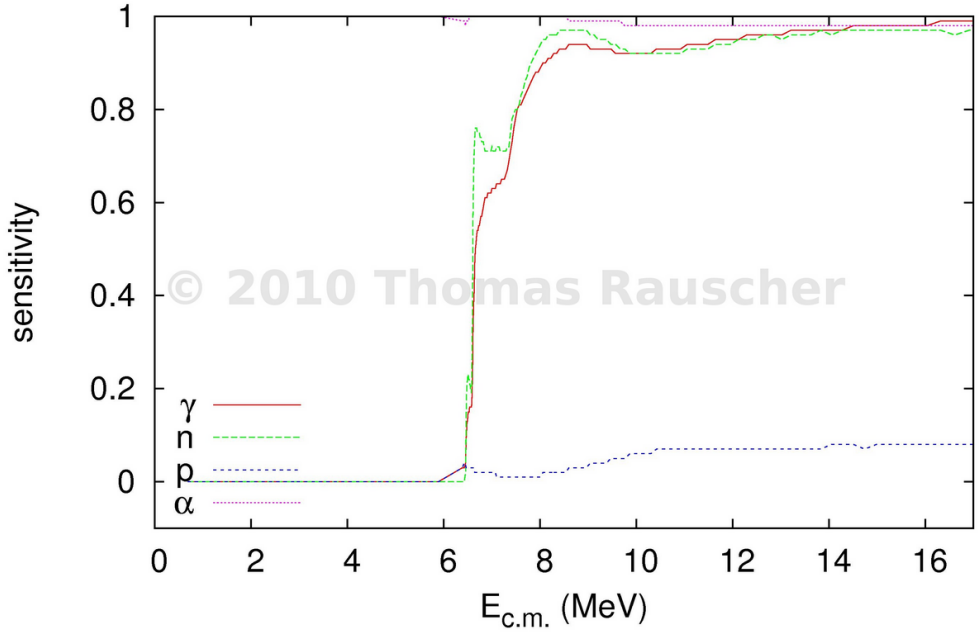

FIGURE 4.5: The sensitivity of the ^{76}Se(α,γ) g.s. cross section that results from increasing the γ, neutron, proton and α partial widths by a factor of two. Taken from `http://nucastro.org/nonsmoker.html`.

nuclei in the energy region relevant to the γ-process, resulting in complicated decay schemes and anisotropic emission distributions. Failure to discern a specific transition can result in an underestimation of the cross section. This can be somewhat remedied by utilizing a 4π summing crystal, as most of the solid angle is covered then the sum of all the γ rays detected should give a single photo peak corresponding to the excitation level populated. Knowledge of the decay scheme is still required for the purposes of efficiency calculation however. Previous studies using this method include [102–110].

Activation method This method involves detecting the particle decay of the product nuclei after it has been produced, rather than observing the prompt γ as described in the previous method. This does require, however, that the final nucleus be radioactive, with a decay half life that allows for detection of the decay to take place on a practical timescale. In the nuclei region relevant to the p-process, a significant portion of the radioisotopes decay via the β^+ channel followed by a γ emission from the excited state of the daughter nucleus. The detection of this γ emission is therefore used in the majority of such experiments, with a few exceptions such as in the case of alpha emission or electron capture of the daughter, when the alpha particle and characteristic X-ray, respectively, are observed instead. Previous studies using this method include [111–113, 113–125].

The current status of experimental information pertaining to radiative capture cross sections relevant to the γ-process is illustrated in figures 4.6 and 4.7. Experimental (α,γ) data in the mass and astrophysical energy region near ^{76}Se are scarce, however there was an in beam study on ^{70}Ge by Fulop *et al.* [108] and the authors did find good agreement with theoretical predictions. Work by Harissopulos *et al.* [109], using the in beam technique on

^{91}Zr, also showed agreement with theoretical Hauser-Feshbach models, although the energy range was above the astrophysically important region. The study also revealed the theoretical uncertainties arising from the various optical potentials and nuclear level densities available in the literature. To the author's knowledge, the current study represents to first time that a recoil separator has been used for the purposes of observing cross sections relevant to the γ-process.

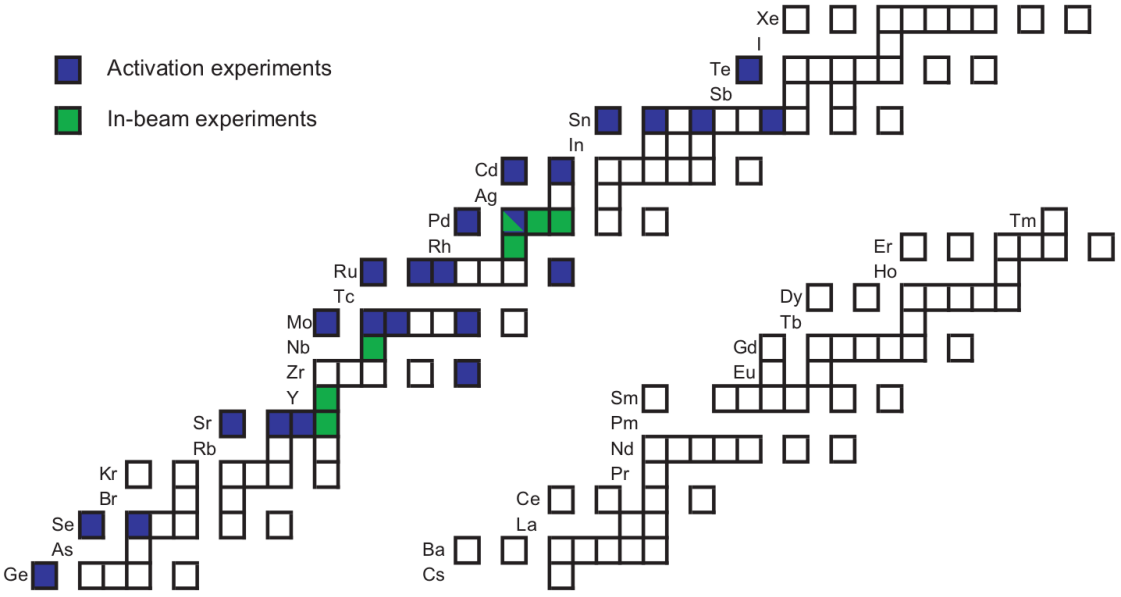

FIGURE 4.6: Illustration of nuclides that have experimental (p,γ) cross section data relevant to the γ process available. Figure taken from [27].

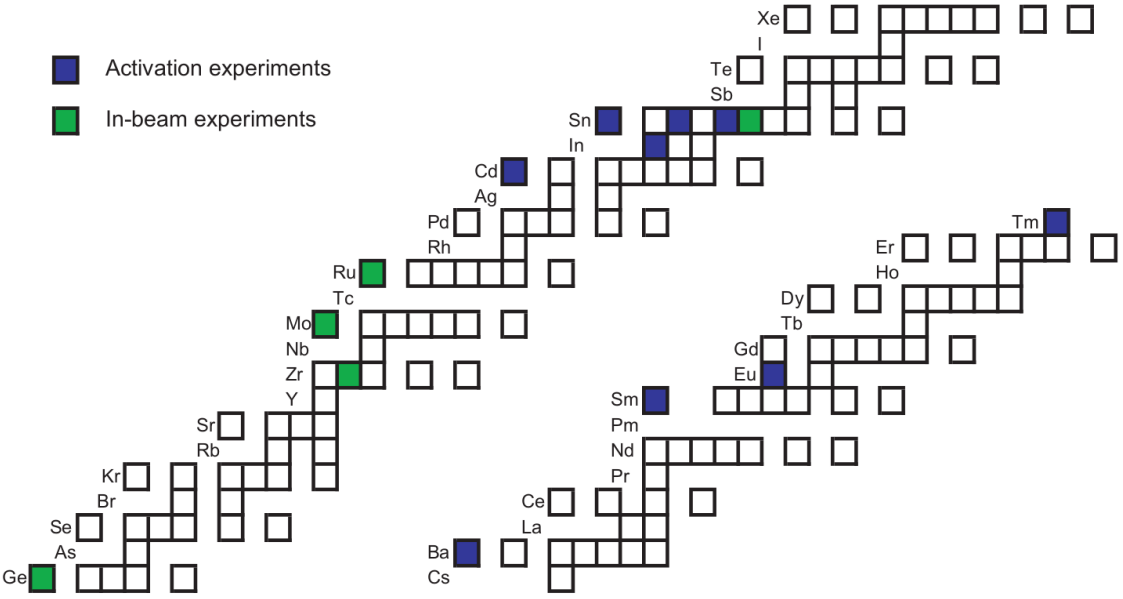

FIGURE 4.7: Illustration of nuclides that have experimental (α,γ) cross section data relevant to the γ process available. Figure taken from [27].

4.2 Experimental Procedure

In much the same fashion as the previous experiment, ^{18}F(p,γ), observation of ^{80}Kr recoils at astrophysical energies requires a large background suppression, due to the low cross sections resulting from the sub Coulomb barrier regime. In this case such suppression is provided by DRAGON; the reader is referred to section 2.2 for a more detailed description of the facility. The time reverse counterpart of the astrophysically important reaction ^{80}Kr(γ,α) was the one observed for the reasons outlined in the previous section.

4.2.1 Initial Test Runs

Measuring high-mass reactions is part of a broader project of expanding DRAGON's overall performance capabilities, which was originally designed for capture reactions in the mass range A=12→27 [31]. As a result it was deemed appropriate to conduct a test experiment in this mass range to act as a proof of principle for the ^{76}Se run. The reaction chosen was ^{58}Ni(p,γ)^{59}Cu as the separator gave beam ions a neighbouring charge state momentum separation of 1%, roughly the same as ^{76}Se(α,γ). This allowed the group to determine if the separator's suppression and rigidity (momentum to charge ratio) was great enough to successfully discern recoil events from such high mass radiative capture reactions. It should be noted that this test run and the subsequent one (see later) were conducted before the author joined the DRAGON group.

^{58}Ni beam was received with an energy of 1.432 keV/u so as to position the resonance at 1399 keV at the centre of the target. Due to the limits on DRAGON's target pressure, beam and recoil particles formed in the gas could not reach a high enough charge state in appreciable enough amounts to be bent around the separator, greatly reducing the total detection efficiency (N_r^{det}/N_r^{tot}). This necessitated the use of a charge state booster foil, made from 50 nm thick SiN, which was mounted on the downstream side of the target chamber. The separator was then tuned to transmit recoil ^{59}Cu ions with charge and mass slits set to minimize the background rate whilst not reducing recoil transmission. A leaky beam rate of 5 Hz on the focal plane detector was finally achieved, which scaled up linearly with the beam intensity requested for the ^{76}Se run (2.5×10^{11} pps) was still within the envelope of the DAQ systems capabilities. Approximate numbers for overall beam suppression were extracted for both singles and coincidence modes: $4.17\pm0.04\times10^{8}$ and $9.7\pm0.9\times10^{10}$ respectively [126]. An estimated yield (N_r^{tot}/N_b) of 7×10^{-12} was taken from Non-smoker data for the ^{76}Se(α,γ) run suggesting DRAGON's suppression and PID capabilities were sufficient for a cross section measurement. Data analysis yielded a resonance strength that was consistent with previous work [126], giving confidence to DRAGON's performance in this mass region.

A ^{84}Kr beam was also utilized, with a SiN foil downstream of the target, for the purposes of charge state distribution and suppression measurements. The maximum voltage achievable on ED1 during this run was 210 kV, although 220 kV had previously been achieved, illustrating the inconsistency observed in maximizing ED1's voltage which currently represents one of the main boundaries in DRAGON's ability to measure high mass reactions. The separator was then subsequently tuned for ^{88}Sr recoils from the ^{84}Kr(α,γ) reaction. The background

rate at the focal plane was lower than the Ni run at ≈0.5 Hz and approximate calculations for beam suppression, in singles and coincidence modes, yielded ≈1.1×10^{9} and ≈1.4×10^{10} respectively. These results were again within the DAQ's operating capabilities and provided further confidence in DRAGON's ability to discern real recoil events from radiative capture reactions, in the high mass regime.

4.2.2 ^{76}Se Beam Run

The ^{76}Se beam was produced at the OLIS ion source (see section 2.1.3) and sent to DRAGON with an energy of 1.51 MeV/u, in a 12^{+} charge state, with an average intensity of 2.1×10^{10} pps. As was the case with the ^{58}Ni run a charge state booster foil was utilized so that higher recoil charge states could be obtained for the purposes of transmission through the separator; lower charge states cannot be sufficiently bent by the dipole fields in this mass range. This is due to the fact that greater charge states require lower field strengths to transmit, that are within the design parameters of DRAGON's dipole elements. As there were issues with the SiN foils[1] in the previous high mass runs the decision was made to use aluminium foils instead.

Initial calculations suggested that a 1.5 MeV/u ^{76}Se beam would produce ^{80}Kr recoils with a post foil energy of approximately 1.3 MeV/u, with a charge state distribution peaking around 22^{+} with an abundance of 23.9%[2]. However, due to the field constraints on the separator, it was predicted that DRAGON could only transmit recoil ions down to the 25^{+} charge state, with an estimated abundance of 3.5%. Cross section predictions using the NON-SMOKER code [127] suggested that even at this lower abundance charge state enough recoil events could be produced to be discerned in the end detectors over the course of the experiment. Hence the separator was tuned to a charge state of 25^{+} when transmitting recoil events.

No pilot beam was utilized as the primary beam was stable and intense enough to be tuned independently, and so after attenuated beam was successfully tuned through the separator, the fields were scaled to the corresponding recoil energy. However, after three days of running there were still no discernible recoil candidates despite the NON-SMOKER cross section corresponded to several hundred recoils per day.

The voltage reading on ED2 was 5.30% lower than the theoretical value, predicted from the voltage applied to ED1, and although the predicted field doesn't always agree perfectly with the measured value this discrepancy was significant enough to be noticed. In order to test the separator's tune the beam energy was lowered to correspond to that of the recoils we were hoping to observe, and in doing so measured ED2's voltage to be 3.64% lower than expected. This discrepancy meant that the field across ED2 was not scaling linearity with applied voltage, a phenomenon rarely observed due to the fact that at the time of writing, high mass measurements that require high fields strengths are still in their infancy at DRAGON.

A rational course of action was taken and ED2 was set to 3.64% lower than predicted and the beam energy raised to its previous value, in order to take the observed non linear scaling into account. At this new tune however the leaky beam rate was substantial, to the order

[1] They repeatedly broke during the run, possibly due to beam heating
[2] Calculations conducted using the program *csd*.

of 10 kHz as seen in the IC, making it very difficult to discern any recoil events even with γ coincidence gating. This high trigger rate also significantly lowered the system live time to just 40%, essentially halving the experiment's beam time. The situation was somewhat remedied by lowering the ED2 setpoint voltage as the IC detection rate was observed to fall exponentially when doing so (see figure 4.8). It was decided that we would set ED2 at 164.3 kV, 3.97% lower than the theoretical value, as any potential loss in transmission would be more than compensated for in terms of lowering the leaky beam rate by several orders of magnitude.

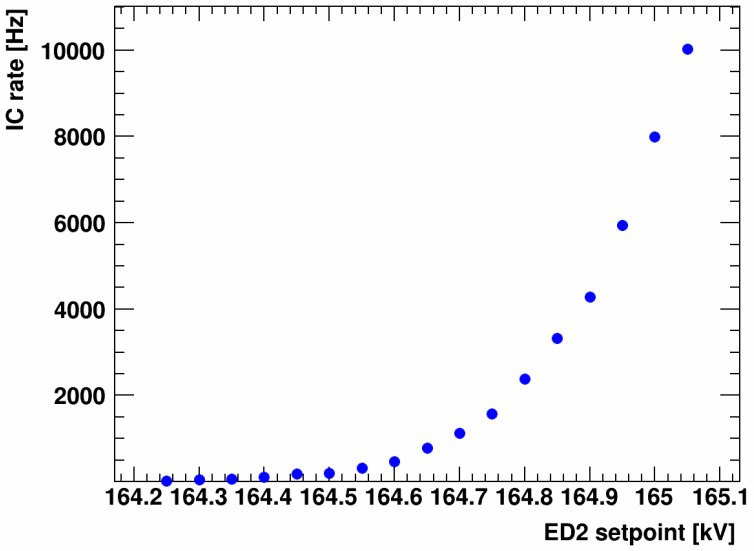

FIGURE 4.8: Graph showing exponential decline of leaky beam rate in the IC when the ED2 setpoint voltage was decreased.

After a few hours clear signs of recoil events become visible (discussed in further detail in the next section) confirming the suspected scaling problems with ED2. The setpoint voltage was subsequently raised slightly to 164.65 kV, to be closer to the theoretical value, and the charge slits were narrowed from 25 to 24 mm to help compensate for additional leaky beam transmission. This was permitted as GEANT simulations indicated that closing the slits by 1 mm would not affect the transmission of recoil particles.

Once a few hundred recoil candidates had been observed, the decision was taken to re-tune to a new beam energy such that we could get two cross section measurements for separate centre of mass energies. The new beam energy was measured to be 1.37 MeV/u, after the charge state booster foil, and ED2 was again observed to have a lower than predicted (-3.5%) setpoint voltage. After tuning to recoils the leaky beam rate was again observed to be unfeasibly high, hence the ED2 setpoint voltage was lowered until the rate dropped to $\approx$1 kHz, in the same manner as when at the higher beam energy. We continued to run with this beam energy, with the separator tuned to transmit recoils in the 25+ charge state (for the same reasons as stated earlier) until the end of the experiment.

4.3 Analysis

In a similar fashion to that described previously, in section 3.3: when calculating the total number of reactions that occurred during a run, the total efficiency of detection must be considered. In the case of a DRAGON experiment this includes: BGO detection efficiency (ϵ_{BGO}), transmission through the separator (ϵ_{ERS}), recoil charge state abundance (ϵ_{CSD}), MCP transmission (ϵ_{MCP}^{trans}), efficiency of end detectors (ϵ_{det}) and detection live time (ϵ_{LT}). The number of observed recoils (N_r^{det}) must be divided by each of these factors in order to calculate the total number of reactions of interest (N_r^{tot}):

$$N_r^{tot} = \frac{N_r^{det}}{\epsilon_{BGO}\,\epsilon_{ERS}\,\epsilon_{CSD}\,\epsilon_{MCP}^{trans}\,\epsilon_{det}\,\epsilon_{LT}} \tag{4.3}$$

And the yield per incident ion is then:

$$Y = \frac{N_r^{tot}}{N_b} \tag{4.4}$$

where N_b is the total integrated beam on target for the whole duration of the run. From the yield various properties of the reaction's rate at astrophysical temperatures can be discerned, as described in section 1.2.

4.3.1 Beam Normalization

The method used for the purposes of normalizing the total beam intensity on target for the experiment described was based on that developed by D'Auria *et al.* [94]. It involved finding a normalization value relating the number of silicon detector triggers to the number of incident ions on target (R value) for a select group of *golden runs*. These must have had near constant beam intensity, coupled with consistent start and end FC readings to be classified as such. Defined more quantitatively, this required them to show no loss of silicon detector triggers and have the final FC4 current be within 5% of the first. Any runs with clear signs of Tail trigger spiking (see section 2.2.7 for an explanation of these terms), that being a temporary excessive number of events recorded at the Tail end of the DAQ, were also disregarded.

Once these golden runs had been identified, an R value was calculated by averaging the start and end FC4 readings to obtain an ion/sec beam intensity, which was subsequently multiplied by the total time of the run to get the total number of incident ions on target, once corrected for transmission through the target chamber (see appendix A for details on how this is calculated). The total number of peak silicon detector events were then divided by the integrated beam number to get the number of silicon detector scattering events per incident ion[3]. This value was calculated for each golden run, averaged, then used to calculate beam intensity for every other run based on its silicon detector peak total and pressure reading.

Despite only utilizing two different beam energies the author decided to separate the data into three separate groups, as two different separator tunes were used at the first energy. The

[3]Equivalent to the R value, once corrected for pressure changes, which was done linearly assuming the target is an ideal gas

Group	E_b (MeV/u)	ED2 (kV)	N_b	N_b(mc)
0	1.513±0.003	164.30	$6.59\pm0.21\times10^{14}$	6.37×10^{14}
1	1.513±0.003	164.65	$1.31\pm0.04\times10^{15}$	1.26×10^{15}
2	1.434±0.003	158.90	$4.31\pm0.14\times10^{15}$	4.03×10^{15}

TABLE 4.2: Total integrated beam on target (N_b) for the three separate recoil separator tunes. Three results from separate methods are displayed, those using FC4 (described in the text) and that utilizing the scattering simulation (mc), described in appendix F. E_b is the pre-target incident beam energy.

described method for beam normalization was used for all three groups, labelled 0, 1 and 2 in chronological order, with the total integrated beam for each given in table 4.2 for comparison.

4.3.2 Particle ID

Inspection of the online data revealed that the beam induced background was great enough that coincident gating on the BGO array was needed if genuine recoil events were to be discerned. Such recoil candidates were first identified during the online analysis due to the appearance of a cluster of events in the MCP vs separator TOF coincidence spectrum. Gating on this region showed that these events were consistent with a peak in the IC0+IC1 vs IC2+IC3 plot separated from the leaky beam locus (see figure 4.9), a trait indicative of recoil ions. Placing a graphical cut on the IC spectrum made the corresponding peak in the MCP vs separator TOF more apparent (figure 4.10).

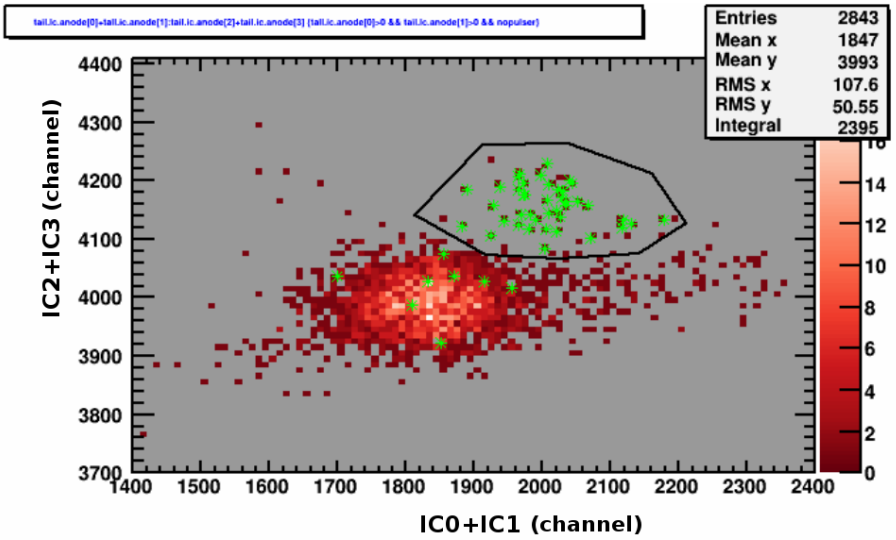

FIGURE 4.9: Online IC0+IC1 vs IC2+IC3 coincidence spectrum of the first few runs at this ED2 tune (164.30 kV). Green points are those corresponding to the separator TOF gate 1400→1500 ns, the location of the suspected recoil peak. The data displayed here forms part of the Group 0 data set.

As DRAGON filters beam from recoil using their mass to charge ratio, higher mass beams make the difference in ratio of the respective particles much smaller when considering (p,γ) or (α,γ) reactions. This inevitably results in a significantly higher leaky beam rate, which

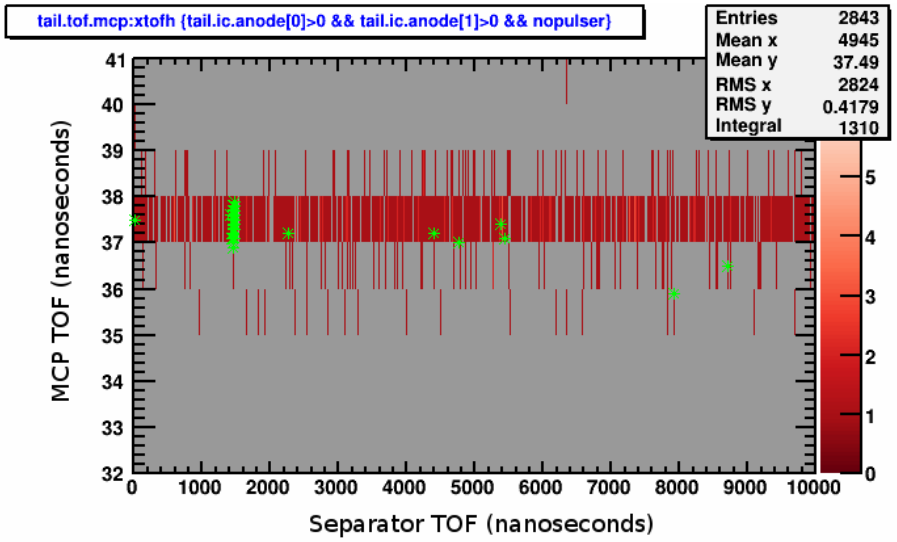

FIGURE 4.10: Online separator vs MCP TOF coincidence spectrum of the first few runs at this ED2 tune (164.30 kV). Green points are those corresponding to the graphical gate on the IC0+IC1 vs IC2+IC3 spectrum in figure 4.9. The data displayed here forms part of the Group 0 data set.

increased further when ED2 was increased from its initial 164.30 kV value to 164.65 kV, closer to the theoretical prediction.

In order to minimize background multiple variables were plotted against one another so that a region that gave recoil candidates the greatest spatial separation from leaky beam could be found. Ultimately the separator TOF vs IC_{tot} spectrum was chosen as the basis of PID for this reason, as can be seen in figure 4.11. The separator TOF is defined as the time difference between the BGO array and heavy ion detectors triggering, for a given event. A large region of interest (ROI) gate was placed on this spectrum to minimize false negative recoil events and a square shape was chosen so as to account for any possible correlation in the two plotted variables. Projection onto the IC_{tot} axis shows that the ROI gate contains a noticeable number leaky beam events however, as seen in figure 4.12. Although they are concentrated in the lower energy region, any cut placed here would inevitably cut out genuine recoil events due to the visible overlap of background with the recoil peak.

As the separator TOF is calculated based on the triggering of any heavy ion detector, including the MCP's, IC and target silicon detectors, an additional cut on the MCP TOF (the time difference between the two MCP's triggering) was also used for recoil selection. This was done to account for any background events triggering one of the heavy ion detectors which would generate a separator TOF if coincident with a BGO γ event, such an occurrence could potentially contribute to background in the recoil separator TOF region. The MCP TOF cut means that only events that trigger both MCP's in a timescale indicative of recoil ions (34→41 ns) will be selected, as shown in figure 4.13.

To try to better discern recoils from background, a series of IC spectra were produced, gated on the recoil ROI described above, with the three most enlightening shown in figure 4.14; events that appear in the cut from the separator TOF vs IC_{tot} plot (figure 4.11) are

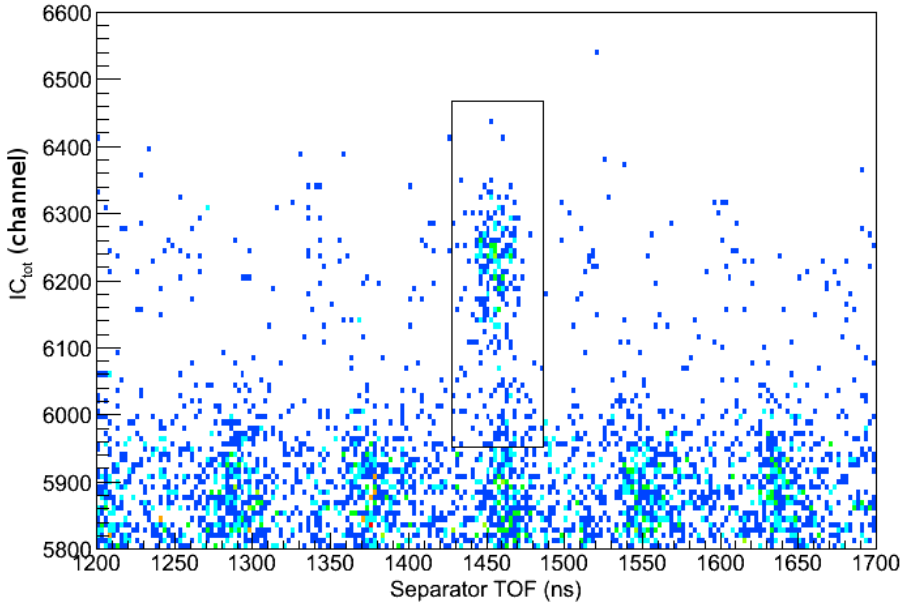

FIGURE 4.11: Plot used as the basis for particle ID; the rectangle shows the visual cut applied to recoil candidates. The data shown comes from Group 1 events which are at E_{cm}=5.76 MeV, with ED2=164.65 kV (see table 4.2).

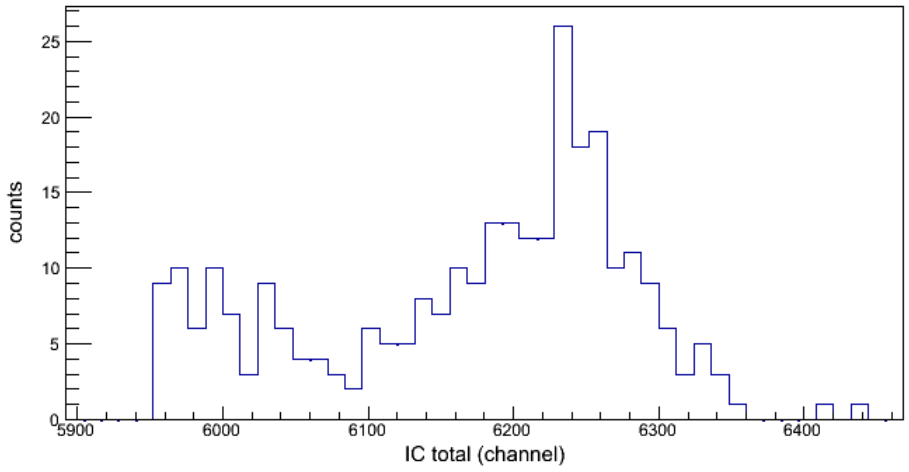

FIGURE 4.12: IC$_{tot}$ spectrum for the rectangular cut shown in figure 4.11. Leaky beam is clearly visible in the lower energy region.

shown as black stars. The recoil peak is again clear in these spectra, as is the location of background contamination, which is formed of two separate loci. This is most likely due to a neighbouring charge state passing through the separator; different charge states require different energies to traverse the separator (see section 2.2.4 for the equations that show this) so it is expected that they will manifest themselves as separate peaks in the ion chamber data. In the author's opinion placing a cut on these spectra requires some contemplation however. Made too small and the limits may cut out genuine recoil events that cannot be retrieved by subsequent analysis, the regions therefore must be large enough to include all such events.

This was done by fitting a Gaussian function to all events in the separator TOF vs IC$_{tot}$

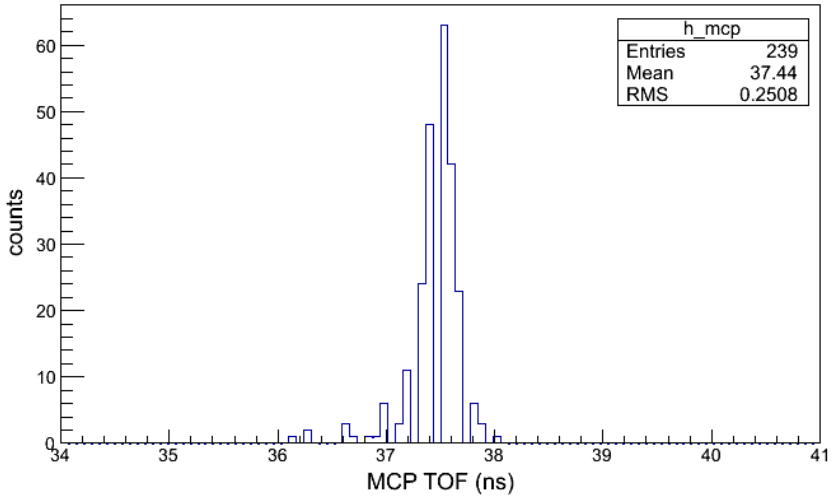

FIGURE 4.13: MCP TOF spectrum for the Group 1 data. The software cut applied to the recoil candidates is equal to the region displayed here.

plot cut (see figure 4.11), in order to approximate their distribution in the relevant spectra; circular cuts with a radius of 4.5 times these distribution's standard deviation were then constructed, as shown in figure 4.14. The author deemed these cuts large enough to include all recoil candidates yet constrained enough to remove a significant portion of the main background peak.

The separator TOF vs IC_{tot} spectrum is replotted, with the addition of the three described cuts, in figure 4.15. It is clear that there was a large decrease in the number of leaky beam events with the addition of the three IC cuts, however background contamination still remained and needed to be accounted for. Due to the nature of the beam buncher upstream from DRAGON however, background events did not have a completely random separator TOF; they appeared in packets separated with the inverse of the bunchers frequency, 84.8 ns[4]. To properly characterize the background the recoil cut was displaced along the TOF axis in periods of this magnitude, multiple times, and averaged to give the expected number of background events inside the cut $\langle N_b \rangle$.

This same technique, using IC cuts to remove background from the separator TOF vs IC_{tot} PID spectrum, was utilized for the Group 2 data; these had a slightly lower centre of mass energy and so the position of all the applied cuts had to be recalculated. The results are displayed in figures 4.16 and 4.17, the former of which are the IC spectra with the latter being the separator TOF vs IC_{tot} spectrum used to discern recoil events. Background from leaky beam was clearly more of an issue at this energy to such an extent that no reliable cut could be placed on the IC0 vs IC1 plot as the recoil peak was not well enough resolved. A peak in the separator TOF vs IC_{tot} spectrum was still visible however and so a reaction yield was calculable. As with the previous energy, a secondary leaky beam peak is visible in the ion chamber data and can even be seen in the TOF vs IC_{tot} spectrum (figure 4.17) in the form of periodic peaks around channel 5900 in the ion chamber.

[4]This effect is in fact visible upon closer inspection of figure 4.11

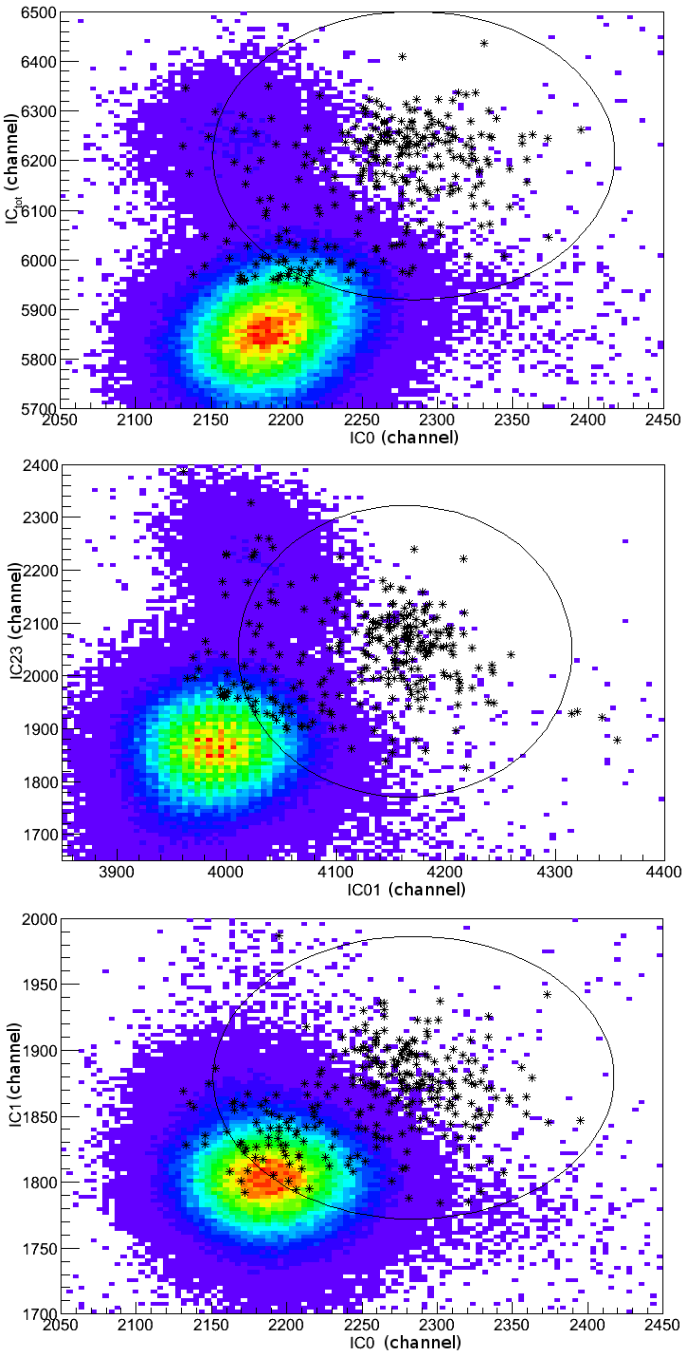

FIGURE 4.14: IC particle ID plots for the Group 1 data. Two separate leaky beam loci are visible in the top two spectra, most likely caused by multiple charge states traversing the separator. Events consistent with the cut on figure 4.11 are displayed as black stars. A generously large cut, shown as a black line, was placed on these spectra to reduce background whilst retaining all recoil events, see text for more details.

The total number of detected recoil events for each data set (N_r^{det}) was calculated by calculating the total number of events in the separator TOF vs IC$_{tot}$ spectrum ROI (N_{tot}) and then subtracting by the expected background $\langle N_b \rangle$. Table 4.3 gives all such numbers, and their associated uncertainty, for the three data sets. Note that the final recoil count has been corrected for the system live time when observing coincidence events, see section 2.2.7

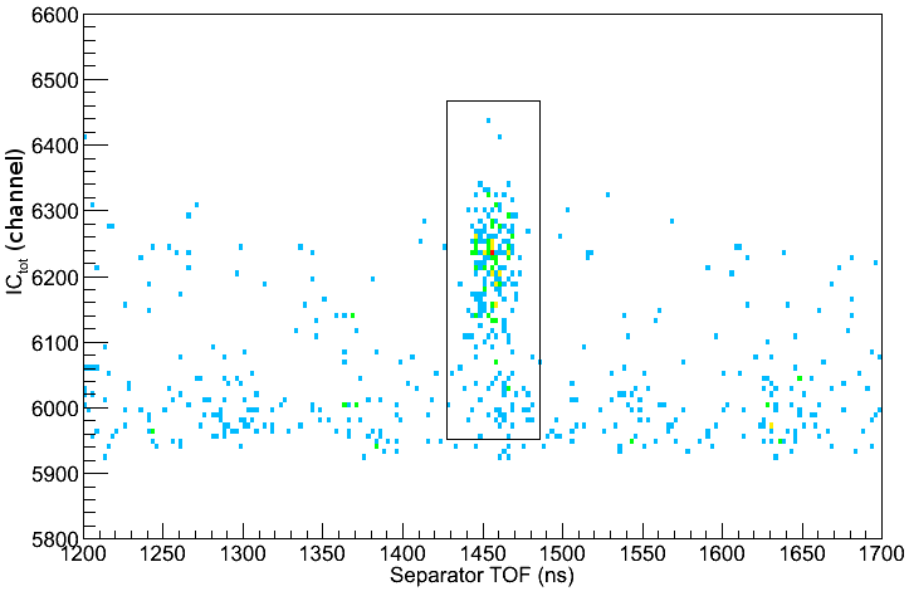

FIGURE 4.15: Particle ID plot with IC cuts added. There is a large decrease in background leaky beam when compared to the ungated spectrum in figure 4.11.

Group	N_{tot}	$\langle N_b \rangle$	LT (%)	N_r^{det}	ϵ_{IC} (%)	ϵ_{MCP} (%)
0	46±6.8	0.2±0.1	94.5	48.5±7.2	79.4±0.73	99.67±0.12
1	239±15	41.3±1.9	83.7	239.5±18.6	79.4±0.73	99.67±0.12
2	326±18	239.6±4.1	84.8	101.9±21.9	80.0±0.39	99.70±0.06

TABLE 4.3: Total number of events (N_{tot}), expected background $\langle N_b \rangle$, coincidence live time (LT) and expected number of recoil events (N_r^{det}, corrected for live time) for the three data sets. The relevant detection efficiencies (ϵ_{MCP} & ϵ_{IC}) are also shown.

for more details. Although the Group 0 and 1 data were analyzed separately, their final recoil count was combined (as they were both at the same beam energy) to give $N_r^{det} = 288 \pm 20$.

IC and MCP detection efficiencies for the recoil events were also calculated, based on the attenuated beam data, as described in appendix E. The same sized cuts were made as those used when discerning recoil events, but were re-positioned so as to cover the beam ion peaks in the spectra as shown in figures 4.18 and 4.19. Calculated efficiency values are given in table 4.3.

4.3.3 Charge State Distribution Measurements

As only one recoil charge state may be transmitted through DRAGON's separator for a given run, it is necessary to calculate what fraction of all recoil ions produced have such a charge immediately before they enter MD1. As an ion's charge state distribution in a medium is dominated by its atomic number and velocity[5], different recoil isotopes provide an acceptable surrogate for the charge state abundance of the ^{80}Kr ions produced in the reaction. As ^{83}Kr was more readily available at the ion source than ^{80}Kr, the former was

[5]For this reason ion energies in this section are given, and extrapolation done, in terms of MeV/u which is proportional to velocity squared.

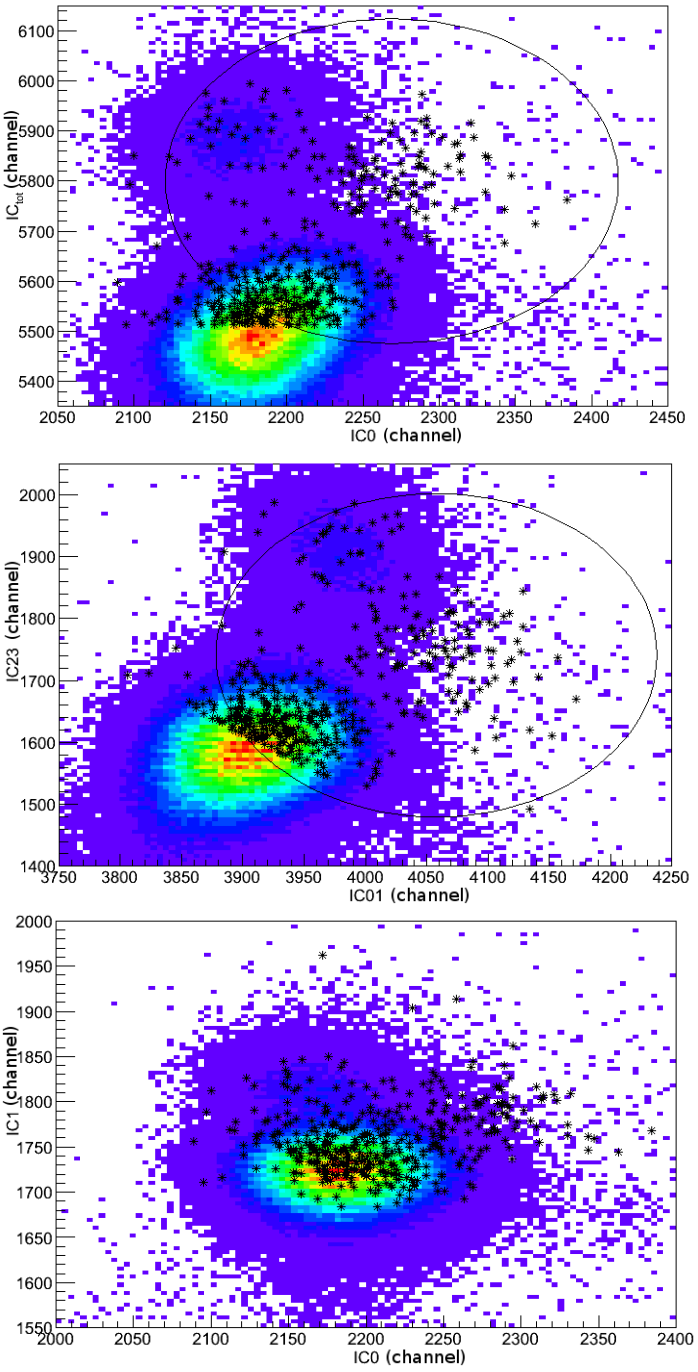

FIGURE 4.16: Same plots as figure 4.14 but with the Group 2 data (E_{cm}=5.45 MeV). The recoil peak is barely discernible in the IC0 vs IC1 spectrum and thus no cut was made on it.

used for the subsequent charge state measurements. Beam was delivered to DRAGON in the 14^+ charge state with post-target and post-foil charge state distributions observed at five different energies[6], in the 25+ charge state (corresponding to the charge state used for observing recoils in the experiment) using the method outlined in appendix C. The target gas pressure and aluminium foil thickness were consistent with those used in the radiative capture run. Such a large recoil energy range was used so as to cover the region corresponding

[6]Corresponding to recoil energies of 1.067, 1.122, 1.196, 1.285 and 1.486 MeV/u.

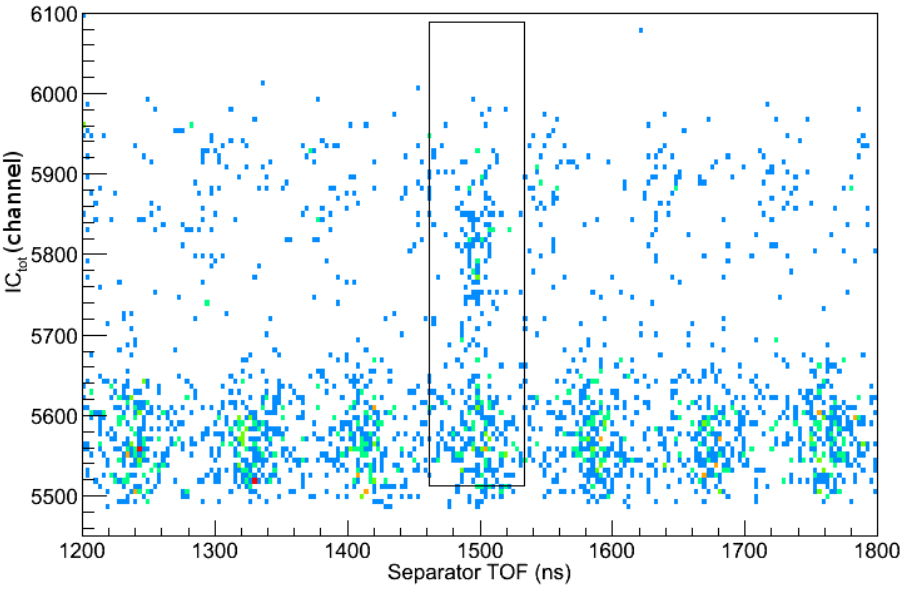

FIGURE 4.17: Particle ID plot with IC cuts from figure 4.16 added, for the Group 2 data. Periodic peaking in the ion chamber around channel 5900 can be seen, due to an additional leaky beam charge state traversing the separator.

Group	E_b (MeV/u)	E_{rec} (MeV/u)	ϵ_{CSD} (%)
0 & 1	1.513±0.003	1.290±0.007	2.11±0.06
2	1.434±0.003	1.220±0.007	1.63±0.06

TABLE 4.4: Table showing calculated charge state fractions (ϵ_{CSD}) for both post foil recoil energies (E_{rec}). Calculated pre-target beam energy (E_b) is also given.

to possible future measurements of the ^{76}Se(α,γ) cross section. The experimental data were fitted with a second order polynomial using the least squares method from both Minuit and Fumili. Both gave consistent fit parameters with figure 4.20 showing a graph of the resulting function, together with the experimental data.

Extrapolating the experimental data to the corresponding recoil energies was complicated by the presence of the charge state booster foils; ion energy loss through them could not be measured as the incident beam charge state was too low to be tuned through DRAGON. This meant that the pre-target beam energy had to be calculated using energy loss values obtained from the program SRIM [95]. As such calculations are based on extrapolations there is also a contribution to the uncertainty in estimated beam energy, in addition to uncertainty arising from the length of the target [31]. The former was estimated from comparisons of experimental data to those quoted by SRIM for a helium target, yielding a value of 6.9%. Once the beam energy was calculated, so too was the initial recoil energy and SRIM energy loss values were used to estimate post target and foil energy. These were subsequently used, together with the fitted charge state distribution data, to give a final recoil charge state abundance value for both beam energies, as shown in table 4.4. Uncertainty arising from the fit was taken to be the average displacement from the experimental points, weighted to the uncertainty on each data point.

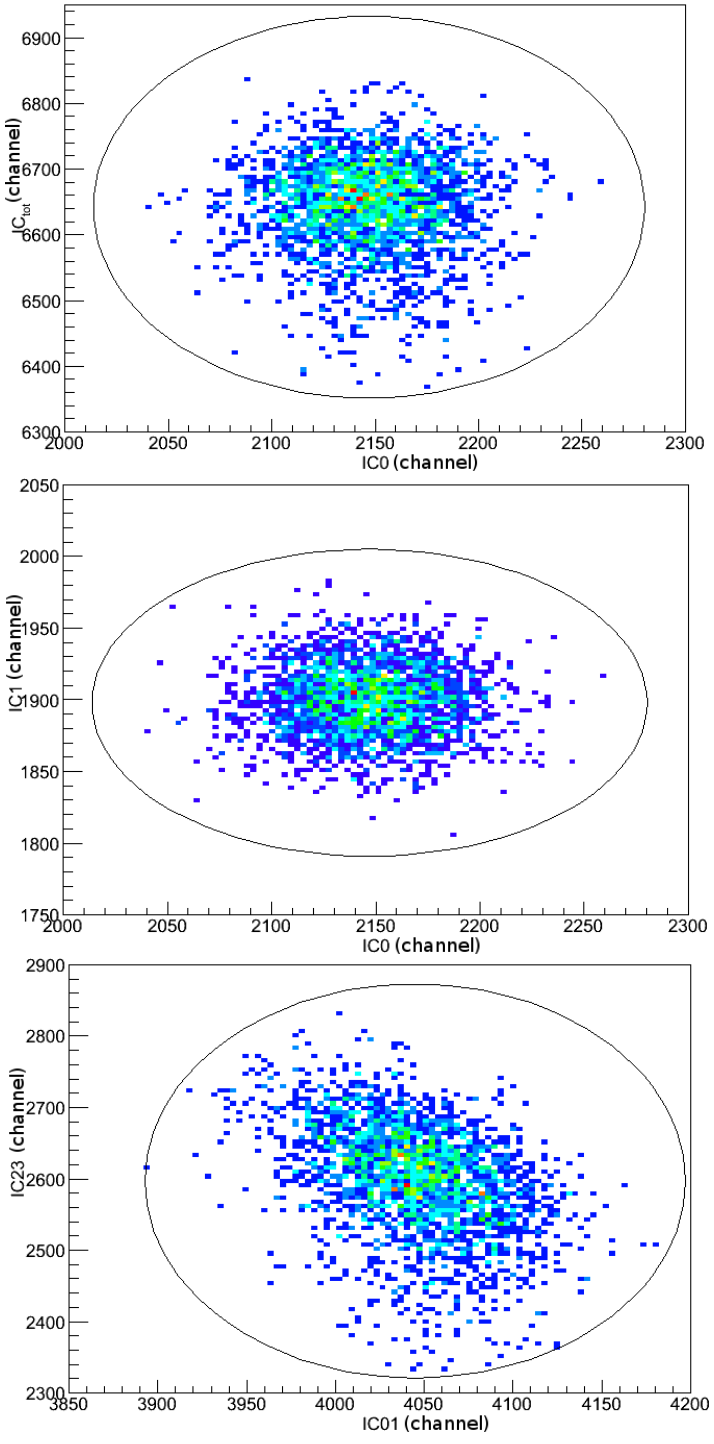

FIGURE 4.18: IC cuts used on the attenuated beam data when calculating the end detector efficiencies, for the Group0 and 1 energies.

4.3.4 BGO Efficiency

As a coincidence gate on the BGO array was used when discerning recoil events the corresponding detection efficiency is needed when calculating the final recoil yield. The level scheme of the compound nuclei (^{80}Kr) is what ultimately dictates the array's efficiency whilst not necessarily being the object of interest per se. Previous work characterizing the levels in

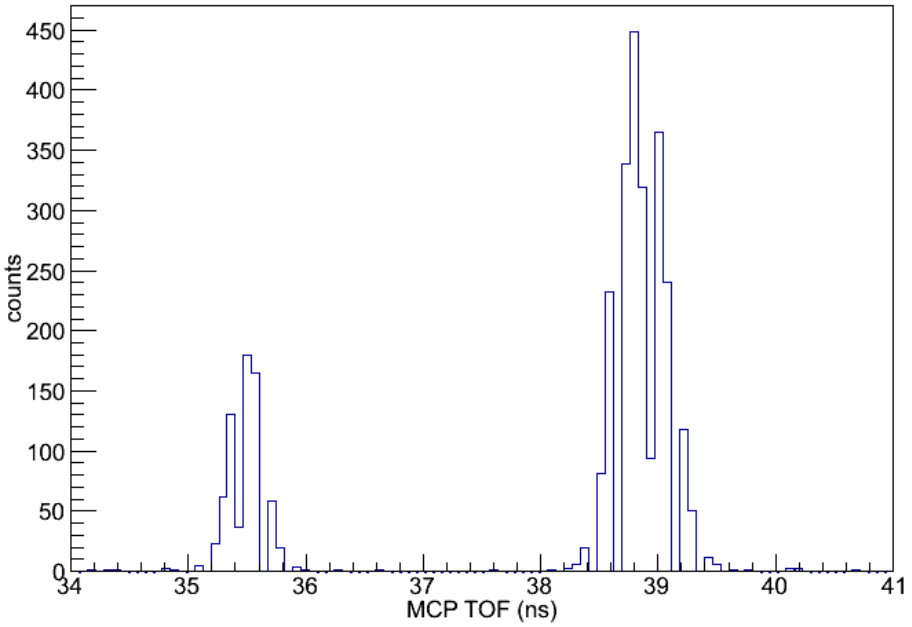

FIGURE 4.19: MCP TOF cut used on the attenuated beam data when calculating the end detector efficiencies, for the Group0 and 1 energies.

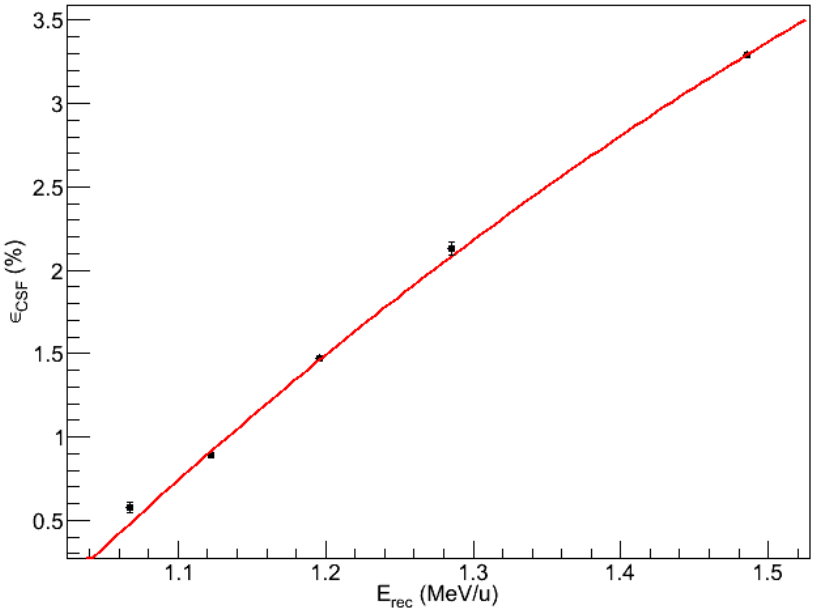

FIGURE 4.20: Measured charge state fractions of ^{83}Kr, in the 25+ charge state, for a variety of energies. A second order polynomial fit is shown in red.

this nucleus has been carried out [128] (as illustrated in figure 4.21), however, in the energy region corresponding to the current work (see table 4.5) only relatively few high spin states have been observed [129]. As such the precise decay scheme for the compound state is not known.

Calculating the BGO detection efficiency in the event of an unknown decay scheme for the recoil nuclei required treating it as a nuisance parameter. As such the BGO simulation

E_{cm} (MeV)	$E_x(^{80}\mathrm{Kr})$ (MeV)
5.677→5.749±0.012	10.742→10.814±0.012
5.379→5.451±0.012	10.444→10.516±0.012

TABLE 4.5: Calculated energy range in the target for the two beam energies. Note that the uncertainties represent the systematic error in the range's position, arising from energy loss calculations from SRIM [95].

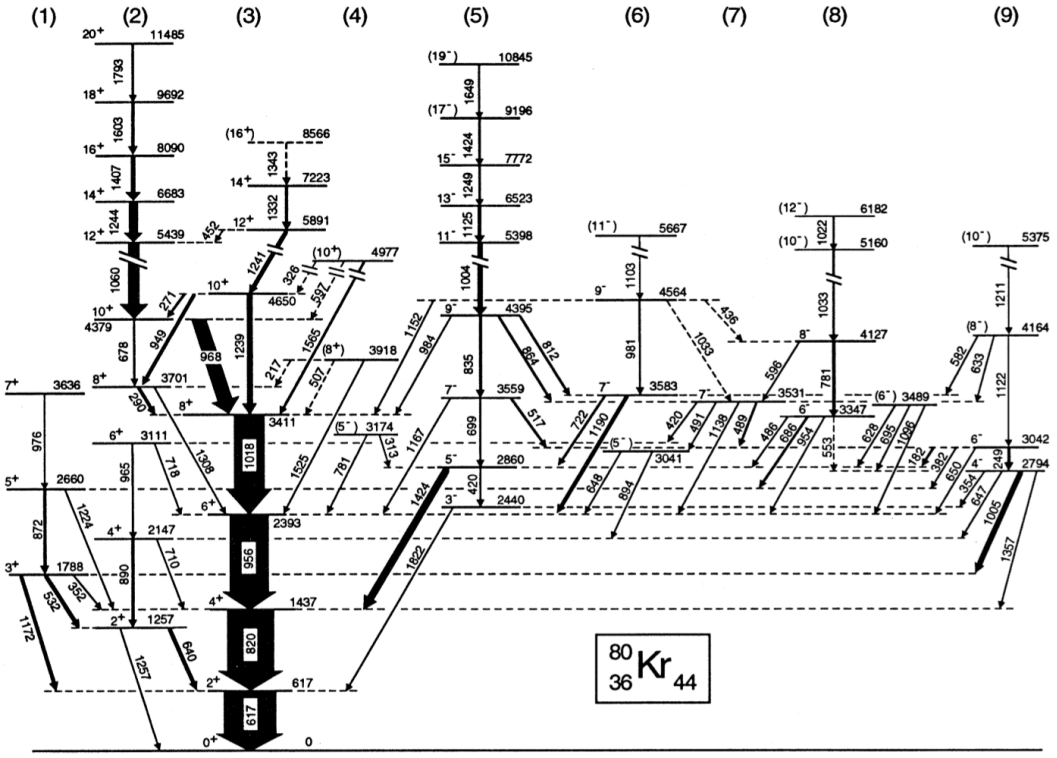

FIGURE 4.21: Observed level scheme for ^{80}Kr. Only high spin states were observed in the energy region corresponding to the current experiment. Taken from [129].

described in appendix I was used, with a multitude of possible γ cascade schemes, so that a suitable efficiency range could be discerned. This involved dividing the excitation level energy of the compound nucleus (^{80}Kr) into fifty equally spaced levels and generating a cascade for every branching scenario. Note that multiple branching from a single level was not included as this would have greatly increased the number of cascade possibilities whilst not enlarging the efficiency range.

The conditions of the simulation were set to mimic those from the experiment; specifically the BGO threshold was set to 1 MeV and γ events were generated randomly along the length of the target, which was assumed to be the case as no specific resonance is thought to dominate the cross section in the observed energy range. Also, all γ distributions were assumed to be isotropic. A total of 2754 unique cascade combinations were run, up to a multiplicity (number of gamma events for a single cascade) of five, giving a final efficiency range of 65→95%. The higher efficiencies correspond to cascades that result in many gamma events above the BGO threshold, and the lower efficiencies correspond to the case of just one gamma event above

threshold. The simulation was also run with cascades corresponding to the high spin bands observed in [129], giving efficiencies within the quoted range, although populating them with an alpha capture channel was unlikly.

With regards to the threshold, it was noted that there was a miscalibration observed in this energy range during the ^{60}Co source tests (see appendix I), and so the threshold used in the simulation was varied in both directions by 200 keV so as to account for this. This did not increase the range of possible efficiencies however. The quoted range therefore includes every feasible decay possibility and gives a total detection efficiency of 80±10%, which is the average of the range and the standard deviation of the population of possible values taken as the uncertainly, under the assumption all are equally likely. There is also a systematic uncertainty in the simulation however, as seen in appendix I. An estimate of this is taken to be 6%, which is the deviation of the simulation from the experimental data for total photopeak efficiency, when a ^{244}Cm^{13}C (6.13 MeV) source was placed inside the target. Combining this with the cascade uncertainty gives: ϵ_{BGO}=80±11%. The two beam energies populate an excitation region in ^{80}Kr close enough that their ϵ_{BGO} values can be considered consistent.

Chapter 5

Results and Discussion

In this chapter the results of the the two experiments presented in this thesis are presented and their implications discussed. It should be noted that the results and conclusion of the following section were previously published in the journal *Physics Review Letters* [45].

5.1 ^{18}F(p,γ)^{19}Ne

A resonance strength ($\omega\gamma$) of 29^{+69}_{-24} meV and a Γ_γ of 110^{+263}_{-93} meV was found (see section 1.2 for a discussion of how this is calculated), at the 95% confidence level, both of which are a factor of nine smaller than the previously assigned values. The 665 keV resonance's contribution to the total reaction rate was calculated, with both the previous and current results in order to fully comprehend the impact of the current study. Cross sections were calculated within an R-Matrix framework, including the external capture component and interference between resonances (see section 1.2.4 for a overview of this method). The program AZURE [130] provided a convenient, user friendly interface with which to conduct this work.

One complication with this method however, is the large number of experimental parameters needed. As discussed in section 3.1.3, there have been a number of studies characterizing the level scheme in the relevant region of ^{19}Ne, some of which have provided conflicting results. When coupled with the tentative nature of inferring resonance parameters from analogue assignments, as well as their relative phase, providing the R-Matrix formalism with a definite set of input parameters was problematic to say the least. Given this it seemed most sensible to consider the scenario that maximizes the 665 keV resonance's potential contribution to the total reaction rate, provided that it was plausible given the previous work, in order to fully appreciate the significance of the current study.

Parameters were taken from a variety of sources (see table 5.1 for a complete list) and the the 665 keV resonance was given a positive phase, relative to the other $3/2^+$ states in ^{19}Ne. The upper graph in figure 5.1 displays the 665 keV resonant contribution using the previous upper limit from Rehm *et al.* [60]. Although the 330 keV resonance (E_x=6.741 MeV) does dominate, only the Γ_p of the E_x=6.741 MeV state has been experimentally determined [78] and the model calculations are based on Γ_γ and Γ_α from an assumed analogue assignment [56]. Another state with the same J^π, but different width, does lie nearby so this assignment is by no means definitive, meaning that the 665 keV resonance could have played a major role in

E_x (MeV)	E_r (keV)	J^π	Γ_γ (eV)	Γ_p (keV)	Γ_α (keV)
6.289	-122	$^1/_2^+$ [83]	1	73.1 ($fm^{-1/2}$) [131]	11.62 [83]
6.419	8	$^3/_2^+$ [56]	0.77 [87]	7.19×10^{-39} [131]	0.5 [90]
6.437	26	$^1/_2^-$ [56]	1	1.1×10^{-20} [74]	220 [56]
6.449	38	$^3/_2^+$ [56]	1.1 [88]	1.17×10^{-15} [132]	4.0 [79]
6.698	287	$^5/_2^+$ [56]	0.29 [87]	1.2×10^{-5} [74]	1.2 [88]
6.741	330	$^3/_2^-$ [56]	5.0 [87]	2.2×10^{-3} [78]	5.2 [87]
6.861	450	$^7/_2^-$ [133]	2.4 [56]	1.6×10^{-5} [56]	3.10 [56]
7.070	665	$^3/_2^+$ [24]	1	15.2 [24]	23.8 [24]
7.238	827	$^3/_2^+$ [56]	1	0.35 [134]	6.0 [87]
7.253	842	$^1/_2^+$ [134]	1	0.2 [79]	23 [134]

TABLE 5.1: ^{19}Ne level scheme adopted for the R-Matrix calculation. Γ_γ widths set to 1 eV are assumed based purely on surrounding analogue states in ^{19}F.

this temperature range (0.1→0.4 GK). It can be clearly seen that, compared to the 330 keV resonance, only now can it be definitively shown that this resonance makes no significant contribution to the reaction rate at any temperature relevant to ONe novae [57].

In summary, the ^{18}F(p,γ)^{19}Ne resonance strength was been measured at the 665 keV resonance using the recoil mass separator DRAGON. Two ^{19}Ne recoil events were discerned with high confidence, resulting in a $\omega\gamma$ that is a factor of nine smaller than the previous assignment. As a consequence this resonance has now, for the first time, been shown experimentally to play a negligible role in the destruction of ^{18}F at temperatures associated with ONe novae, and thus does not influence the ^{18}F abundance after the resulting outburst. It is therefore now clear that it is crucial that either a direct measurement of the 330 keV resonance, or an indirect determination of the Γ_γ and Γ of the associated state, are made if future ^{18}F abundance observations are to be fully exploited.

5.2 ^{76}Se(α,γ)^{80}Kr

Experimental cross sections were calculated for the two separate energies, using the method outlined in section 1.2, and are displayed in table 5.2. Theoretical values were taken from the NON-SMOKER code [127] with ground state spins from [135], level densities from [99], particle potentials from [136–138], width fluctuation corrections from [139] and isospin suppression from [140]. The results are displayed in figure 5.2 and table 5.2. The published theoretical cross sections have associated theoretical masses from three different sources [141–143]; as the latter two gave near identical results only calculations using Möller *et al.* [141] and Pearson *et al.* [143] are shown however. Good agreement can be seen with the experimental data, the higher energy point agrees to within uncertainty and the lower energy point shows a two standard deviation separation, when using the Pearson *et al.* masses.

The data for the in beam study on ^{70}Ge by Fülöp *et al.* [108] is shown in figure 5.3. It can be seen that there is very good agreement with the NON-SMOKER calculations also, using the same settings as before with masses from Möller *et al.* [141]. This would suggest that the described settings are satisfactory for calculating alpha capture cross sections for the

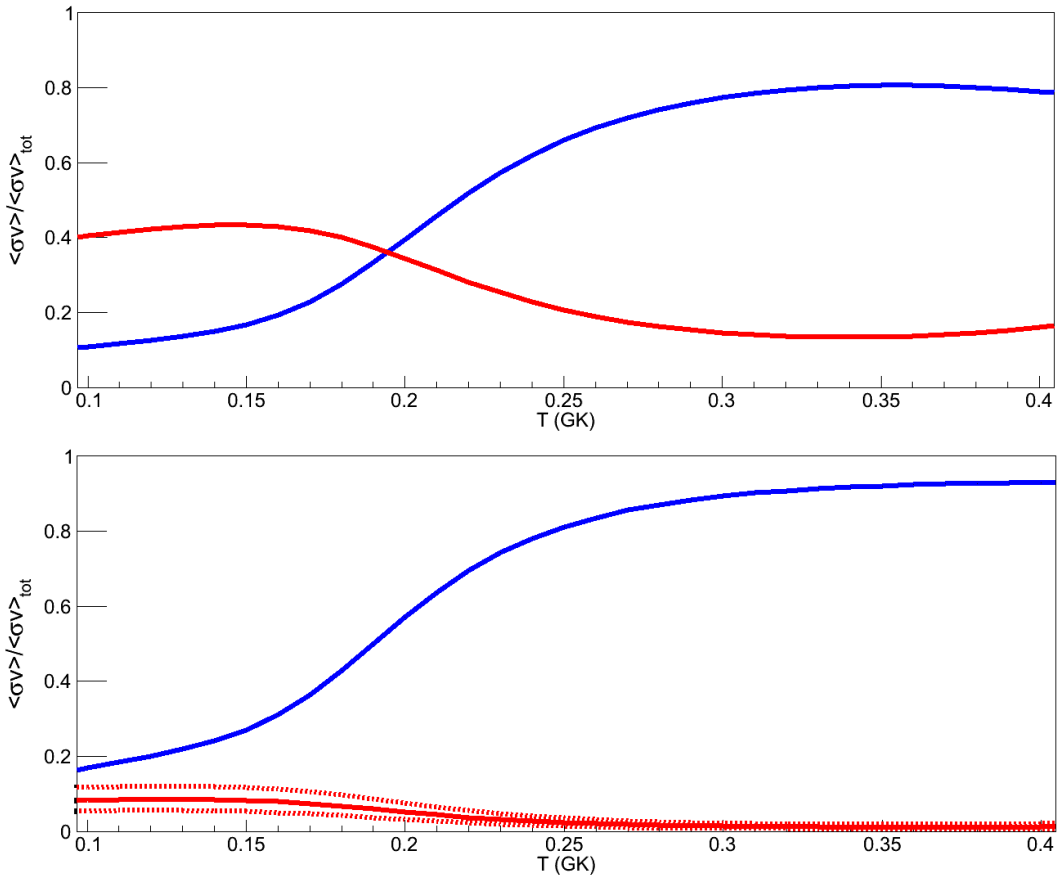

FIGURE 5.1: Fractional resonant and direct capture contributions to the total ^{18}F(p,γ)^{19}Ne reaction rate at ONe nova peak temperatures. The upper graph shows the 665 keV rate (red) using the experimental upper limit taken from Rehm *et al.* [60] whilst the lower graph has the rate using the current work, with dashed lines indicating the uncertainty when the Γ_γ width was varied at the 67% confidence level. The 330 keV resonance (blue) contribution was computed using data from [78, 83, 90]. Note that at lower temperatures the resonance at 38 keV together with a sub threshold state at -122 keV and the direct capture component account for the remaining contribution to the total rate [131].

p-process in the lower mass region, somewhat in contrast to the results of the higher mass studies. Here the NON-SMOKER code has been observed to both under [123, 144] and over predict [112, 113, 124, 125, 145, 146] the experimental cross section, although using different optical potentials has a large effect on the model's agreement. Further studies are still needed

E_b (MeV/u)	E_{cm} (MeV)	σ_{exp} (μb)	σ_{NS1} (μb)	σ_{NS2} (μb)
1.513±0.003	5.677→5.749±0.012	5.24±0.86	6.42	6.16
1.434±0.003	5.379→5.451±0.012	1.10±0.29	1.83	1.75

TABLE 5.2: Measured experimental cross sections (σ_{exp}) for the two beam energies (E_b) and the corresponding centre of mass energy range seen in the target (E_{cm}). The theoretical predictions, as given by the NON-SMOKER code (σ_{NS}), are also displayed (extrapolated from the data points given in [127]). The two theoretical values, σ_{NS1} and σ_{NS2}, use different theoretical masses, from [141] and [143] respectivly.

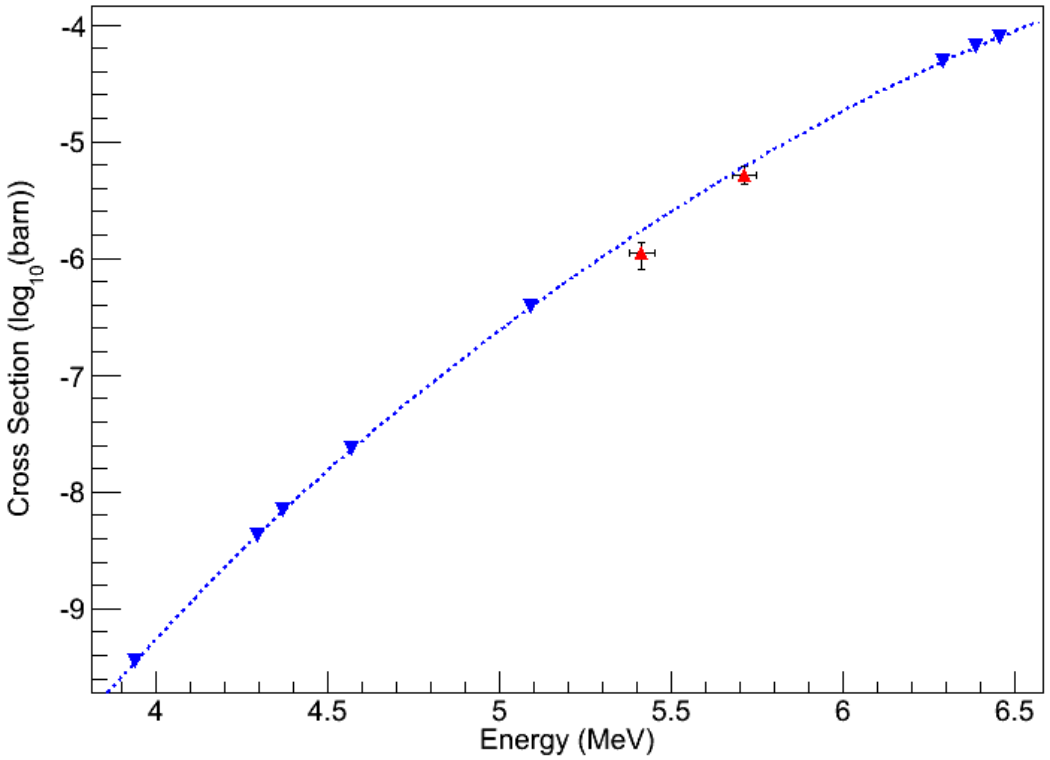

FIGURE 5.2: Measured experimental cross sections for the reaction ^{76}Se(α,γ) (red), compared with NON-SMOKER code results from [127] (blue). A polynomial extrapolation to the given theory data points is shown. Horizontal error bars indicate the energy region covered by the target. The astrophysically important region is 4.3→6.7 MeV.

though, due to the lack of experimental data available in both the low and high mass regions, so any conclusions remain tentative.

With regards to DRAGON's performance during the experiment, it is clear that there are issues with ED2's power supply, however in spite of this reliable data was still obtained. This strongly suggests that the facility can be used as an alternative to activation and in beam experiments with regards to measuring radiative capture reactions relevant to the γ-process.

In summary, the cross section of a high mass alpha capture reaction, relevant to the production of p-nuclei, has been successfully measured using a recoil mass separator for the first time. The results agree well with the NON-SMOKER prediction using default input parameters. In addition to this, it has been conclusively shown that DRAGON is capable of such high mass studies at astrophysical energies.

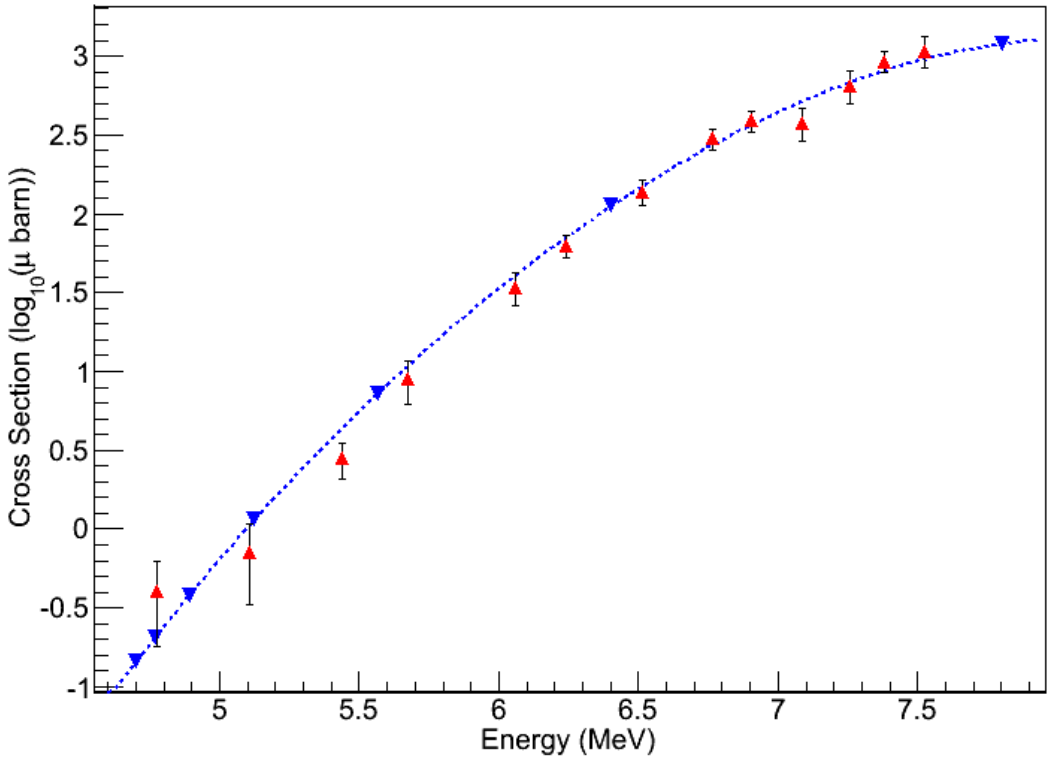

FIGURE 5.3: Measured experimental cross sections for the ^{70}Ge(α,γ) reaction from Fülöp *et al.* [108] (red), compared with NON-SMOKER code results from [127] (blue). A polynomial extrapolation to the given theory data points is shown.

Appendix A

Tuning DRAGON

The following gives a qualitative description of the procedure used to tune a beam through DRAGON and scale to recoils. It is included to illustrate the techniques and care taken to ensure that beam and recoil ions can be reliably transmitted to the end detectors. For a more specific description of individual steps and the user interface the reader is referred to `dragon.triumf/sep_tuning.html`.

Centring beam through the target

An optimal beam tune should be centred horizontally (in the direction perpendicular to the beamline) and vertically, in both position and direction throughout the target chamber. This is done so as to maximize ion transmission through the target cell and minimize spatial aberrations in beam composition; an important property needed for accurate beam energy measurements. A schematic of all the elements used in tuning DRAGON, as well as their names, is illustrated in figure A.1 and should be referred to by the reader for the following procedure:

- With gas removed, allow beam operators[1] to tune through to FC1 in order to maximize transmission through the target chamber.
- Refill the target with gas and adjust the MD1 field to centre the beam on the charge slits, which should be set to be just 2 mm apart in the x axis. Adjust the magnetometer until the NMR locks onto a specific field reading.
- Calculate the beam energy from the NMR reading, if it is not within user specifications ask the operators to re-tune and repeat the two previous steps.
- Insert the profile monitor and observe the location of the beam profile width and centroid position. Turn off Q1 and Q2, if the beam is properly centred then its profile will broaden but the centroid location should remain constant; if it shifts by more than 3 mm then ask the operators to re-tune and repeat this step. See figure A.2 for a screen shot of the profile monitor display.

[1] Not to be confused with the DRAGON operators, the beam operators control all tuning prior to FC4 and also have control of elements up to FC1.

- Also observe the charge-coupled device (CCD) image to ensure that the beam spot image does not shift by more than 10 pixels when Q1 and Q2 are turned off. See figure A.3 for an example of such an image.

Tuning beam from the charge slits to the mass slits

Tuning through the rest of DRAGON consists essentially of sequentially observing the beam position on a series of charge slits and beam current monitors, whilst utilizing the steering magnets and dipoles for alignment.

- The dipoles should now be scaled by a factor measured from a previously successful tune, whilst taking into account post target beam energy, mass and desired charge state; this is done on the "tune scaling" page[2]. Check that the beam is still centred on the charge slits, still set to 2 mm separation, if there is more current on one side than the other adjust the "energy" parameter of the "tune scaling" page.
- Put the beam current monitor 2 in (BCM2) and use steering magnet 1 (SM1) to centre the beam in both the x and y axis at this point.
- Retract BCM2 and open the mass slits, along the x axis, to a separation of 25 mm and look for current on FCM. If current is observed on one of the slits and not FCM adjust the ED1 voltage to minimize it.
- Progressively reduce the x separation in the mass slits whilst minimizing beam current on them by further adjustment of the ED1 voltage.
- Check the mass to charge ratio of the tune using the formula: $A/q = 2468(B^2)/V$. Any discrepancy greater than 0.5% of the expected value may indicate a problem with the ED power supply units[3].
- Open the x mass slits to 15 mm separation and close the y slits to 3 mm. Adjust the y axis steering magnets (SM1) to centre the beam on the y mass slits.

Tuning beam from the mass slits to the final slits

- Pull out FCM and insert BCM3. Adjust SM2 in both the x and y planes to centre the beam on BCM3, then retract the latter.
- Adjust the MD2 current such that the ratio of field strengths MD1/MD2, as measured by the NMR's is equal to 0.813.
- Insert BCM4 and adjust SM2 in the y plane for vertical centring; adjust the MD2 voltage for horizontal alignment then retract BCM4.
- Put in BCM5, adjust SM3 for alignment then retract BCM5.

[2]This software essentially just does calculations regarding what theoretical voltages should be applied to the dipoles for a given scenario.

[3]Such an issue was found and addressed in the ^{76}Se run, see chapter 4.2.

- Insert BCM6 and adjust SM3 in the y axis for centring then retract the former.
- Adjust the ED2 voltage to centre the beam on the final slits in the x axis, whilst closing the latter progressively to a width of 2 mm. Open the x slits to 45 mm and repeat the process for the y slits using SM4 instead of ED2.
- Compare FCCH, FCM and FCF to confirm that transmission is approximately 100%.

Tuning DRAGON to recoils

- Use the "tune scaling" page scale to scale the ED voltages by the beam to recoil mass ratio; MD field values should not change however.
- Beam current on FCF should be observed to drop below a measurable level and can be retracted such that recoil events can be transmitted to the end detectors.

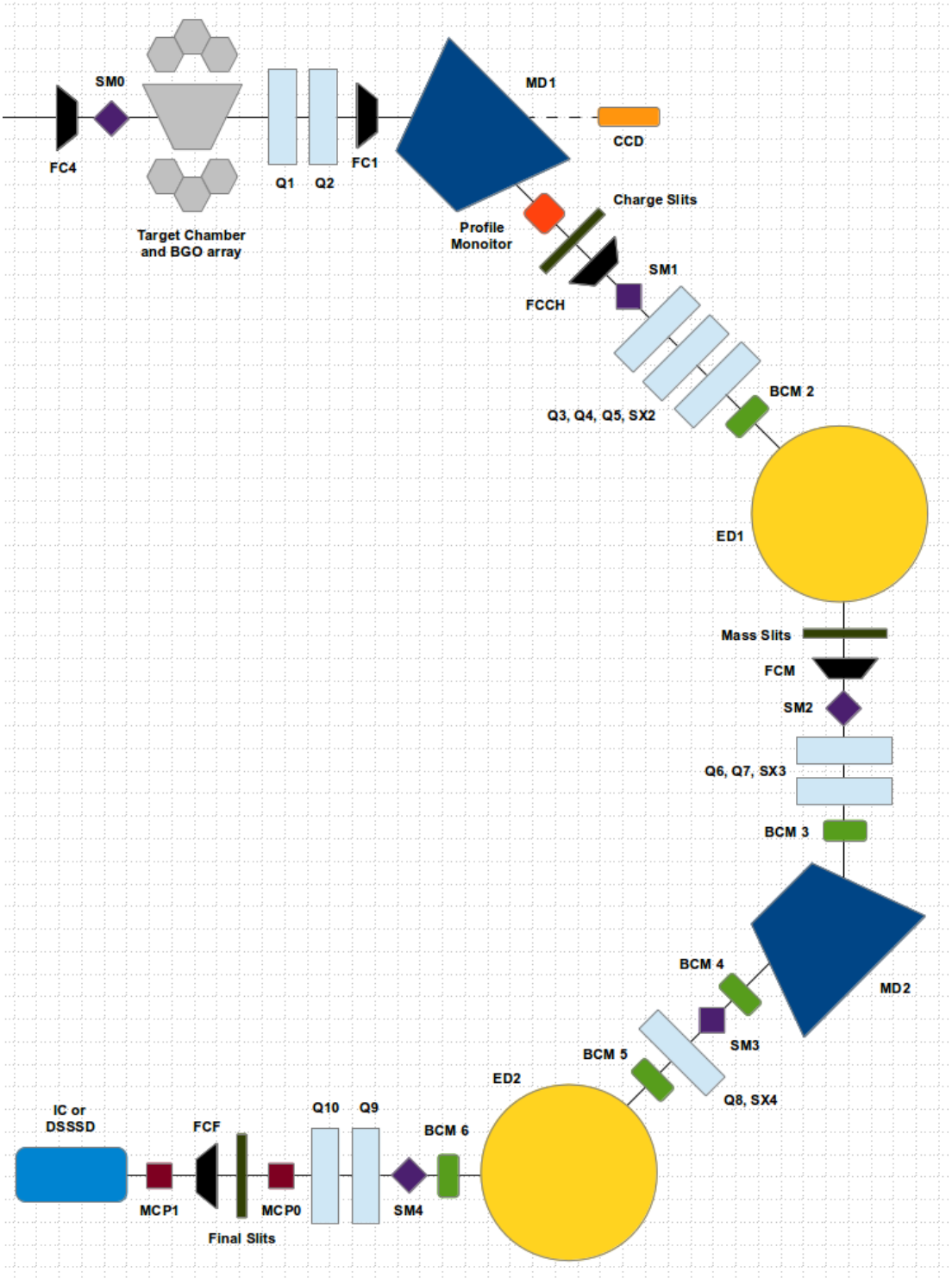

FIGURE A.1: Schematic showing all major components of DRAGON needed for beam tuning. Note that the size of each element and dipole bending angles are distorted for visual clarity.

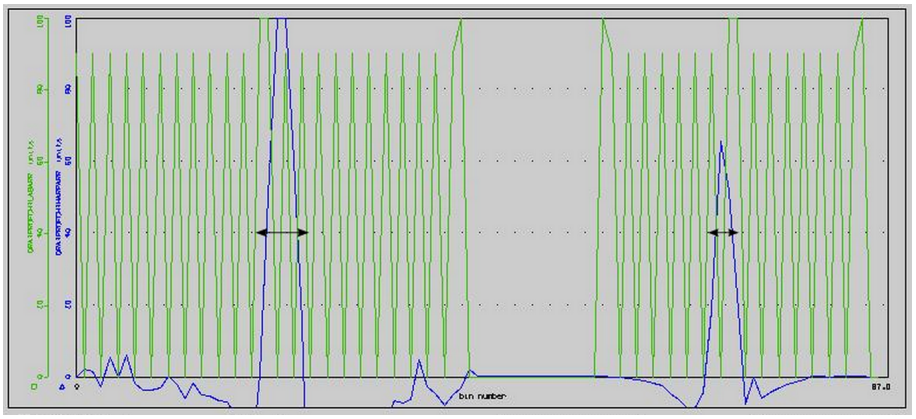

FIGURE A.2: Screenshot showing profile, in blue, of a well tuned beam with Q1 and Q2 on. Black arrows indicate the range of Q1 and Q2 off centroid shifts. As the separation between green peaks represents a distance of 1 mm this tune is within the 3 mm shift requirement.

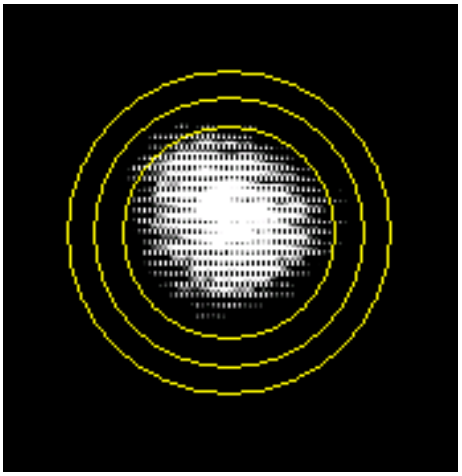

FIGURE A.3: Screen shot showing a CCD image of the beam spot.

Appendix B

Calibrating the BGO Array

In order for BGO thresholds to be set reliably, the detectors must first be energy calibrated. This is done with a 6.13 MeV $^{244}Cm^{13}C$ gamma source which is attached close to the centre of the array, usually in the gap between the top of the outer chamber and the crown detectors. Data from all 30 detectors is then acquired for a period of time sufficient for the 6.13 MeV peak to be discernible from the rest of the energy spectrum. The user then manually designates this peak (as shown in figure B.1) in every detector and the software re-calculates each bias voltage in such a way as to shift the peaks centroid into the expected position. This data acquisition and peak designation phase is then repeated, at least twice more, until the user is content that all 30 peaks centroids are at 6.13 MeV, although the poor energy resolution of scintillators prevents the accuracy of this method being much greater than ≈50 keV.

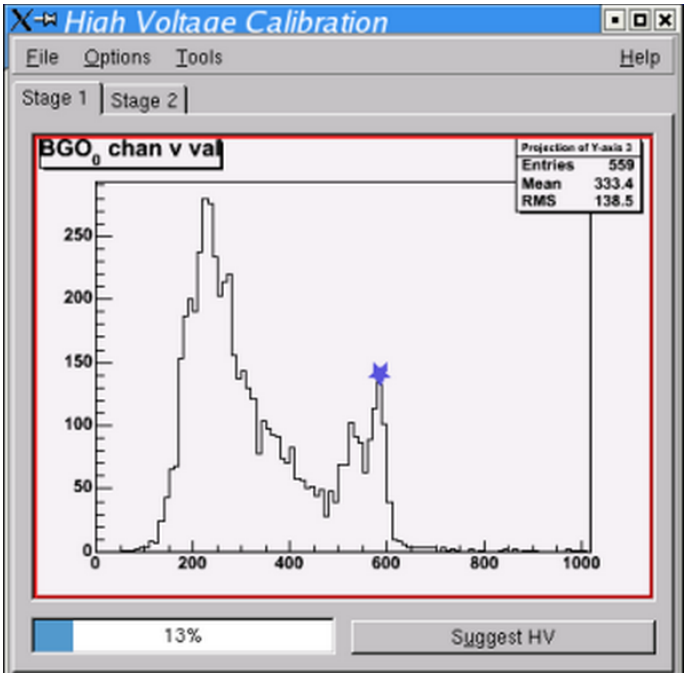

FIGURE B.1: Screen show illustrating user peak finding interface for the voltage calibration software.

Appendix C

Charge State Distribution Measurements

Calculations of experimental yields at DRAGON require accurate knowledge of recoil charge state distributions. These can be calculated using semi empirical equations, such as that outlined in Shu *et al.* [89], however experimental measurements are always more desirable and reliable. Often the exact nuclei of interest is not available in beam form and so another isotope of the same element must be used instead; these are deemed acceptable surrogates as charge state distributions are dominated by the velocity and atomic number of the ion being observed.

Once beam has been successfully centred through the target, as described in appendix A, the ratio of FC1 to FC4 (see figure A.1 for the location of all Faraday cups) is taken as the transmission through the target, emptied of gas, and beam energy is measured. Next the target is refilled, preferably to the same pressure as that used when conducting the radiative capture measurement, and MD1 set to transmit a specific charge state. The FC4 to FCCH current ratio is then measured and can be used to calculate the relative intensity of the chosen charge state. Note that the FC4 and FCCH currents have to be divided by the charge state of the beam and that selected by MD1, respectively, in order to be normalized to particle per second intensity. FC4 current readings are repeated three times and the corresponding uncertainty given as the standard error in the mean, see section 2.3.1 for more details on this method.

This process is repeated for a selection of charge states including, and encompassing that selected for the radiative capture run, for a given incident beam energy. A Gaussian distribution is then fitted to the resulting spectrum and, provided the measurements were conducted successfully, the integral of the fitted function should equal unity, within uncertainty.

Appendix D

MCP Transmission Measurement

After the two experiments described in this thesis were conducted it was found that the MCP transmission efficiency was in fact lower than previously measured by Vockenhuber *et al.* [147]. This was due to the support wires on the carbon foils being thicker than anticipated as a result of the manufacturer sending us the wrong type; as such the transmission quoted in the ^{18}F(p,γ)^{19}Ne paper [45] was erroneous and had to be re measured. This was done in April 2014 using a 1.12 MeV/u ^{15}N beam, which was attenuated and transmitted through the separator and into the end detectors. A double sided silicon strip detector (DSSSD) was positioned after the MCP's and a series of runs were taken with the support wires in place and then retracted, alternatively. By observing the number of events incident on the DSSSD with the wires in place and dividing it by the number when retracted one can calculate the corresponding transmission efficiency, consistent with the method outlined in [147]. Twenty nine such transmission calculations were done and averaged, yielding ϵ_{MCP}^{trans}=66.5±2.2%. The uncertainty comes from the standard error in the mean for multiple measurements, as described in section 2.3.1.

Appendix E

Heavy Ion Detector Efficiencies

We can define the efficiencies ϵ for both the IC and MCP's as:

$$N_{IC} = \epsilon_{IC} N_{tot} \tag{E.1}$$

$$N_{MCP} = \epsilon_{MCP} N_{tot} \tag{E.2}$$

respectively, where N_{IC} and N_{MCP} are the total counts in the respective detectors. However we also need the total number of incident ion particles N_{tot}, which we don't know as a beam intense enough to measure on the FC's would damage the end detectors, therefore a third measurement is needed in order for the efficiencies to be calculated:

$$N_{MCP\&IC} = \epsilon_{MCP} \epsilon_{IC} N_{tot} \tag{E.3}$$

Where $N_{MCP\&IC}$ are events that trigger both the MCP and IC detectors. Dividing equation E.3 by equation E.1 yields:

$$\epsilon_{MCP} = \frac{N_{MCP\&IC}}{N_{IC}} \tag{E.4}$$

and dividing equation E.3 by equation E.2 gives:

$$\epsilon_{IC} = \frac{N_{MCP\&IC}}{N_{MCP}} \tag{E.5}$$

As is often the case with DRAGON data analysis, cuts are made on the MCP and IC spectra in order to reduce the presence of background events. In this scenario N_{MCP}, N_{IC} and $N_{MCP\&IC}$ must be limited to those events that pass through the software gates imposed on the relevant detectors. For example if a cut of IC0=1000→1500 is used for event analysis, then N_{IC} and $N_{MCP\&IC}$ should include only those events that lie within this region. N_{MCP} will not be affected as no cut is made on this detectors spectra however.

Due to the typically low recoil yields present in astrophysical reactions there are frequently not enough good recoil candidates to sufficiently constrain the detector efficiencies. In this case attenuated beam is used as surrogate data, with care taken to account for the difference in energy and mass. This is done by re-positioning the software cuts to align with the attenuated

beam data.

Such efficiency calculations can be modelled as a series of trials, equal to either N_{MCP} or N_{IC} depending on which detector's spectra is being analyzed, and so the resulting uncertainty is governed by binomial, rather than Poisson or Gaussian statistics. The corresponding uncertainty is then:

$$\sigma_{IC} = \sqrt{N_{MCP}\epsilon_{IC}(1-\epsilon_{IC})} \tag{E.6}$$

for N_{IC}, and:

$$\sigma_{MCP} = \sqrt{N_{IC}\epsilon_{MCP}(1-\epsilon_{MCP})} \tag{E.7}$$

for N_{MCP}.

Appendix F

Elastic Scattering Simulation

The monte carlo simulation described in chapter 3 was initially constructed in order to facilitate beam normalization without the need for Faraday cup readings by monitoring the rate of elastic scattering. As the level of detail and scope of the simulation increased it was subsequently used to estimate detection rate for proposed experiments and for direct measurement of partial widths. It was written by the author in C++, allowing for its later integration with Geant4 libaries. The program reads in differential cross section data, in the centre of mass frame of reference, for a range of energies and angles, utilizing it to calculate how many scattering events will be detected per incident ion (defined here as the scattering yield) for a given detector geometry. When compared to the experimental spectra this yield can be converted to a value corresponding to the total number of incident beam particles on target, independent of Faraday cup readings. Beam properties such as diffuseness[1], relative position, angle and energy can also be modelled whilst energy and angular straggling of the recoil particle is handled by the Geant libaries.

In order to optimize efficiency the user enters constraints on certain parameters that limit the number of scattering events the program has to generate. For example if the detector is located at an angle of 35 degrees to the beam axis it makes little sense to calculate the number of scatting events that lie far outside this value and generate them as they have no realistic chance of being observed. Consequently the polar and azimuthal angle of generated events are constrained to a given range ($\Delta\theta$ and $\Delta\phi$ respectively). Another parameter constrained is the length of the beam axis in which scattering events originate as, due to collimation, only a small fraction of the targets total length is visible to each detector.

The first stage in generating the scattering yield involves calculating the total number of scattering events occurring within the constrained parameters which is done by profiling the beam energy through the target in the form of a root histogram. Incident beam energy, its diffuseness and subsequent energy loss are provided by the user. The range of beam energies (E) in the target together with the spatial length of the target are divided into a finite number of bins, (each denoted E_j and z_n respectively, having a width of dE and dz) in order to allow for histogram plotting. A Gaussian distributed beam energy probability density function (pdf) is then generated for each target and energy bin ($E_{pdf}(E_j, z_n)$), an example of which is

[1] Amount of spatial spread in beam intensity across the plane perpendicular to its direction

shown in figure F.1. The total beam energy probability density function for the beam energy across the whole target ($E_{pdf}(E_j)$) is extracted by summing each energy bin across the entire range of target length bins:

$$E_{pdf}(E_j) = \sum_{n=0}^{n_{max}} E_{pdf}(E_j, z_n) \tag{F.1}$$

Note that $E_{pdf}(E_j)$ is re-normalized to unity at the end of this procedure.

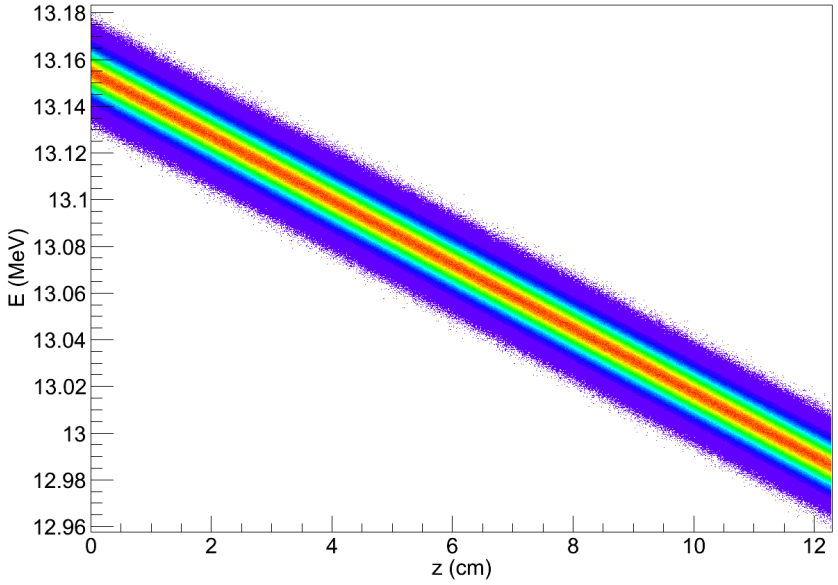

FIGURE F.1: A beam energy probability function through the length of the DRAGON target. Red indicates a higher probability density.

Now that the beam energy pdf has been constructed the next step is to fold this with the cross section data. Angular limits are also divided into a finite number of bins (each having a width of $d\theta$) which are used as the framework for a 2D histogram of the absolute scattering cross section for a given angle and energy bin pair, $\sigma(\theta_i,\ E_j)$. This is calculated from differential cross section data inputted by the user via:

$$\sigma(\theta_i, E_j) = \frac{d\sigma(\theta, E)}{d\Omega} \times sin(\theta) \times d\theta \times \Delta\phi \tag{F.2}$$

Here $\sigma(\theta_i,\ E_j)$ denotes the 2D bin value corresponding to the i^{th} bin of θ and the j^{th} bin of beam energy whilst $\frac{d\sigma}{d\Omega}$ is the differential cross section as a function of both polar angle and energy. The value of θ and E is determined from the centre of the bins θ_i and E_j. $d\theta$ is the size of the polar angular bins, not to be confused with the size of an infinitesimally small element, and $\Delta\phi$ is the total azimuthal angular range. The left hand side of this equation gives an absolute cross section for each angle and energy bin pair, numbered i and j respectively (an example of such a histogram is shown in figure F.2). This allows us to infer the absolute probability of a scattering event occurring, given quantitatively as:

$$P_{scat}(E_j) = \sigma(E_j) \times E_{pdf}(E_j) \times \frac{N_t}{A} \tag{F.3}$$

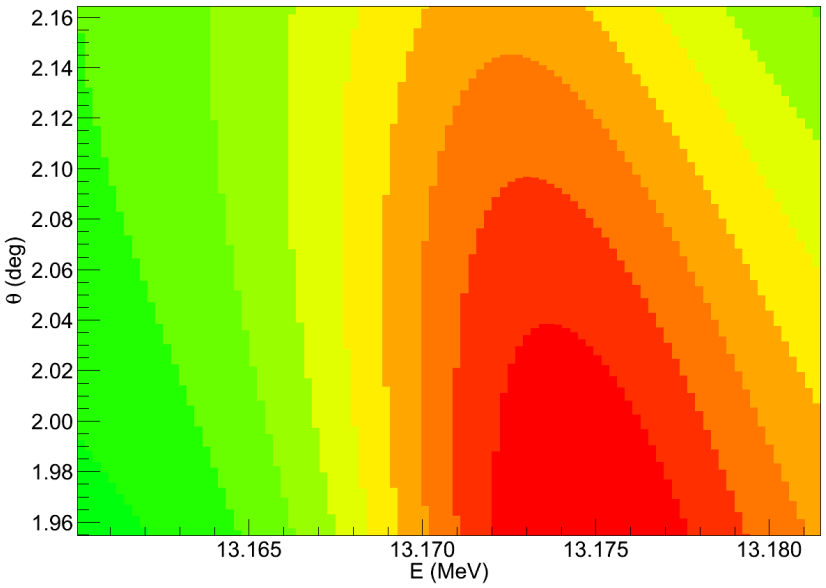

FIGURE F.2: Histogram of $\sigma(\theta_i, E_j)$, red indicates a higher cross section.

Here $P_{scat}(E_j)$ is defined as the expected number of scattering events occurring at a specific energy per incident ion on target. The number of scattering events is also constrained to those occurring within the angular and spatial user limits, as a consequence $\sigma(E_j)$ can be calculated:

$$\sigma(E_j) = \sum_{i=\theta_{min}}^{\theta_{max}} \sigma(E_j, \theta_i) \tag{F.4}$$

such that the energy is held constant whilst summing all the cross sections within the angular range. Once the histogram of absolute probability of scattering as a function of beam energy has been constructed it is used to calculate the total number of scattering events that will occur within the user limits. This is done by performing the sum:

$$N_{scat} = \sum_{j=E_{min}}^{E_{max}} P_{scat}(E_j) \times N_{beam} \tag{F.5}$$

Where the number of incident beam ions (N_{beam}) is another user defined input used to control the simulation's length of execution and precision.

Once the total number of scattering events is calculated the simulation proceeds to generate this number of events, individually and consecutively, within the user specified geometry. The $P_{scat}(E_j)$ histogram is used to generate a randomly weighted centre of mass energy for every event and the $E_{pdf}(E, z)$ histogram is then subsequently used to generate a randomly weighted position along the beam axis for this event to originate. This is done by projecting the histogram along the beam axis for the energy bin (E_j) generated from $P_{scat}(E_j)$, a process is shown schematically in figure F.3.

A randomly weighted value for θ is also generated in much the same way, but by projecting the $\sigma(\theta_i, E_j)$ histogram along the angular axis, as illustrated in figure F.4. As θ is in the centre of mass frame a conversion to the relevant laboratory value is done together with

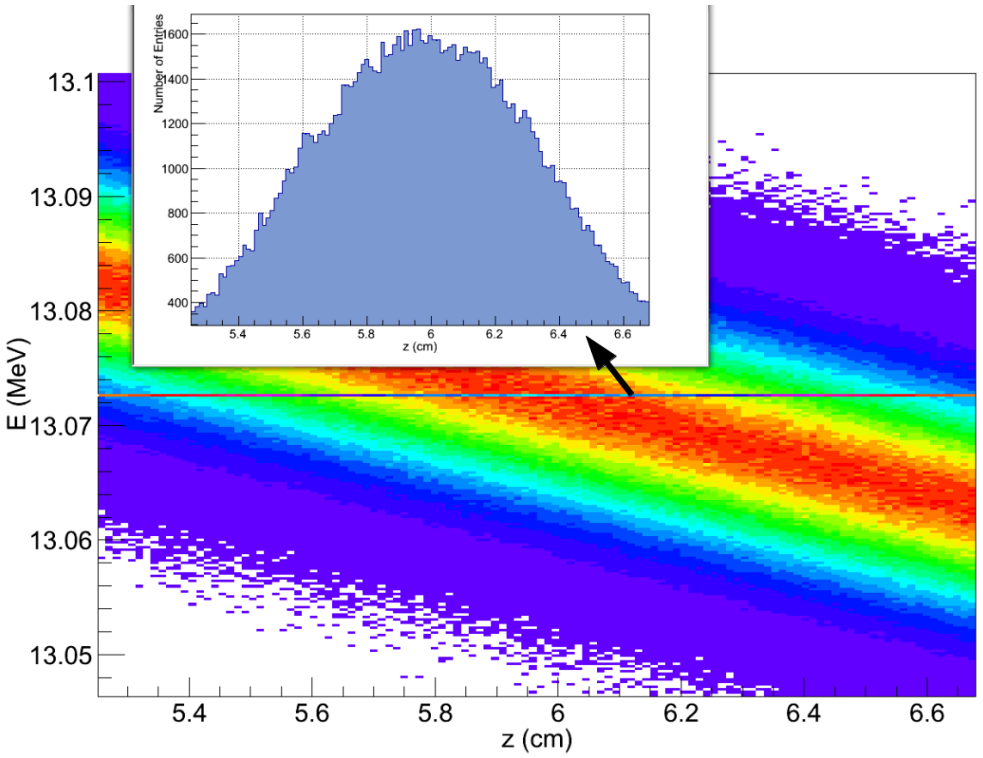

FIGURE F.3: A randomly weighted value for z is generated from a one energy bin projection of the $E_{pdf}(z, E)$ histogram along the z axis.

further kinematic calculations which are required to extract the recoil's kinetic energy, such derivations are given in appendix G.

Once the position, energy and direction of the recoil event have been ascertained they are used within the Geant framework to generate and track such an occurrence. Any event hitting a detector is recorded allowing the user to determine how many scattering events to expect for a given number of beam ions on target. This number can then be compared to experimental spectra allowing the relevant beam intensity to be inferred accordingly.

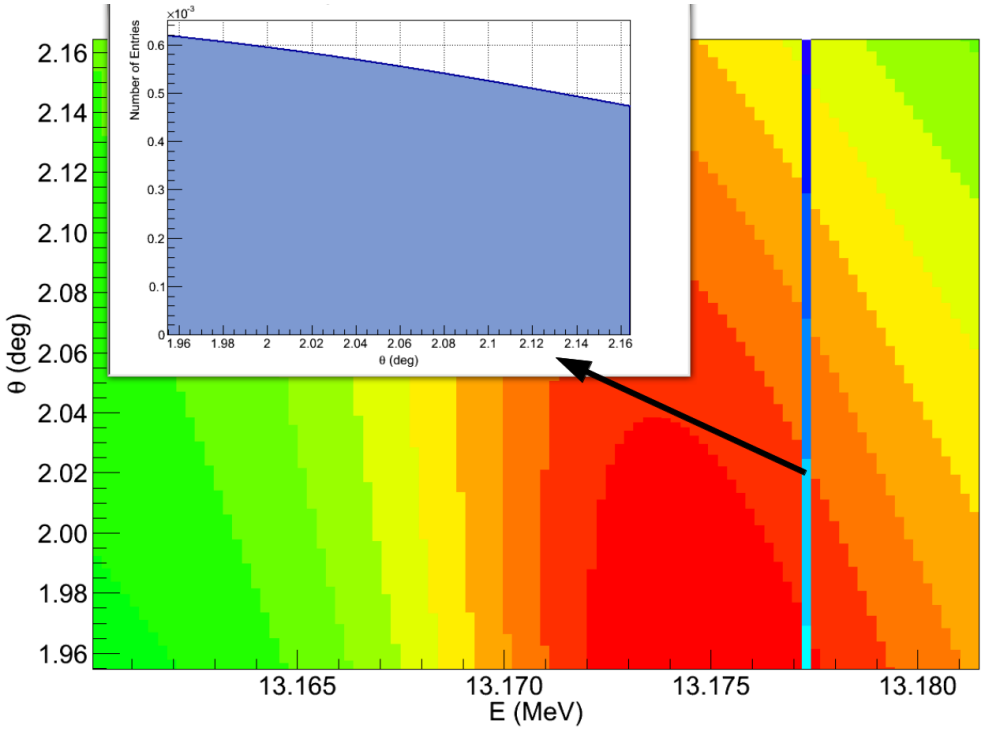

FIGURE F.4: A randomly weighted value for θ is generated from a one energy bin projection of the $\sigma(\theta_i, E_j)$ histogram along the angular axis.

Appendix G

Elastic Scattering Kinematics

When performing calculations involving elastic scattering in the laboratory frame we must also consider the centre of mass system as cross sections are usually quoted in such a format. Conversion between frames of reference can be done using the fact that total energy and momentum are always conserved. For the case of elastic scattering in the laboratory we have a beam particle (a) incident on a stationary target (A) with the former scattering off, due to Coulomb repulsion, at an angle θ and the latter at an angle ϕ. The beam ion subsequently becomes the ejectile (b) and the target nuclei becomes the recoil (B). Figure G.1 gives a visual outline of the situation.

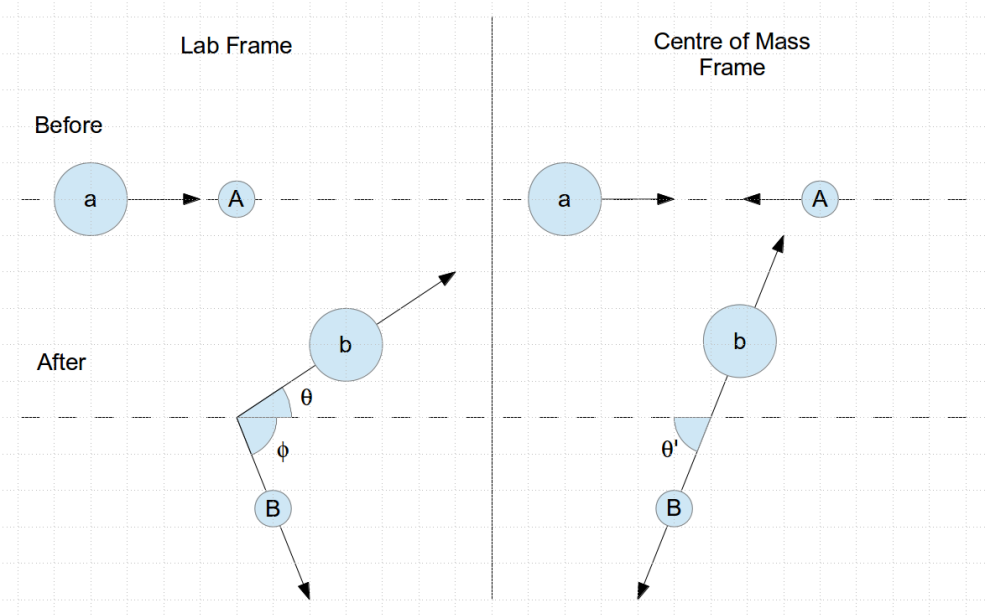

FIGURE G.1: Illustration of elastic scattering in both the laboratory and centre of mass frame of reference.

The monte carlo scattering simulation described in appendix F generates a centre of mass angle (θ') for each scattering event. In order to translate this into a laboratory energy (E_B) and angle (ϕ) for the recoil particle we must first consider just the energetics of the reaction:

$$E_a = E_b + E_B \tag{G.1}$$

With m the particle's mass and E their respective kinetic energy; subscripts classify each particle as outlined above. Next we examine linear momentum along the beam axis by considering the total before and after the interaction:

$$\sqrt{2m_aE_a} = \sqrt{2m_BE_B}\cos\phi + \sqrt{2m_bE_b}\cos\theta \tag{G.2}$$

Doing the same in the vertical axis gives us:

$$\sqrt{2m_BE_B}\sin\phi = \sqrt{2m_bE_b}\sin\theta \tag{G.3}$$

Combining these three equations leads us to:

$$E_b = \left(r \pm \sqrt{r^2 + s}\right)^2 \tag{G.4}$$

Where r and s are defined as:

$$r = \frac{\sqrt{m_am_bE_a}}{m_b + m_B}\cos\theta \tag{G.5}$$

and:

$$s = \frac{E_a(m_B - m_a)}{m_b + m_B} \tag{G.6}$$

The recoil's kinetic energy (E_B) can then be calculated for a given value of θ, provided we have knowledge of the beam particle's energy (E_a), from equation G.1 ($E_a = E_b + E_B$):

$$E_B = E_a - \left(r \pm \sqrt{r^2 + s}\right)^2 \tag{G.7}$$

This gives us a recoil kinetic energy for every laboratory scattering angle of the ejectile (θ), hence we now require conversion between the ejectile's laboratory angle (θ) and centre of mass angle (θ'). This can be achieved by first defining the centre of mass velocity (v_c) of the system:

$$(m_a + m_A)v_c = m_av_a \tag{G.8}$$

Which makes sense if we again consider conservation of linear momentum. After the collision we then have:

$$v_b'\cos\theta' = v_b\cos\theta - v_c \tag{G.9}$$

along the beam axis and:

$$v_b'\sin\theta' = v_b\sin\theta \tag{G.10}$$

along the axis perpendicular to the beam, where v'_b is the ejectile's velocity in the centre of mass frame. Also after the collision ejectile and recoil have equal and opposite momenta:

$$m_b v'_b = m_B v'_B \tag{G.11}$$

and their kinetic energies can be given as:

$$E'_b = \frac{1}{2} m_b (v'_b)^2 \tag{G.12}$$

$$E'_B = \frac{1}{2} m_B (v'_B)^2 \tag{G.13}$$

By combining equations G.9,G.10,G.11,G.12 and G.13, after much algebra we can arrive at:

$$\theta = \cos^{-1}\left(\frac{m_a/m_A + \cos\theta'}{\sqrt{1 + (m_a/m_A)^2 + 2(m_a/m_A)\cos\theta'}}\right) \tag{G.14}$$

A more rigorous derivation of this equation is given in [6]. The recoil's scattering angle in the laboratory frame (ϕ) can then be derived from equation G.3:

$$\phi = \sin^{-1}\left(\sqrt{\frac{m_b E_b}{m_B E_B}}\sin\theta\right) \tag{G.15}$$

As we have also previously derived values for both the ejectile (E_b) and recoil's kinetic energy (E_B), in equations G.4 and G.7 respectively, we can now generate a laboratory angle and kinetic energy for every centre of mass scattering angle generated by the monte carlo program.

One complication does arise, however, from the fact that equation G.4 ($\sqrt{E_b} = r \pm \sqrt{r^2 + s}$) has two real solutions, which converge at $\theta' = \pi/2$, then diverge. The situation is illustrated in figure G.2 where the green line represents the function resulting from the second term in equation G.4 being positive and the blue line is the negative subtraction case. This problem can be resolved by considering the physical implications of each case; at θ'=0, E_b can be equal to either the original beam energy (in this case 5.75 MeV) or a lower value. Observation of equation G.10 shows us that θ'=0 corresponds to θ=0 which is when the beam particle's trajectory is unaffected by the target nuclei's coulomb repulsion. Thus the beam ion must retain its initial energy and so the greater value is taken for E_b when $0 < \theta' \leq \pi/2$. The case when $\theta' = \pi$ corresponds to a head on collision between beam and target, basic intuition tells us that in this scenario the target recoil feels an impulse from the beam and carries away some of its kinetic energy and so E_b must be less than its initial value. Hence the lower of the two solutions is taken for when $\pi/2 < \theta' \leq \pi$ resulting in the red function as shown in figure G.2.

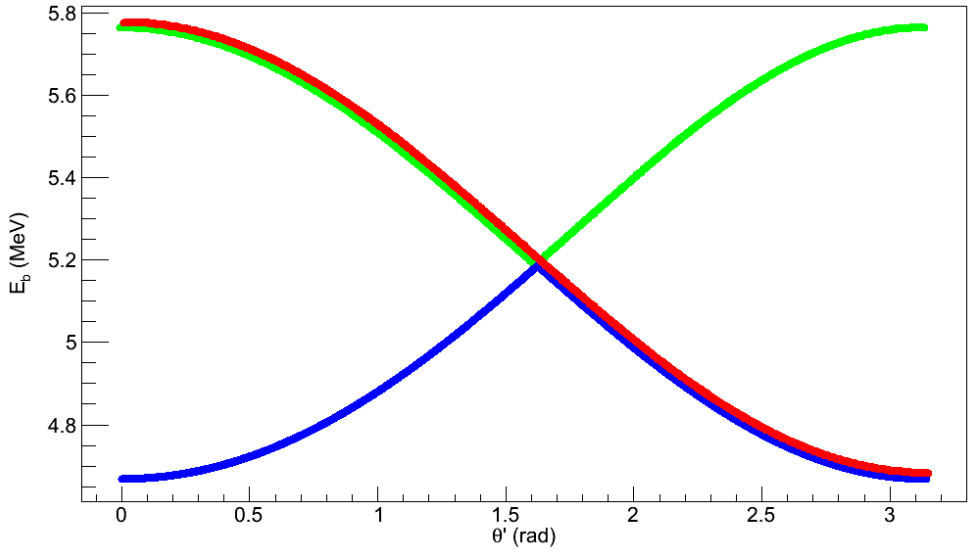

FIGURE G.2: The ejectile's laboratory energy (E_b) as a function of centre of mass scattering angle (θ') has two possible solutions, shown in green and blue, but only the combination shown in red is physically allowed. See text for more details.

Appendix H

^{18}F(p,γ)^{19}Ne Error Analysis

This section further outlines how the profile likelihood method from [43] (also see section 2.3.6) was used in determining the uncertainty in the resonance strength ($\omega\gamma$) for the 665 keV resonance in ^{18}F(p,γ)^{19}Ne. In implementing this method the experiment's data set was characterized in the form of a probability density function (pdf), consisting of three independent functions (X, Y, Z). These represent the random variables in our data: X forms the signal pdf, Y the background pdf and Z the detection efficiency pdf. The observed data can then be modelled as the product of these:

$$P(x, y, z|\mu, b, e) = X(\mu, b, e) \times Y(b) \times Z(e) \tag{H.1}$$

Here μ, b, e are the actual signal rate, background rate (in the signal region) and detection efficiency, respectively. Their observed counter parts are then: x, y, z, corresponding to the number of events in the signal region, number of events in the background region and measured efficiency of detection.

For the given experiment the signal rate pdf can be represented as a Poisson distribution as only two events were recorded:

$$X(\mu, b, e) = \frac{(e\mu + b)^x}{x!} e^{-(e\mu+b)} \tag{H.2}$$

The background pdf can also be modelled as Poisson as only three such events materialized in the relevant region during the run:

$$Y(b) = \frac{(\tau b)^y}{y!} e^{-\tau b} \tag{H.3}$$

Here τ is the probability of observing an event in the background region divided by the probability of observing an event in the signal region. In the given experiment this value was measured to be 8,000 from the attenuated beam MCP spectrum, meaning that there were 8,000 events in the region where the three background events appeared for every one in the region corresponding to the two ^{19}Ne counts.

The detection efficiency pdf is Gaussian in form as its expectation value is derived from a large sample of events:

Symbol	Definition	Measured value
ϵ_{MCP}^{trans}	MCP transmission efficiency	65.5±2.2%
N_b	Total number of beam ions on target	$9.9\pm1.8\times10^{11}$
ϵ_{CSF}	Charge state fraction efficiency	23.26±0.29%
ΔE	Energy loss across target	458±46 keV
Δx	Length of target	12.3±0.4 cm [31]
Γ	Width of resonance	39.0±1.2 keV [88]

TABLE H.1: List of all nuisance parameters in this experiment, together with their measured values.

$$Z(e) = e^{-\frac{1}{2}\left(\frac{z-e}{\sigma_e}\right)^2} \tag{H.4}$$

This pdf can be expanded to include all systematic uncertainties that arise from nuisance parameters when calculating the resonance strength based on an experimental yield. Such a calculation requires the use of equations 1.12[1] and 3.1[2]; and we can arrive at:

$$\omega\gamma = C\frac{N_r^{det}}{N_b\epsilon_{csf}}\frac{\Delta E}{\Delta x}\frac{1}{f(\Gamma,\Delta E)} \tag{H.5}$$

Where only variables with significant experimental uncertainties (>1%) are included, apart from C which is just a constant incorporating all other values; the function f represents both trigonometric terms from equation 1.12. All variables are defined, along with their measured values, in table H.1.

If we now consider all our nuisance parameters as a single term, θ, we can say:

$$\theta = \frac{1}{N_b\epsilon_{csf}}\frac{\Delta E}{\Delta x}\frac{1}{f(\Gamma,\Delta E)} \tag{H.6}$$

Assuming that all of the variables have uncorrelated uncertainties, then their total error is given by equation 2.18[3], and we have:

$$\sigma_\theta = \sqrt{\frac{\delta\theta}{\delta\epsilon_{MCP}}^2\sigma_{MCP}^2 + \frac{\delta\theta}{\delta N_b}^2\sigma_{N_b}^2 + \frac{\delta\theta}{\delta\epsilon_{CSF}}^2\sigma_{CSD}^2 + \frac{\delta\theta}{\delta\Delta E}^2\sigma_{\Delta E}^2 + \frac{\delta\theta}{\delta\Delta x}^2\sigma_{\Delta x}^2 + \frac{\delta\theta}{\delta\Gamma}^2\sigma_\Gamma^2} \tag{H.7}$$

After much algebra we arrive at a value of $\frac{\sigma_\theta}{\theta}$=19%. When considering equation H.4, we can say that e=1 and σ_e=0.19, when we calculate our confidence region for μ, making it equivalent to N_r^{det}.

The likelihood function for the data is given as:

$$L(\mu,b,e|x,y,z) = \prod_{i=1}^{n} P(x_i,y_i,z_i|\mu,b,e) \tag{H.8}$$

[1] $Y = \frac{\lambda^2(E_r)}{2\pi}\frac{\omega\gamma}{\epsilon(E_r)}\left[\arctan\left(\frac{E_0-E_r}{\Gamma/2}\right) - \arctan\left(\frac{E_0-E_r-\Delta E}{\Gamma/2}\right)\right]$

[2] $N_r^{tot} = \frac{N_r^{det}}{\epsilon_{BGO}\,\epsilon_{ERS}\,\epsilon_{CSD}\,\epsilon_{MCP}\,\epsilon_{det}\,\epsilon_{LT}}$

[3] $\sigma_f^2 = \left(\frac{df}{dx}\right)^2\sigma_x^2 + \left(\frac{df}{dy}\right)^2\sigma_y^2$

And as we only have one set of data, it follows that:

$$L(\mu, b, e|x, y, z) = \frac{(e\mu + b)^x}{x!} e^{-(e\mu+b)} \frac{(\tau b)^y}{y!} e^{-\tau b} e^{-\frac{1}{2}\left(\frac{z-e}{\sigma_e}\right)^2} \tag{H.9}$$

The profile likelihood is then:

$$\lambda(\mu_0|x, y, z) = \frac{\sup\{L(\mu_0, b, e|x, y, z); b, e\}}{\sup\{L(\mu, b, e|x, y, z); \mu, b, e\}} \tag{H.10}$$

Finding the supremum of equation H.9 is not possible analytically, at least to the authors knowledge, and so a C++ program was constructed in order to solve the problem numerically. It worked by first finding the denominator of equation H.10 with three nested do loops, each scanning a relevant section of μ, b and e parameter space. This was the most time consuming part as there were three degrees of freedom to process. The numerator of equation H.10 utilized the same method but required only the supremum of the two nuisance parameters; the background and detection efficiency. This process was repeated for a range of possible μ_0, creating the profile function shown in figure H.1, which only shows two parameters for practical reasons.

The minimum of the function -2 $\log(\lambda)$ converges to a χ^2 distribution [44], which can be used to extract limits on μ. This is possible as when the -2 $\log(\lambda)$ curve increases by an α percentile of the χ^2 distribution, with one degree of freedom, the corresponding values taken by μ are the limits on the confidence interval. In this case a 95% confidence interval on μ was extracted by taking the limits where the distribution increases by 3.84 from the minimum. When the relevant function is plotted it can be clearly seen (figure H.2) that the result is not statistically consistent with zero at this confidence level.

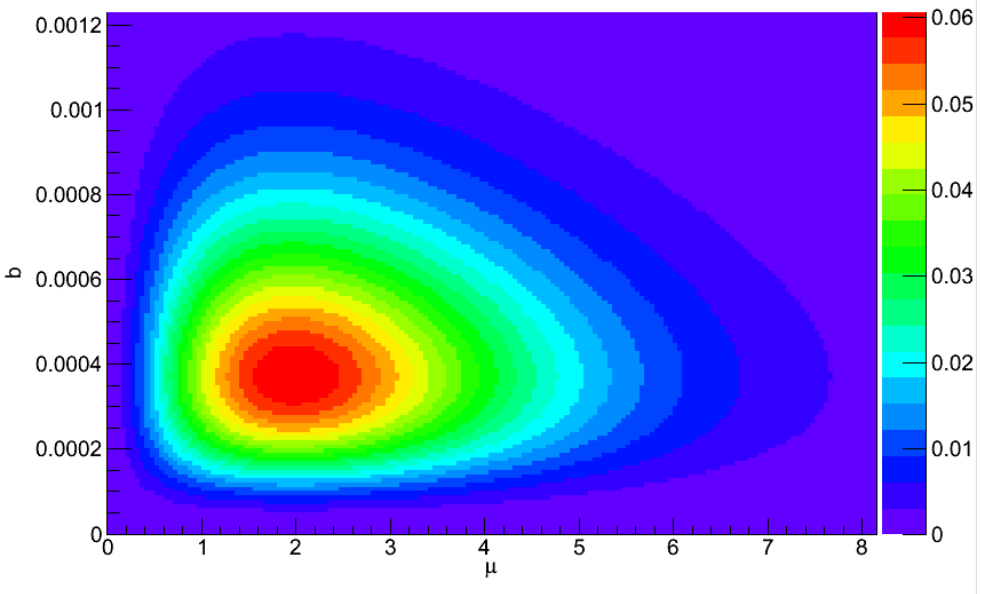

FIGURE H.1: 2D histogram showing how the profile likelihood varies as a function of μ and b for the given data set. The peak of the likelihood occurs when the signal strength is 2 and the background is just ≈ 0.0004, illustrating the power of DRAGON's background suppression.

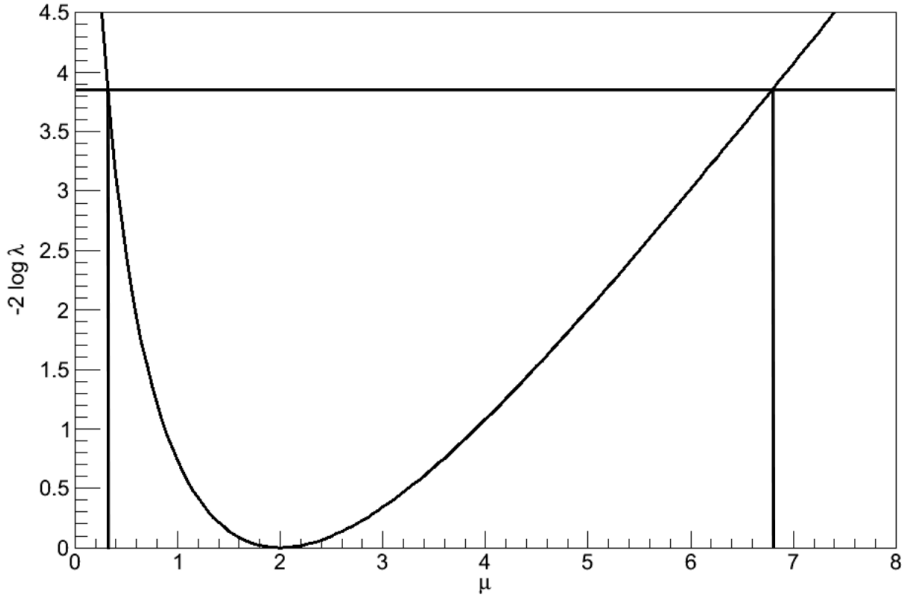

FIGURE H.2: -2logλ function for the data. The vertical lines show where the function increases by 3.84, relative to the minimum, corresponding to a 95% confidence interval. A value of $2.0^{+4.8}_{-1.7}$ for the number of recoil events detected (N_r^{det}) is therefore assumed.

Appendix I

BGO Array Simulation

A Geant4 simulation of the BGO array was constructed, by the author, primarily for the purpose of estimating the gamma detection coincidence efficiency during data acquisition. A previous simulation, utilizing Geant3, exists [32] but is relatively slow and difficult to modify. Multiplicity distributions were difficult to extract and also, in the case of an unknown cascade, it is desirable to simulate multiple possibilities for the purposes of comparison with experimental data, something that was troublesome with the Geant3 model.

Geometry for the various detectors and their constituent parts was taken from original DRAGON eDrawings and Dario Giglotti's Thesis work [32]. As described in section 2.2.3, the array consists of 30 BGO scintillation detectors arranged in two tessellated side arrays flanking the chamber, with another 10 crowning the top and sides for optimal solid angle coverage. The simulation's geometry is shown in figure I.1 with the numbering scheme illustrated in figure I.2. A DAQ (data acquisition) class was written especially to replicate the functionality of that at DRAGON (see section 2.2.7), but without the tail side (heavy ion electronics). Recorded variables were also programmed to mimic those from the actual DAQ to make comparison with experimental data more straightforward.

The two simulations were compared for a variety of scenarios from the Thesis material with the results shown here in tabular form (see tables I.1, I.2, I.3, I.4, I.5 and I.6), displaying photo-peak efficiency for the Geant 4 simulation (G4), the Geant 3 simulation (G3) together with experimental results (Exp). The reader is encouraged to review the original work for further details of each scenario. Almost all of the detectors in each comparison agree to within 10% for the two simulations, and a significant portion to within 5%.

These comparisons only take into account the photo-peak of the spectra however. In fact a large number of γ events in real detectors lie beneath this energy region (see section 2.2.8) and so the simulation's ability to replicate a full spectrum was investigated, using a ^{60}Co source with a known cascade scheme and angular distribution (see figure I.3). The source used had an activity of 5.65 Bq and was taped near the geometric centre of the chamber. The software threshold (the minimum energy needed to be deposited in a single detector during the course of a decay event) of the BGO array was set to 0.65 MeV so as to minimize the effect of 511 keV background gamma rays without being great enough to wrongly discredit too many genuine decay events. Data were taken with and without the source in place, the latter as a measure of background that was subsequently subtracted from the source data,

and an experimental energy spectrum was obtained. An energy spectrum was produced for a single detector (number 22 in figure I.2) with the simulation data produced and analyzed in an identical manner.

The results are displayed in figure I.4 with the simulation data overlayed onto the experimental spectrum. Both spectra have been normalized such that their integrals are equal to one. Good agreement can be seen in the shape of both spectra indicating that the simulation is accurately replicating the Compton scattering, which is the dominant detection process at these energies in the BGO crystal, as explained in section 2.2.8. One discrepancy to note is the energy miscalibration however. The source of this energy offset at low energies comes from the array calibration phase, (as described in appendix B) and is due to the fact that only one higher energy point is used, at 6.13 MeV. For future experiments that intend to make use of the BGO simulation it would be wise to take a run with a low energy source to avoid this issue.

Ultimately the good agreement exhibited in both photo-peak efficiency and Compton scattering convinced the author that the Geant4 model was capable of being utilized for the purposes of scientific research.

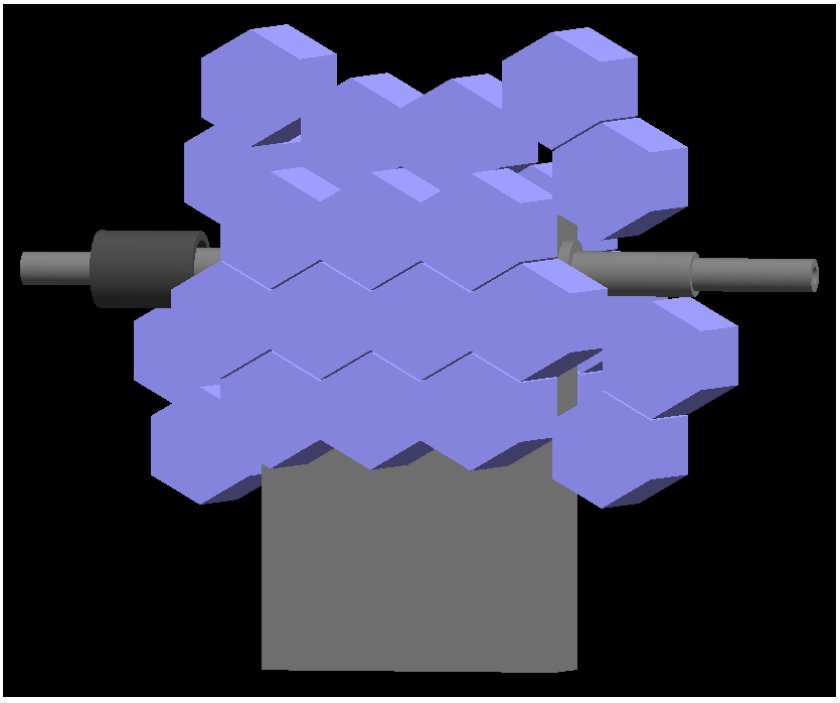

FIGURE I.1: Visualization of the detector geometry using in the Geant4 simulation. The detector's outer casing is shown in blue with the chamber and pumping tubes in grey.

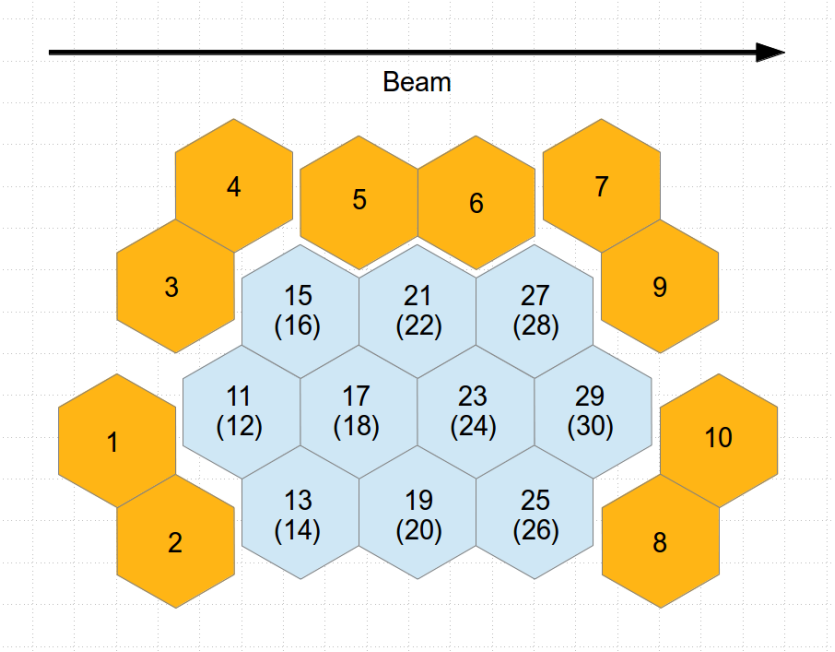

FIGURE I.2: Numbering scheme for the BGO array, as used in [32] and the Geant4 simulation. Blue detectors comprise the two side arrays with the numbers in brackets denoting detectors on the opposite side of the chamber. Orange detectors are those crowning the chamber.

Source	E_γ(MeV)	G4 (%)	G3 (%)	Exp (%)
^{137}Cs	0.662	1.17	1.19	1.20 ± 0.03
^{60}Co	1.33	0.84	0.84	0.85 ± 0.02
^{241}Am^{9}Be	4.44	0.44	0.45	0.42 ± 0.03
^{244}Cm^{13}C	6.13	0.38	0.39	0.39 ± 0.04

TABLE I.1: Comparison of photo-peak efficiencies for a single detector with its face placed 10 cm perpendicularly away from four sources.

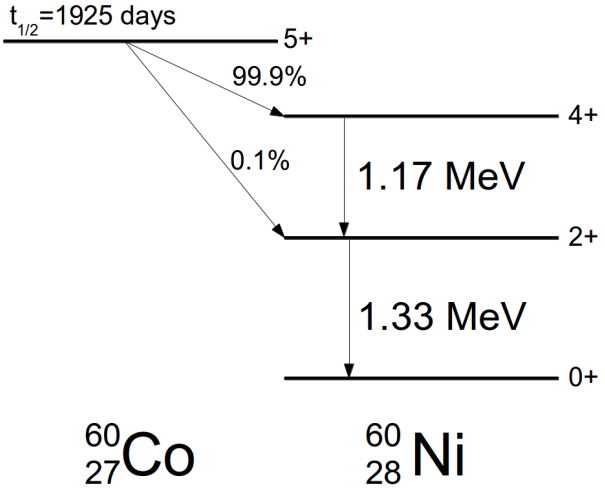

FIGURE I.3: Decay scheme for ^{60}Co, decay data taken from [148].

Det. #	G4 (%)	G3 (%)	Exp (%)
1	0.06	0.06	0.11 ± 0.01
2	0.33	0.32	0.35 ± 0.04
3	0.12	0.14	0.23 ± 0.03
4	0.27	0.30	0.33 ± 0.04
5	1.16	1.22	1.37 ± 0.15
6	1.17	1.21	1.41 ± 0.15
7	0.27	0.30	0.29 ± 0.03
8	0.33	0.32	0.28 ± 0.03
9	0.47	0.48	0.51 ± 0.06
10	0.33	0.32	0.32 ± 0.03
12	0.33	0.31	0.40 ± 0.04
14	0.29	0.26	0.31 ± 0.03
16	0.69	0.67	0.80 ± 0.09
18	1.30	1.22	1.35 ± 0.15
20	0.53	0.48	0.54 ± 0.06
22	1.61	1.60	1.73 ± 0.19
24	1.29	1.22	1.25 ± 0.14
26	0.29	0.27	0.29 ± 0.03
28	0.69	0.66	0.75 ± 0.08
30	0.33	0.30	0.36 ± 0.04

TABLE I.2: Comparison of photo-peak efficiencies for $^{244}Cm^{13}C$ source positioned in the centre of the target chamber.

Det. #	G4 (%)	G3 (%)	Exp (%)
11	0.033	0.033	0.035 ± 0.004
12	0.032	0.033	0.034 ± 0.004
13	0.027	0.028	0.031 ± 0.003
14	0.028	0.029	0.028 ± 0.003
15	0.042	0.041	0.044 ± 0.005
16	0.041	0.041	0.043 ± 0.005
17	0.034	0.034	0.037 ± 0.004
18	0.033	0.034	0.035 ± 0.004
19	0.029	0.029	0.031 ± 0.003
20	0.028	0.029	0.030 ± 0.003
21	0.041	0.042	0.048 ± 0.005
22	0.041	0.043	0.046 ± 0.005
23	0.034	0.034	0.037 ± 0.004
24	0.034	0.035	0.036 ± 0.004
25	0.028	0.029	0.030 ± 0.003
26	0.028	0.028	0.028 ± 0.003
27	0.041	0.041	0.045 ± 0.005
28	0.040	0.043	0.045 ± 0.005
29	0.034	0.033	0.036 ± 0.004
30	0.031	0.033	0.035 ± 0.004

TABLE I.3: Comparison of photo-peak efficiencies for $^{244}Cm^{13}C$ source positioned 15 cm above the centre of the top of the outer chamber, with the array retracted 31.5 cm.

Det. #	G4 (%)	G3 (%)	Exp (%)
11	0.039	0.039	0.041 ± 0.003
12	0.038	0.038	0.040 ± 0.003
13	0.033	0.032	0.036 ± 0.003
14	0.032	0.033	0.034 ± 0.002
15	0.049	0.049	0.049 ± 0.004
16	0.048	0.048	0.050 ± 0.004
17	0.039	0.040	0.044 ± 0.003
18	0.039	0.038	0.042 ± 0.003
19	0.034	0.034	0.037 ± 0.003
20	0.033	0.034	0.036 ± 0.003
21	0.048	0.051	0.054 ± 0.004
22	0.049	0.050	0.052 ± 0.004
23	0.039	0.040	0.043 ± 0.003
24	0.039	0.040	0.042 ± 0.003
25	0.033	0.033	0.035 ± 0.003
26	0.033	0.033	0.033 ± 0.002
27	0.049	0.048	0.051 ± 0.004
28	0.048	0.047	0.052 ± 0.004
29	0.038	0.039	0.041 ± 0.003
30	0.038	0.039	0.040 ± 0.003

TABLE I.4: Comparison of photo-peak efficiencies for ^{241}Am^{9}Be source positioned 15 cm above the centre of the top of the outer chamber, with the array retracted 31.5 cm.

Det. #	G4 (%)	G3 (%)	Exp (%)
1	0.050	0.051	0.048 ± 0.004
2	0.074	0.074	0.070 ± 0.005
3	0.056	0.059	0.055 ± 0.004
4	0.085	0.088	0.084 ± 0.006
5	0.092	0.096	0.091 ± 0.007
6	0.095	0.097	0.093 ± 0.007
7	0.084	0.088	0.087 ± 0.006
8	0.075	0.077	0.071 ± 0.005
9	0.086	0.087	0.086 ± 0.006
10	0.077	0.078	0.073 ± 0.005
12	0.057	0.059	0.056 ± 0.004
14	0.054	0.056	0.049 ± 0.004
16	0.062	0.063	0.059 ± 0.004
18	0.062	0.062	0.056 ± 0.004
20	0.058	0.058	0.055 ± 0.004
22	0.065	0.065	0.057 ± 0.004
24	0.063	0.060	0.058 ± 0.004
26	0.055	0.058	0.049 ± 0.004
28	0.062	0.063	0.058 ± 0.004
30	0.059	0.060	0.052 ± 0.004

TABLE I.5: Comparison of photo-peak efficiencies for ^{241}Am^{9}Be source positioned on top of the outer chamber (centred with respect to the beam axis, and on the edge facing the east array) with the array retracted 31.5 cm.

Det. #	G4 (%)	G3 (%)	Exp (%)
11	0.137	0.148	0.138 ± 0.004
13	0.130	0.140	0.134 ± 0.003
15	0.146	0.158	0.135 ± 0.003
17	0.144	0.155	0.148 ± 0.004
19	0.136	0.145	0.137 ± 0.004
21	0.151	0.162	0.158 ± 0.004
23	0.147	0.156	0.161 ± 0.004
25	0.129	0.139	0.150 ± 0.004
27	0.146	0.156	0.151 ± 0.004
29	0.139	0.146	0.133 ± 0.003

TABLE I.6: Comparison of photo-peak efficiencies for ^{137}Cs source positioned on top of the outer chamber (centred with respect to the beam axis, and on the edge facing the east array) with the array retracted 31.5 cm.

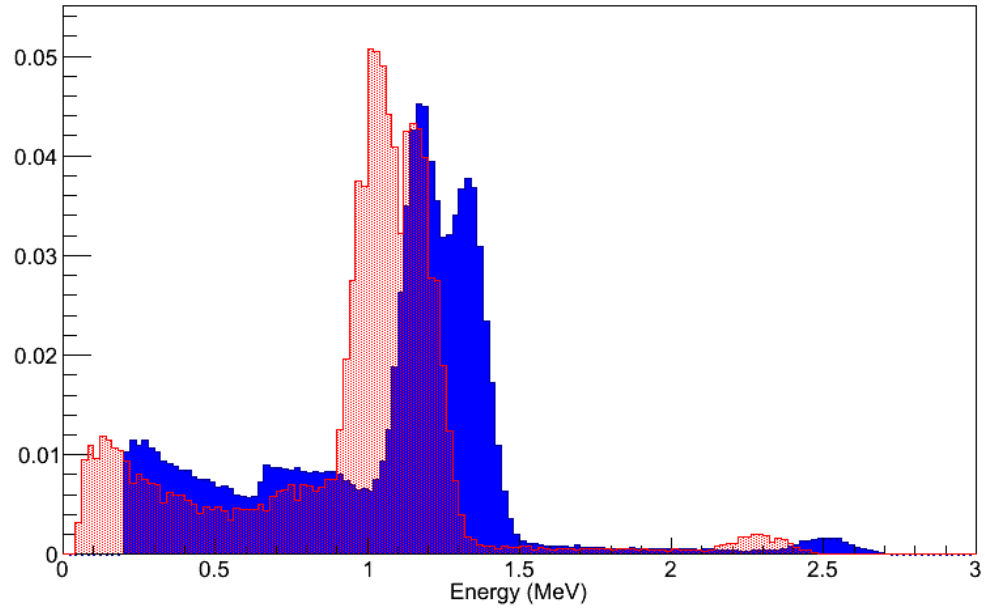

FIGURE I.4: Normalized comparison of the energy spectra in BGO number 22 when a ^{60}Co source is placed inside the target chamber. Blue is the spectrum obtained from the simulation and red is that from the experimental data. It should be noted that in this figure a low energy cut is placed on the experimental data so as to account for the energy miscalibration.

Bibliography

[1] G. Dalrymple. *The Age of the Earth.* Stanford University Press, Redwood City, CA, 1991.

[2] PLANK Collaboration. Planck 2013 results. xvi. cosmological parameters. *Astron. & Astro. Phys.*, 571(A16), 2014.

[3] G.Z. Gamow. *Z. Phys.*, 51(204), 1928.

[4] K. Krane. *Introductory Nuclear Physics.* Wiley-VCH, New York, USA, 1988.

[5] J. Kraushaar and R. Ristinen. Energy and problems of a technical society. *Journal of Chemical Education*, 62(12):327, 1985.

[6] C. Iliadis. *Nuclear Physics of Stars.* John Wiley and Sons, Weinheim, Germany, 2007.

[7] F. Aston. *Mass Spectra and Isotopes.* Longmans, Green & Co., London, England, 1942.

[8] R. d'E. Atkinson and F. G. Houtermans. *Z. Phys.*, 54(656), 1929.

[9] H. A. Bethe and C.L. Critchfield. *Phys. Rev.*, 54(248), 1938.

[10] C. F. Weizsacker. *Phys. Z*, 39(633), 1938.

[11] H. A. Bethe. *Phys. Rev.*, 55(434), 1939.

[12] E. E. Saltpeter. *Astrophys. J.*, 115(326), 1952.

[13] D. N. F. Dunbar *et al. Phys. Rev.*, 92(649), 1953.

[14] C. W. Cook *et al. Phys. Rev.*, 107(508), 1957.

[15] W. A. Fowler E. M. Burbidge, G. R. Burbidge and F. Hoyle. *Phys. Rev.*, 29(4), 1957.

[16] R. W. Merrill. *Astrophys. J.*, 116(21), 1952.

[17] W. A. Mahoney. *Astrophys. J.*, 262(724), 1982.

[18] J. N. Bahcall. *Neutrino Astrophysics.* Cambridge University Press, Cambridge, UK, 1982.

[19] K. S. Hirata *et al.* Results from one thousand days of real-time, directional solar-neutrino data. *Phys. Rev. Lett.*, 65:1297–1300, Sep 1990.

[20] S. Matz *et al. Nature*, 331(416), 1988.

[21] B. Pagel. *Nucleosynthesis and Chemical Evolution of Galaxies, 2nd ed.* Cambridge University Press, Cambridge, UK, 2009.

[22] A compilation of charged-particle induced thermonuclear reaction rates. *Nuclear Physics A*, 656(1):3 – 183, 1999.

[23] F. Hoyle. *Astrophys. J. Suppl.*, 1(121), 1954.

[24] D. W. Bardayan, J. C. Blackmon, W. Bradfield-Smith, C. R. Brune, A. E. Champagne, T. Davinson, B. A. Johnson, R. L. Kozub, C. S. Lee, R. Lewis, P. D. Parker, A. C. Shotter, M. S. Smith, D. W. Visser, and P. J. Woods. Destruction of ^{18}F via ^{18}F(p,α)^{15}O burning through the E_{cm}=665 kev resonance. *Phys. Rev. C*, 63:065802, May 2001.

[25] Erich Vogt. Theory of low energy nuclear reactions. *Rev. Mod. Phys.*, 34:723–747, Oct 1962.

[26] C. Beers. PhD thesis, University of York, 2010.

[27] T Rauscher, N Dauphas, I Dillmann, C Fröhlich, Zs Fülöp, and Gy Gyürky. Constraining the astrophysical origin of the p-nuclei through nuclear physics and meteoritic data. *Reports on Progress in Physics*, 76(6):066201, 2013.

[28] T. Rauscher. Sensitivity of astrophysical reaction rates to nuclear uncertainties. *The Astrophysical Journal Supplement Series*, 201(2):26, 2012.

[29] K. Jayamanna, F. Ames, G. Cojocaru, R. Baartman, P. Bricault, R. Dube, R. Laxdal, M. Marchetto, M. MacDonald, P. Schmor, G. Wight, and D. Yuan. Off-line ion source terminal for ISAC at TRIUMF). *Review of Scientific Instruments*, 79(2):–, 2008.

[30] K. Jayamanna, G. Wight, D. Gallop, R. Dube, V. Jovicic, C. Laforge, M. Marchetto, M. Leross, D. Louie, R. Laplante, R. Laxdal, M. McDonald, G. J. Wiebe, V. Wang, and F. Yan. A multicharge ion source (supernanogan) for the OLIS facility at ISAC/TRIUMF. *Review of Scientific Instruments*, 81(2):–, 2010.

[31] D.A Hutcheon, S Bishop, L Buchmann, M.L Chatterjee, A.A Chen, J.M D'Auria, S Engel, D Gigliotti, U Greife, D Hunter, A Hussein, C.C Jewett, N Khan, M Lamey, A.M Laird, W Liu, A Olin, D Ottewell, J.G Rogers, G Roy, H Sprenger, and C Wrede. The DRAGON facility for nuclear astrophysics at TRIUMF – ISAC: design, construction and operation. *Nuclear Instruments and Methods in Physics Research Section A: Accelerators, Spectrometers, Detectors and Associated Equipment*, 498(1–3):190 – 210, 2003.

[32] D. G. Gigliotti. PhD thesis, University of Northern British Columbia, 2000.

[33] C. Vockenhuber, C. O. Ouellet, L.-S. The, L. Buchmann, J. Caggiano, A. A. Chen, H. Crawford, J. M. D'Auria, B. Davids, L. Fogarty, D. Frekers, A. Hussein, D. A. Hutcheon, W. Kutschera, A. M. Laird, R. Lewis, E. O'Connor, D. Ottewell, M. Paul,

M. M. Pavan, J. Pearson, C. Ruiz, G. Ruprecht, M. Trinczek, B. Wales, and A. Wallner. Measurement of the ^{40}Ca(α,γ)^{44}Ti reaction relevant for supernova nucleosynthesis. *Phys. Rev. C*, 76:035801, Sep 2007.

[34] S. Engel, D. Hutcheon, S. Bishop, L. Buchmann, J. Caggiano, M.L. Chatterjee, A.A. Chen, J. D'Auria, D. Gigliotti, U. Greife, D. Hunter, A. Hussein, C.C. Jewett, A.M. Laird, M. Lamey, W. Liu, A. Olin, D. Ottewell, J. Pearson, C. Ruiz, G. Ruprecht, M. Trinczek, C. Vockenhuber, and C. Wrede. Commissioning the DRAGON facility at ISAC. *Nuclear Instruments and Methods in Physics Research Section A: Accelerators, Spectrometers, Detectors and Associated Equipment*, 553(3):491 – 500, 2005.

[35] Glenn F. Knoll. *Radiation Detection and Measurement*. John Wiley & Sons, 3rd ed. edition, 2000.

[36] M. P. Taggart. PhD thesis, York University, 2012.

[37] *Cyclone Device Handbook*. Altera Corperation, San Jose, CA, 2008.

[38] G. Christian, C. Akers, D. Connolly, J. Fallis, D. Hutcheon, K. Olchanski, and C. Ruiz. Design and commissioning of a timestamp-based data acquisition system for the DRAGON recoil mass separator. *The European Physical Journal A*, 50(4), 2014.

[39] H. Jeffreys. *Theory of Probability*. Clarendon, Oxford, UK, 1983.

[40] A. Stuart and J.K. Ord. *Classical Inference and Relationship*. Oxford University Press, New York, USA, 1983.

[41] J. Neyman. *Phys. Sci.*, 236(767), 1937.

[42] Gary J. Feldman and Robert D. Cousins. Unified approach to the classical statistical analysis of small signals. *Phys. Rev. D*, 57:3873–3889, Apr 1998.

[43] Wolfgang A. Rolke, Angel M. López, and Jan Conrad. Limits and confidence intervals in the presence of nuisance parameters. *Nuclear Instruments and Methods in Physics Research Section A: Accelerators, Spectrometers, Detectors and Associated Equipment*, 551(2–3):493 – 503, 2005.

[44] G. Casella and R.L. Berger. *Statistical Inference*. Duxburry Press, Pacific Grove, CA, 1990.

[45] C. Akers, A. M. Laird, B. R. Fulton, C. Ruiz, D. W. Bardayan, L. Buchmann, G. Christian, B. Davids, L. Erikson, J. Fallis, U. Hager, D. Hutcheon, L. Martin, A. St. J. Murphy, K. Nelson, A. Spyrou, C. Stanford, D. Ottewell, and A. Rojas. Measurement of radiative proton capture on ^{18}F and implications for oxygen-neon novae. *Phys. Rev. Lett.*, 110:262502, Jun 2013.

[46] Sumner Starrfield. Recent advances in studies of the nova outburst. *Physics Reports*, 311(3–5):371 – 381, 1999.

[47] J. José and M. Hernanz. Beacons in the sky: Classical novae vs. x-ray bursts. *The European Physical Journal A - Hadrons and Nuclei*, 27(1):107–115, 2006.

[48] M. Hernanz and J. José. *Classical Nova Explosions.* American Institute of Physics, Melville, New York, 2002.

[49] Jordi José and Margarita Hernanz. Nucleosynthesis in classical novae: CO versus ONe white dwarfs. *The Astrophysical Journal*, 494(2):680, 1998.

[50] C. Iliadis S. Starrfield and W. H. Hix. *Classical Novae, 2nd ed.* Cambridge University Press, Cambridge, UK, 2008.

[51] S.S. Tsygankov S. A. Grebnev, A. A. Lutovinov and C. Winkler. Hard-x-ray emission lines from the decay of ^{44}Ti in the remnant of supernova 1987a. *Nature*, 490:373–375, 2012.

[52] M. Hernanz. *Classical Novae (edited by M. F. Bode and A. Evans).* Cambridge University Press, Cambridge, England, 2nd ed. edition, 2008.

[53] Roland Diehl. Nuclear astrophysics lessons from integral. *Reports on Progress in Physics*, 76(2):026301, 2013.

[54] U. Hager, L. Buchmann, B. Davids, J. Fallis, B. R. Fulton, N. Galinski, U. Greife, D. A. Hutcheon, D. Ottewell, A. Rojas, C. Ruiz, and K. Setoodehnia. Measurement of the ^{17}O(p, γ)^{18}F reaction rate at astrophysically relevant energies. *Phys. Rev. C*, 85:035803, Mar 2012.

[55] A. Kontos, J. Görres, A. Best, M. Couder, R. deBoer, G. Imbriani, Q. Li, D. Robertson, D. Schürmann, E. Stech, E. Uberseder, and M. Wiescher. Proton capture on ^{17}O and its astrophysical implications. *Phys. Rev. C*, 86:055801, Nov 2012.

[56] S. Utku, J. G. Ross, N. P. T. Bateman, D. W. Bardayan, A. A. Chen, J. Görres, A. J. Howard, C. Iliadis, P. D. Parker, M. S. Smith, R. B. Vogelaar, M. Wiescher, and K. Yildiz. Breakout from the hot CNO cycle: The ^{18}F(p, γ) vs ^{18}F(p, α) branching ratio. *Phys. Rev. C*, 57:2731–2739, May 1998.

[57] Christian Iliadis, Art Champagne, Jordi José, Sumner Starrfield, and Paul Tupper. The effects of thermonuclear reaction-rate variations on nova nucleosynthesis: A sensitivity study. *The Astrophysical Journal Supplement Series*, 142(1):105, 2002.

[58] K. E. Rehm, M. Paul, A. D. Roberts, D. J. Blumenthal, J. Gehring, D. Henderson, C. L. Jiang, J. Nickles, J. Nolen, R. C. Pardo, J. P. Schiffer, and R. E. Segel. Study of the ^{18}F(p,α)^{15}O reaction at astrophysical energies using a ^{18}F beam. *Phys. Rev. C*, 52:R460–R463, Aug 1995.

[59] K. E. Rehm, M. Paul, A. D. Roberts, C. L. Jiang, D. J. Blumenthal, S. M. Fischer, J. Gehring, D. Henderson, J. Nickles, J. Nolen, R. C. Pardo, J. P. Schiffer, and R. E. Segel. Astrophysical reaction rate for the ^{18}F(p,α)^{15}O reaction. *Phys. Rev. C*, 53:1950–1954, Apr 1996.

[60] K. E. Rehm, C. L. Jiang, M. Paul, D. Blumenthal, L. A. Daniel, C. N. Davids, P. Decrock, S. M. Fischer, D. Henderson, C. Lister, J. Nickles, J. Nolen, R. C. Pardo, J. P. Schiffer, D. Seweryniak, and R. E. Segel. Exploring the ^{18}F(p,γ)^{19}Ne gateway to the formation of heavy elements in hot stars. *Phys. Rev. C*, 55:R566–R569, Feb 1997.

[61] R. Coszach, M. Cogneau, C.R. Bain, F. Binon, T. Davinson, P. Decrock, Th. Delbar, M. Gaelens, W. Galster, J. Goerres, J.S. Graulich, R. Irvine, D. Labar, P. Leleux, M. Loiselet, C. Michotte, R. Neal, G. Ryckewaert, A.S. Shotter, J. Vanhorenbeeck, J. Vervier, M. Wiescher, and Ph. Woods. A direct measurement of the ^{18}F(p,α)^{15}O reaction. *Physics Letters B*, 353(2–3):184 – 188, 1995.

[62] J.S. Graulich, F. Binon, W. Bradfield-Smith, M. Cogneau, R. Coszach, T. Davinson, Th. Delbar, M. Gaelens, W. Galster, J. Görres, D. Labar, P. Leleux, M. Loiselet, J. McKenzie, R. Neal, G. Ryckewaert, A.C. Shotter, J. Vanhorenbeeck, J. Vervier, M. Wiescher, and Ph. Woods. The ^{18}F(p,α) reaction and its astrophysical implications. *Nuclear Physics A*, 626(3):751 – 759, 1997.

[63] J.-S. Graulich, S. Cherubini, R. Coszach, S. El Hajjami, W. Galster, P. Leleux, W. Bradfield-Smith, T. Davinson, A. Di Pietro, A. C. Shotter, J. Görres, M. Wiescher, F. Binon, and J. Vanhorenbeeck. 7.07 mev resonant state in ^{19}Ne reexamined through a new measurement of the ^{18}F$(p,\alpha)^{15}$O reaction and ^{18}F(p,p) scattering. *Phys. Rev. C*, 63:011302, Dec 2000.

[64] P. Parker. *Nuclear Physics in the Universe.* CRC Press, Oak Ridge, TN, 1992.

[65] S. Utku. PhD thesis, Yale University, 1994.

[66] J. G. Ross. PhD thesis, Notre Dame University, 1994.

[67] Y. M. Butt, J. W. Hammer, M. Jaeger, R. Kunz, A. Mayer, P. D. Parker, R. Schreiter, and G. Staudt. Measurement of the properties of the astrophysically interesting $3/2^+$ state at 7.101 MeV in ^{19}F. *Phys. Rev. C*, 58:R10–R12, Jul 1998.

[68] M. Wiescher, H.W. Becker, J. Görres, K.-U. Kettner, H.P. Trautvetter, W.E. Kieser, C. Rolfs, R.E. Azuma, K.P. Jackson, and J.W. Hammer. Nuclear and astrophysical aspects of ^{18}O$(p,\gamma)^{19}$F. *Nuclear Physics A*, 349(1–2):165 – 216, 1980.

[69] Alain Coc, Margarita Hernanz, Jordi Jose, and Jean-Pierre Thibaud. Influence of new reaction rates on ^{18}F production in novae. *Astron.Astrophys.*, 2000.

[70] N. de Séréville, A. Coc, C. Angulo, M. Assunçāo, D. Beaumel, B. Bouzid, S. Cherubini, M. Couder, P. Demaret, F. de Oliveira Santos, P. Figuera, S. Fortier, M. Gaelens, F. Hammache, J. Kiener, D. Labar, A. Lefebvre, P. Leleux, M. Loiselet, A. Ninane, S. Quichaoui, G. Ryckewaert, N. Smirnova, V. Tatischeff, and J.-P. Thibaud. Study of the ^{18}F(p,α)^{15}O reaction for application to nova γ-ray emission. *Nuclear Physics A*, 718(0):259 – 262, 2003.

[71] N. de Séréville, E. Berthoumieux, and A. Coc. The ^{18}F(p,α)^{15}O reaction rate for application to nova γ-ray emission. *Nuclear Physics A*, 758(0):745 – 748, 2005. Nuclei in the Cosmos VIII Proceedings of the Eighth International Symposium on Nuclei in the Cosmos Eighth International Symposium on Nuclei in the Cosmos.

[72] N. de Séréville, A. Coc, C. Angulo, M. Assunçāo, D. Beaumel, E. Berthoumieux, B. Bouzid, S. Cherubini, M. Couder, P. Demaret, F. de Oliveira Santos, P. Figuera, S. Fortier, M. Gaelens, F. Hammache, J. Kiener, A. Lefebvre-Schuhl, D. Labar, P. Leleux, M. Loiselet, A. Ninane, S. Ouichaoui, G. Ryckewaert, N. Smirnova, and V. Tatischeff. Indirect study of ^{19}Ne states near the threshold. *Nuclear Physics A*, 791(1–2):251 – 266, 2007.

[73] N. De Séréville, C. Angulo, A. Coc, N. L. Achouri, E. Casarejos, T. Davinson, P. Descouvemont, P. Figuera, S. Fox, F. Hammache, J. Kiener, A. Laird, A. Lefebvre-Schuhl, P. Leleux, P. Mumby-Croft, N. A. Orr, I. Stefan, K. Vaughan, and V. Tatischeff. Low-energy ^{18}F(p,α)^{15}O cross section measurements relevant to nova γ-ray emission. *Phys. Rev. C*, 79:015801, Jan 2009.

[74] R.L. Kozub, D.W. Bardayan, J.C. Batchelder, J.C. Blackmon, C.R. Brune, A.E. Champagne, J.A. Cizewski, T. Davinson, U. Greife, C.J. Gross, C.C. Jewett, R.J. Livesay, Z. Ma, B.H. Moazen, C.D. Nesaraja, J.P. Scott, L. Sahin, D. Shapira, M.S. Smith, and J.S. Thomas. New limits for the ^{18}F(p,α)^{15}O rate in novae. *Nuclear Physics A*, 758(0):753 – 756, 2005. Nuclei in the Cosmos VIII Proceedings of the Eighth International Symposium on Nuclei in the Cosmos Eighth International Symposium on Nuclei in the Cosmos.

[75] R. L. Kozub, D. W. Bardayan, J. C. Batchelder, J. C. Blackmon, C. R. Brune, A. E. Champagne, J. A. Cizewski, U. Greife, C. J. Gross, C. C. Jewett, R. J. Livesay, Z. Ma, B. H. Moazen, C. D. Nesaraja, L. Sahin, J. P. Scott, D. Shapira, M. S. Smith, and J. S. Thomas. Neutron single particle strengths from the (d,p) reaction on ^{18}F. *Phys. Rev. C*, 73:044307, Apr 2006.

[76] D. W. Bardayan, J. C. Blackmon, W. Bradfield-Smith, C. R. Brune, A. E. Champagne, T. Davinson, B. A. Johnson, R. L. Kozub, C. S. Lee, R. Lewis, P. D. Parker, A. C. Shotter, M. S. Smith, D. W. Visser, and P. J. Woods. Kinematically complete measurement of the ^{1}H(^{18}F, p)^{18}F excitation function for the astrophysically important 7.08-mev state in ^{19}Ne. *Phys. Rev. C*, 62:042802, Sep 2000.

[77] D.W. Bardayan, J.C. Blackmon, W. Bradfield-Smith, C.R. Brune, A.E. Champagne, T. Davinson, B.A. Johnson, R.L. Kozub, C.S. Lee, R. Lewis, P.D. Parker, A.C. Shotter, M.C. Smith, D.W. Visser, and P.J. Woods. Determination of properties of the 7.08 Mev state in ^{19}Ne by measurement of the ^{1}H(^{18}F,p)^{18}F and ^{1}H(^{18}F,α)^{15}O cross sections with a radioactive ^{18}F beam. *Nuclear Physics A*, 688(1–2):475 – 477, 2001. Nuclei in the Cosmos.

[78] D. W. Bardayan, J. C. Batchelder, J. C. Blackmon, A. E. Champagne, T. Davinson, R. Fitzgerald, W. R. Hix, C. Iliadis, R. L. Kozub, Z. Ma, S. Parete-Koon, P. D. Parker, N. Shu, M. S. Smith, and P. J. Woods. Strength of the ^{18}F(p,α)^{15}O resonance at E_{cm}=330 kev. *Phys. Rev. Lett.*, 89:262501, Dec 2002.

[79] K. Y. Chae, D. W. Bardayan, J. C. Blackmon, D. Gregory, M. W. Guidry, M. S. Johnson, R. L. Kozub, R. J. Livesay, Z. Ma, C. D. Nesaraja, S. D. Pain, S. Paulauskas, M. Porter-Peden, J. F. Shriner Jr., N. Smith, M. S. Smith, and J. S. Thomas. First experimental constraints on the interference of $\frac{3}{2}^+$ resonances in the ^{18}F(p,α)^{15}O reaction. *Phys. Rev. C*, 74:012801, Jul 2006.

[80] J. C. Dalouzy, L. Achouri, M. Aliotta, C. Angulo, H. Benhabiles, C. Borcea, R. Borcea, P. Bourgault, A. Buta, A. Coc, A. Damman, T. Davinson, F. de Grancey, F. de Oliveira Santos, N. de Séréville, J. Kiener, M. G. Pellegriti, F. Negoita, A. M. Sánchez-Benítez, O. Sorlin, M. Stanoiu, I. Stefan, and P. J. Woods. Discovery of a new broad resonance in ^{19}Ne: Implications for the destruction of the cosmic γ-ray emitter ^{18}F. *Phys. Rev. Lett.*, 102:162503, Apr 2009.

[81] A. St. J. Murphy, A. M. Laird, C. Angulo, L. Buchmann, T. Davinson, P. Descouvemont, S. P. Fox, J. José, R. Lewis, C. Ruiz, K. Vaughan, and P. Walden. Simultaneous measurement of the ^{18}F$(p,p)^{18}$F and ^{18}F(p,α)^{15}O reactions: Implications for the level structure of ^{19}Ne, and for ^{18}F production in novae. *Phys. Rev. C*, 79:058801, May 2009.

[82] D. J. Mountford, A. St J. Murphy, N. L. Achouri, C. Angulo, J. R. Brown, T. Davinson, F. de Oliveira Santos, N. de Séréville, P. Descouvemont, O. Kamalou, A. M. Laird, S. T. Pittman, P. Ujic, and P. J. Woods. Resonances in ^{19}Ne with relevance to the astrophysically important ^{18}F$(p,\alpha)^{15}$O reaction. *Phys. Rev. C*, 85:022801, Feb 2012.

[83] A. S. Adekola, D. W. Bardayan, J. C. Blackmon, C. R. Brune, K. Y. Chae, C. Domizioli, U. Greife, Z. Heinen, M. J. Hornish, K. L. Jones, R. L. Kozub, R. J. Livesay, Z. Ma, T. N. Massey, B. Moazen, C. D. Nesaraja, S. D. Pain, J. F. Shriner, N. D. Smith, M. S. Smith, J. S. Thomas, D. W. Visser, and A. V. Voinov. First proton-transfer study of $^{18}\mathrm{F} + p$ resonances relevant for novae. *Phys. Rev. C*, 83:052801, May 2011.

[84] A. S. Adekola, C. R. Brune, D. W. Bardayan, J. C. Blackmon, K. Y. Chae, C. Domizioli, U. Greife, Z. Heinen, M. J. Hornish, K. L. Jones, R. L. Kozub, R. J. Livesay, Z. Ma, T. N. Massey, B. Moazen, C. D. Nesaraja, S. D. Pain, J. F. Shriner, N. D. Smith, M. S. Smith, J. S. Thomas, D. W. Visser, and A. V. Voinov. Single-nucleon transfer reactions on ^{18}F. *Phys. Rev. C*, 84:054611, Nov 2011.

[85] C. E. Beer, A. M. Laird, A. St. J. Murphy, M. A. Bentley, L. Buchman, B. Davids, T. Davinson, C. A. Diget, S. P. Fox, B. R. Fulton, U. Hager, D. Howell, L. Martin, C. Ruiz, G. Ruprecht, P. Salter, C. Vockenhuber, and P. Walden. Direct measurement of the ^{18}F$(p,\alpha)^{15}$O reaction at nova temperatures. *Phys. Rev. C*, 83:042801, Apr 2011.

[86] A. M. Laird, A. Parikh, A. St. J. Murphy, K. Wimmer, A. A. Chen, C. M. Deibel, T. Faestermann, S. P. Fox, B. R. Fulton, R. Hertenberger, D. Irvine, J. José, R. Longland, D. J. Mountford, B. Sambrook, D. Seiler, and H.-F. Wirth. Is γ-ray emission from novae affected by interference effects in the ^{18}F(p,α)^{15}O reaction? *Phys. Rev. Lett.*, 110:032502, Jan 2013.

[87] D.R. Tilley, H.R. Weller, C.M. Cheves, and R.M. Chasteler. Energy levels of light nuclei A = 18–19. *Nuclear Physics A*, 595(1):1 – 170, 1995.

[88] C. D. Nesaraja, N. Shu, D. W. Bardayan, J. C. Blackmon, Y. S. Chen, R. L. Kozub, and M. S. Smith. Nuclear structure properties of astrophysical importance for ^{19}Ne above the proton threshold energy. *Phys. Rev. C*, 75:055809, May 2007.

[89] Shu Neng-Chuan, D. W. Bardayan, J. C. Blackmon, Chen Yong-Shou, R. L. Kozub, P. D. Parker, and M. S. Smith. New astrophysical reaction rates for ^{18}F(p,α)^{15}O and ^{18}F(p,γ)^{19}Ne. *Chinese Physics Letters*, 20(9):1470, 2003.

[90] D. W. Bardayan, R. L. Kozub, and M. S. Smith. ^{19}F α widths and the ^{18}F+p reaction rates. *Phys. Rev. C*, 71:018801, Jan 2005.

[91] W Liu, G Imbriani, L Buchmann, A.A Chen, J.M D'Auria, A D'Onofrio, S Engel, L Gialanella, U Greife, D Hunter, A Hussein, D.A Hutcheon, A Olin, D Ottewell, D Rogalla, J Rogers, M Romano, G Roy, and F Terrasi. Charge state studies of low energy heavy ions passing through hydrogen and helium gas. *Nuclear Instruments and Methods in Physics Research Section A: Accelerators, Spectrometers, Detectors and Associated Equipment*, 496(1):198 – 214, 2003.

[92] P. G. Bricault, F. Ames, M. Dombsky, F. Labrecque, J. Lassen, A. Mjos, G. Minor, and A. Tigelhoefer. Recent developments of the ion sources at tri university meson factory/isotope separator and accelerator facility). *Review of Scientific Instruments*, 83(2):–, 2012.

[93] P. W. Schmor. An overview of isac. *AIP Conference Proceedings*, 473(1):439–450, 1999.

[94] J. M. D'Auria, R. E. Azuma, S. Bishop, L. Buchmann, M. L. Chatterjee, A. A. Chen, S. Engel, D. Gigliotti, U. Greife, D. Hunter, A. Hussein, D. Hutcheon, C. C. Jewett, J. José, J. D. King, A. M. Laird, M. Lamey, R. Lewis, W. Liu, A. Olin, D. Ottewell, P. Parker, J. Rogers, C. Ruiz, M. Trinczek, and C. Wrede. The ^{21}Na$(p,\gamma)^{22}$Mg reaction from $E_{\mathrm{c.m.}} = 200$ to 1103 kev in novae and x-ray bursts. *Phys. Rev. C*, 69:065803, Jun 2004.

[95] James F. Ziegler, M.D. Ziegler, and J.P. Biersack. SRIM – the stopping and range of ions in matter (2010). *Nuclear Instruments and Methods in Physics Research Section B: Beam Interactions with Materials and Atoms*, 268(11–12):1818 – 1823, 2010. 19th International Conference on Ion Beam Analysis.

[96] Claudio Arlandini, Franz Käppeler, Klaus Wisshak, Roberto Gallino, Maria Lugaro, Maurizio Busso, and Oscar Straniero. Neutron capture in low-mass asymptotic giant branch stars: Cross sections and abundance signatures. *The Astrophysical Journal*, 525(2):886, 1999.

[97] Thomas Rauscher. Branchings in the γ process path revisited. *Phys. Rev. C*, 73:015804, Jan 2006.

[98] W. Rapp, J. Görres, M. Wiescher, H. Schatz, and F. Käppeler. Sensitivity of p-process nucleosynthesis to nuclear reaction rates in a 25 $M_\odot$ supernova model. *The Astrophysical Journal*, 653(1):474, 2006.

[99] Thomas Rauscher, Friedrich-Karl Thielemann, and Karl-Ludwig Kratz. Nuclear level density and the determination of thermonuclear rates for astrophysics. *Phys. Rev. C*, 56:1613–1625, Sep 1997.

[100] T. Rauscher, P. Mohr, I. Dillmann, and R. Plag. Opportunities to constrain astrophysical reaction rates for the s-process via determination of the ground-state cross-sections. *The Astrophysical Journal*, 738(2):143, 2011.

[101] Thomas Rauscher and Friedrich-Karl Thielemann. Astrophysical reaction rates from statistical model calculations. *Atomic Data and Nuclear Data Tables*, 75(1–2):1 – 351, 2000.

[102] A. Sauerwein, J. Endres, L. Netterdon, A. Zilges, V. Foteinou, G. Provatas, T. Konstantinopoulos, M. Axiotis, S. F. Ashley, S. Harissopulos, and T. Rauscher. Investigation of the reaction ^{74}Ge(p,γ)^{75}As using the in-beam method to improve reaction network predictions for p nuclei. *Phys. Rev. C*, 86:035802, Sep 2012.

[103] A. Spyrou, A. Lagoyannis, P. Demetriou, S. Harissopulos, and H.-W. Becker. Cross section measurements of (p,γ) reactions on pd isotopes relevant to the p process. *Phys. Rev. C*, 77:065801, Jun 2008.

[104] S. Galanopoulos, P. Demetriou, M. Kokkoris, S. Harissopulos, R. Kunz, M. Fey, J. W. Hammer, Gy. Gyürky, Zs. Fülöp, E. Somorjai, and S. Goriely. The ^{88}Sr(p,γ)^{89}Y reaction at astrophysically relevant energies. *Phys. Rev. C*, 67:015801, Jan 2003.

[105] P. Tsagari, M. Kokkoris, E. Skreti, A. G. Karydas, S. Harissopulos, T. Paradellis, and P. Demetriou. Cross section measurements of the ^{89}Y(p,γ)^{90}Zr reaction at energies relevant to p-process nucleosynthesis. *Phys. Rev. C*, 70:015802, Jul 2004.

[106] S. Harissopulos, E. Skreti, P. Tsagari, G. Souliotis, P. Demetriou, T. Paradellis, J. W. Hammer, R. Kunz, C. Angulo, S. Goriely, and T. Rauscher. Cross section measurements of the ^{93}Nb(p,γ)^{94}Mo reaction at $E_p = 1.4 - 4.9$MeV relevant to the nucleosynthetic p process. *Phys. Rev. C*, 64:055804, Oct 2001.

[107] A. Spyrou, H.-W. Becker, A. Lagoyannis, S. Harissopulos, and C. Rolfs. Cross-section measurements of capture reactions relevant to the p process using a 4π γ-summing method. *Phys. Rev. C*, 76:015802, Jul 2007.

[108] Zs. Fülöp, Á.Z. Kiss, E. Somorjai, C.E. Rolfs, H.P. Trautvetter, T. Rauscher, and H. Oberhummer. ^{70}Ge(α,γ)^{74}Se cross section measurements at energies of astrophysical interest. *Zeitschrift für Physik A Hadrons and Nuclei*, 355(1):203–207, 1996.

[109] S. Harissopulos, A. Spyrou, A. Lagoyannis, Ch. Zarkadas, H.-W. Becker, C. Rolfs, F. Strieder, J.W. Hammer, A. Dewald, K.-O. Zell, P. von Brentano, R. Julin, P. Demetriou, and S. Goriely. Systematic measurements of proton- and alpha-capture cross sections relevant to the modelling of the p process. *Nuclear Physics A*, 758(0):505 – 508, 2005. Nuclei in the Cosmos {VIII} Proceedings of the Eighth International Symposium on Nuclei in the Cosmos Eighth International Symposium on Nuclei in the Cosmos.

[110] Jens Hasper, Marc Büssing, Michael Elvers, Janis Endres, and Andreas Zilges. In-beam experiments on (p,γ) and (α,γ) reactions for the astrophysical p process. *Journal of Physics: Conference Series*, 202(1):012005, 2010.

[111] G.G. Kiss, T. Rauscher, T. Szücs, Zs. Kertész, Zs. Fülöp, Gy. Gyürky, C. Fröhlich, J. Farkas, Z. Elekes, and E. Somorjai. Determining reaction cross sections via characteristic x-ray detection: α-induced reactions on ^{169}Tm for the astrophysical γ-process. *Physics Letters B*, 695(5):419 – 423, 2011.

[112] C. Yalçn, R. T. Güray, N. Özkan, S. Kutlu, Gy. Gyürky, J. Farkas, G. G. Kiss, Zs. Fülöp, A. Simon, E. Somorjai, and T. Rauscher. Odd p isotope ^{113}In: Measurement of α-induced reactions. *Phys. Rev. C*, 79:065801, Jun 2009.

[113] Gy. Gyürky, G. G. Kiss, Z. Elekes, Zs. Fülöp, E. Somorjai, A. Palumbo, J. Görres, H. Y. Lee, W. Rapp, M. Wiescher, N. Özkan, R. T. Güray, G. Efe, and T. Rauscher. α-induced cross sections of ^{106}Cd for the astrophysical p process. *Phys. Rev. C*, 74:025805, Aug 2006.

[114] Gy Gyürky, Z Elekes, J Farkas, Zs Fülöp, Z Halász, G G Kiss, E Somorjai, T Szücs, R T Güray, N Özkan, C Yalçın, and T Rauscher. Alpha-induced reaction cross section measurements on ^{151}Eu for the astrophysical γ-process. *Journal of Physics G: Nuclear and Particle Physics*, 37(11):115201, 2010.

[115] Gy Gyürky, G G Kiss, Z Elekes, Zs Fülöp, E Somorjai, and T Rauscher. Proton capture cross-section of ^{106,108}Cd for the astrophysical p-process. *Journal of Physics G: Nuclear and Particle Physics*, 34(5):817, 2007.

[116] G. G. Kiss, Gy. Gyürky, Z. Elekes, Zs. Fülöp, E. Somorjai, T. Rauscher, and M. Wiescher. ^{70}Ge. *Phys. Rev. C*, 76:055807, Nov 2007.

[117] Gy. Gyürky, Zs. Fülöp, E. Somorjai, M. Kokkoris, S. Galanopoulos, P. Demetriou, S. Harissopulos, T. Rauscher, and S. Goriely. Proton induced reaction cross section measurements on Se isotopes for the astrophysical p process. *Phys. Rev. C*, 68:055803, Nov 2003.

[118] Gy. Gyürky, E. Somorjai, Zs. Fülöp, S. Harissopulos, P. Demetriou, and T. Rauscher. Proton capture cross section of Sr isotopes and their importance for nucleosynthesis of proton-rich nuclides. *Phys. Rev. C*, 64:065803, Nov 2001.

[119] F.R. Chloupek, A.StJ. Murphy, R.N. Boyd, A.L. Cole, J. Görres, R.T. Guray, G. Raimann, J.J. Zach, T. Rauscher, J.V. Schwarzenberg, P. Tischhauser, and M.C. Wiescher. Measurements of proton radiative capture cross sections relevant to the astrophysical rp- and γ-processes. *Nuclear Physics A*, 652(4):391 – 405, 1999.

[120] T. Sauter and F. Käppeler. (p,γ) rates of ^{92}Mo, ^{94}Mo, ^{95}Mo, ^{98}Mo: Towards an experimentally founded database for p-process studies. *Phys. Rev. C*, 55:3127–3138, Jun 1997.

[121] J. Bork, H. Schatz, F. Käppeler, and T. Rauscher. Proton capture cross sections of the ruthenium isotopes. *Phys. Rev. C*, 58:524–535, Jul 1998.

[122] N. Özkan, A.St.J. Murphy, R.N. Boyd, A.L. Cole, M. Famiano, R.T. Güray, M. Howard, L. Şahin, J.J. Zach, R. deHaan, J. Görres, M.C. Wiescher, M.S. Islam, and T. Rauscher. Cross section measurements of the ^{102}Pd(p,γ)^{103}Ag, ^{116}Sn(p,γ)^{117}Sb, and ^{112}Sn(α,γ)^{116}Te reactions relevant to the astrophysical rp- and γ-processes. *Nuclear Physics A*, 710(3–4):469 – 485, 2002.

[123] I. Căta-Danil, D. Filipescu, M. Ivaşşcu, D. Bucurescu, N. V. Zamfir, T. Glodariu, L. Stroe, G. Căta-Danil, D. G. Ghiţă, C. Mihai, G. Suliman, and T. Sava. Astrophysical s factor for α capture on ^{117}Sn. *Phys. Rev. C*, 78:035803, Sep 2008.

[124] Z. Halász, Gy. Gyürky, J. Farkas, Zs. Fülöp, T. Szücs, E. Somorjai, and T. Rauscher. Investigation of α-induced reactions on ^{130}Ba and ^{132}Ba and their importance for the synthesis of heavy p nuclei. *Phys. Rev. C*, 85:025804, Feb 2012.

[125] G. G. Kiss, T. Szücs, Zs. Török, Z. Korkulu, Gy. Gyürky, Z. Halász, Zs. Fülöp, E. Somorjai, and T. Rauscher. Investigation of α-induced reactions on ^{127}I for the astrophysical γ process. *Phys. Rev. C*, 86:035801, Sep 2012.

[126] Anna Simon, Jennifer Fallis, Artemis Spyrou, AlisonM. Laird, Chris Ruiz, Lothar Buchmann, BrianR. Fulton, Dave Hutcheon, Lars Martin, Dave Ottewell, and Alex Rojas. Radiative capture reactions with heavy beams: extending the capabilities of dragon. *The European Physical Journal A*, 49(5), 2013.

[127] Thomas Rauscher and Friedrich-Karl Thielemann. Tables of nuclear cross sections and recation rates: an addendum to the paper "astrophysical reaction rates from statistical model calculations". *Atomic Data and Nuclear Data Tables*, 79(1):47 – 64, 2001.

[128] Balraj Singh. Nuclear data sheets for A = 80. *Nuclear Data Sheets*, 105(2):223 – 418, 2005.

[129] J. Döring, V. A. Wood, J. W. Holcomb, G. D. Johns, T. D. Johnson, M. A. Riley, G. N. Sylvan, P. C. Womble, and S. L. Tabor. High-spin bands in ^{80}Kr. *Phys. Rev. C*, 52:76–87, Jul 1995.

[130] R. E. Azuma, E. Uberseder, E. C. Simpson, C. R. Brune, H. Costantini, R. J. de Boer, J. Görres, M. Heil, P. J. LeBlanc, C. Ugalde, and M. Wiescher. Azure. *Phys. Rev. C*, 81:045805, Apr 2010.

[131] A. S. Adelkola. PhD thesis, Ohio University, 2009.

[132] C. Iliadis, R. Longland, A.E. Champagne, and A. Coc. Charged-particle thermonuclear reaction rates: Iii. nuclear physics input. *Nuclear Physics A*, 841(1–4):251 – 322, 2010. The 2010 Evaluation of Monte Carlo based Thermonuclear Reaction Rates.

[133] D. W. Visser, J. A. Caggiano, R. Lewis, W. B. Handler, A. Parikh, and P. D. Parker. Particle decay branching ratios for states of astrophysical importance in ^{19}Ne. *Phys. Rev. C*, 69:048801, Apr 2004.

[134] D. W. Bardayan, J. C. Blackmon, J. Gómez del Campo, R. L. Kozub, J. F. Liang, Z. Ma, L. Sahin, D. Shapira, and M. S. Smith. Search for astrophysically important ^{19}Ne levels with a thick-target $^{18}\mathrm{F}(p,p)^{18}\mathrm{F}$ measurement. *Phys. Rev. C*, 70:015804, Jul 2004.

[135] P. Möller, J.R. Nix, and K.-L. Kratz. Nuclear properties for astrophysical and radioactive-ion-beam applications. *Atomic Data and Nuclear Data Tables*, 66(2):131 – 343, 1997.

[136] J.-P. Jeukenne, A. Lejeune, and C. Mahaux. Optical-model potential in finite nuclei from reid's hard core interaction. *Phys. Rev. C*, 16:80–96, Jul 1977.

[137] A. Lejeune. Low-energy optical model potential in finite nuclei from reid's hard core interaction. *Phys. Rev. C*, 21:1107–1108, Mar 1980.

[138] Lynne McFadden and G.R. Satchler. Optical-model analysis of the scattering of 24.7 MeV alpha particles. *Nuclear Physics*, 84(1):177 – 200, 1966.

[139] J.W. Tepel, H.M. Hofmann, and H.A. Weidenmüller. Hauser-feshbach formulas for medium and strong absorption. *Physics Letters B*, 49(1):1 – 4, 1974.

[140] F.-K. Thielemann T. Rauscher. *Stellar Evolution, Stellar Explosions, and Galactic Chemical Evolution*. IOP, Bristol, UK, 1998.

[141] P. Möller, J.R. Nix, W.D. Myers, and W.J. Swiatecki. Nuclear ground-state masses and deformations. *Atomic Data and Nuclear Data Tables*, 59(2):185 – 381, 1995.

[142] Y. Aboussir, J.M. Pearson, A.K. Dutta, and F. Tondeur. Nuclear mass formula via an approximation to the hartree—fock method. *Atomic Data and Nuclear Data Tables*, 61(1):127 – 176, 1995.

[143] J.M. Pearson, R.C. Nayak, and S. Goriely. Nuclear mass formula with bogolyubov-enhanced shell-quenching: application to r-process. *Physics Letters B*, 387(3):455 – 459, 1996.

[144] N. Özkan, G. Efe, R. T. Güray, A. Palumbo, J. Görres, H. Y. Lee, L. O. Lamm, W. Rapp, E. Stech, M. Wiescher, Gy. Gyürky, Zs. Fülöp, and E. Somorjai. Astrophysical s factor for α-capture on ^{112}Sn in the p-process energy range. *Phys. Rev. C*, 75:025801, Feb 2007.

[145] W. Rapp, M. Heil, D. Hentschel, F. Käppeler, R. Reifarth, H. J. Brede, H. Klein, and T. Rauscher. α- and neutron-induced reactions on ruthenium isotopes. *Phys. Rev. C*, 66:015803, Jul 2002.

[146] W. Rapp, I. Dillmann, F. Käppeler, U. Giesen, H. Klein, T. Rauscher, D. Hentschel, and S. Hilpp. Cross section measurements of α-induced reactions on ^{92,94}Mo and ^{112}Sn for p-process studies. *Phys. Rev. C*, 78:025804, Aug 2008.

[147] C. Vockenhuber, L.E. Erikson, L. Buchmann, U. Greife, U. Hager, D.A. Hutcheon, M. Lamey, P. Machule, D. Ottewell, C. Ruiz, and G. Ruprecht. A transmission time-of-flight system for particle identification at a recoil mass separator at low energies. *Nuclear Instruments and Methods in Physics Research Section A: Accelerators, Spectrometers, Detectors and Associated Equipment*, 603(3):372 – 378, 2009.

[148] E. Browne and J.K. Tuli. Nuclear data sheets for A = 60. *Nuclear Data Sheets*, 114(12):1849 – 2022, 2013.